AN IMPLEMENTATION AND ALGORITHM DEVELOPMENT FOR UWB THROUGH THE WALL IMAGING SYSTEM

A THESIS SUBMITTED TO
THE GRADUATE SCHOOL OF NATURAL AND APPLIED SCIENCES
OF
MIDDLE EAST TECHNICAL UNIVERSITY

BY

KEREM KAŞAK

IN PARTIAL FULFILLMENT OF THE REQUIREMENTS
FOR
THE DEGREE OF MASTER OF SCIENCE
IN
ELECTRICAL AND ELECTRONICS ENGINEERING

NOVEMBER 2007

Approval of the thesis:

AN IMPLEMENTATION AND ALGORITHM DEVELOPMENT
FOR UWB THROUGH THE WALL IMAGING SYSTEM

submitted by KEREM KAŞAK in partial fulfillment of the requirements for the degree of **Master of Science in Electrical and Electronics Engineering Department, Middle East Technical University** by,

Prof. Dr. Canan Özgen
Dean, Graduate School of Natural and Applied Sciences _____

Prof. Dr. İsmet Erkmen
Head of Department, Electrical and Electronics Engineering _____

Assist. Prof. Dr. Çağatay CANDAN
Supervisor, Electrical and Electronics Engineering Dept., METU _____

Examining Committee Members:

Prof. Dr. Yalçın TANIK
Electrical and Electronics Engineering Dept., METU _____

Assoc. Prof. Dr. Sencer KOÇ
Electrical and Electronics Engineering Dept., METU _____

Assist. Prof. Dr. Çağatay CANDAN
Electrical and Electronics Engineering Dept., METU _____

Assist. Prof. Dr. A. Özgür YILMAZ
Electrical and Electronics Engineering Dept., METU _____

Dr. Ülkü ÇİLEK DOYURAN (PH. D.)
ASELSAN Inc. _____

Date: _____

I hereby declare that all information in this document has been obtained and presented in accordance with academic rules and ethical conduct. I also declare that, as required by these rules and conduct, I have fully cited and referenced all material and results that are not original to this work.

Name, Last name : Kerem, KAŞAK

Signature :

ABSTRACT

AN IMPLEMENTATION AND ALGORITHM DEVELOPMENT FOR UWB THROUGH THE WALL IMAGING SYSTEM

KAŞAK, Kerem
M.Sc., Department of Electrical and Electronics Engineering
Supervisor: Assist. Prof. Dr. Çağatay CANDAN

November 2007, 112 pages

The feasibility of Ultra Wide Band (UWB) through the wall surveillance system is studied in this thesis. The transmitter and receiver architectures are discussed and an experimental set-up is constructed to verify the theory of UWB sensing. The constructed system has 80 mW peak, 6 μW average transmit power and 500 kHz PRF and a range resolution better than 1 cm. Using the experimental set-up, two problems are examined. The first problem is the respiration rate detection problem. It has been shown that the respiration rate can be accurately estimated and the signs of vital activity can be determined behind the wall. The second problem studied in this thesis is the through the wall imaging problem. The imaging system is based on the construction of a synthetic aperture by sliding the transmit-receive antenna pair along the cross range direction. The cross range resolution is improved by applying a migration algorithm to the collected data. It

has been shown that imaging of a scene 8 meters in range, behind a wall of 20 cm thickness is possible with the available power.

Keywords: UWB radar, SAR, respiration rate estimation, through the wall imaging

ÖZ

GENİŞ BANTLI DARBE RADARI
İLE
DUVAR ARKASI GÖZETLEME

KAŞAK, Kerem
Yüksek Lisans, Elektrik ve Elektronik Mühendisliği Bölümü
Tez Yöneticisi : Yard. Doç. Dr. Çağatay CANDAN

Kasım 2007, 112 sayfa

Bu tezde, ultra geniş bantlı duvar arkası gözetleme sisteminin fizibilite çalışması yapılmıştır. Almaç ve göndermeç mimarileri incelenmiş ve ultra geniş bant algılama teorisinin doğrulanması amacı ile deneysel bir sistem kurulmuştur. Sistemin 80mW tepe, 6 μW ortalama yayın gücü, 500 kHz darbe sıklığı ve 1 cm'den daha hassas menzil çözünürlüğü vardır. Bu sistem kullanılarak iki problem üzerinde çalışılmıştır. Birinci problem soluk sıklığının belirlenmesi problemidir. Yapılan deneyler ile duvar arkasından yaşam belirtilerinin algılanabileceği ve soluk sıklığının hassasiyetle ölçülebileceği gösterilmiştir. Tezde işlenen ikinci problem duvar arkası görüntüleme problemidir. Görüntüleme sistemi, alma ve gönderme anten çiftinin çapraz menzil boyunca kaydırılması ile oluşturulan yapay açıklık üzerine kurulmuştur. Toplanan veriler

bir göç (migrasyon) algoritması ile işlenmiş ve çapraz menzil çözünürlüğü iyileştirilmiştir. Mevcut yayın gücü ile 20 cm kalınlıkta bir duvarın arkasını 8 m menzile kadar görüntülemenin mümkün olduğu gösterilmiştir.

Anahtar kelimeler : UWB radar, SAR, solunum sıklığı belirleme , duvar arkası görüntüleme

ACKNOWLEDGMENTS

I would like to express my deepest gratitude to my supervisor Assist. Prof. Dr. Çağatay Candan for his guidance, advice, criticism, encouragements and insight throughout the research.

I would also like to thank Assoc. Prof. Dr. Sencer Koç for his suggestions and comments.

I am deeply grateful to ASELSAN Inc. for providing tools and other facilities throughout this study.

I would like to forward my appreciation to all my friends and colleagues who contributed to my thesis with their continuous encouragement.

I would also like to express my profound appreciation to my family for their continuous support.

TABLE OF CONTENTS

LIST OF TABLES

LIST OF FIGURES

LIST OF ABBREVIATIONS

ADC	Analog to Digital Converter
FCC	Federal Communications Commission
FDTD	Finite-Difference Time-Domain
FFT	Fast Fourier Transform
FIR	Finite Impulse Response
PRF	Pulse Repetition Frequency
PSD	Power Spectrum Density
RF	Radio Frequency
RCS	Radar Cross-section
RVSM	Radar Vital Signs Monitor
SAR	Synthetic Aperture Radar
SNR	Signal to Noise Ratio
SPDT	Single Pole Double Throw
SRD	Step Recovery Diode
TEM	Traverse Electromagnetic
UWB	Ultra Wide Band

CHAPTER 1

INTRODUCTION

In general, the UWB characterizes transmission systems with instantaneous spectral occupancy in excess of 500 MHz or a fractional bandwidth of more than 0.2. The bandwidth and fractional bandwidth are defined as

$$\text{Spectral Occupancy} = f_H - f_L \tag{1.1}$$

$$\text{Fractional bandwidth} = \frac{2(f_H - f_L)}{f_H + f_L} \tag{1.2}$$

where f_L and f_H are the lower and upper frequencies at the -10 dB emission point. In the Federal Communications Commission (FCC) standards, the UWB frequency spectrum range of is defined from 3.1 to 10.6 GHz [1].

UWB systems rely on waveforms that are sub-nanosecond long and usually free of sine-wave carriers. The figure below shows a sample UWB waveform and its frequency spectrum.

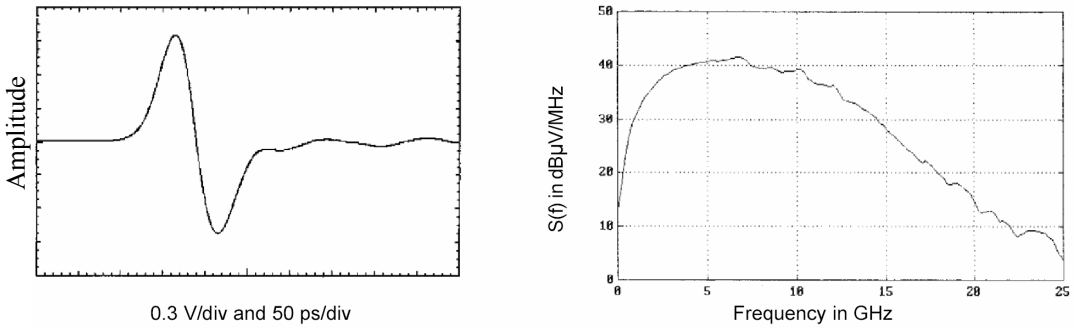

Figure 2-1: A monocycle and its frequency spectrum

As seen from the above figure, UWB waveforms have very large bandwidths. This property of UWB systems promise really greater channel capacity for the same SNR compared with narrowband systems, considering the Shannon's channel capacity theorem ($C= B.\log_2(1+SNR)$). For communication applications, high data rates are possible due to this great channel capacity.

UWB technology also promises target identification and imaging in radar applications. Conventional radars are narrowband systems that have bandwidths no more than 10% of the carrier frequency and they can only provide target detection and low accuracy coordinate measuring, but no target imaging. By UWB technology, the information content of the radar signal is increased as a result of the reduction in the pulse duration [2]. Then UWB offers

- higher range resolution, consequently higher accuracy in range & position measurements
- reduction in the radar dead zones
- recognition of targets as well as forming their radar images since the resolution is high and pulse reflections from separate parts of the target can be collected
- higher radar immunity to passive interferences like rain, fog, clutter, chaff since the interference RCS of these short pulses are comparable with target RCS
- immunity to narrowband electromagnetic interferences and noise

Due to these facts, in the last years a fast growing interest is expressed towards UWB radars in particular and also UWB technologies as a whole. This great interest is confirmed by the growing number of published works and the special international conferences conducted.

Remote sensing the vital parameters of a person is studied for many years since it has a potential for various applications. In 70's and 80's microwave doppler radars were developed for sensing the respiratory movements [3]. Georgia Tech Research Institute (GTRI) designed a radar vital signs monitor (RVSM) for the 1996 Atlanta Olympics that is used for the evaluation of athletes' performances [4]. UWB technology can also be used for the same application owing to its high range resolution. In [5], the novel principle of human being detection is studied and verified experimentally. A UWB radar is developed for detection of respiratory movement and positioning of human beings. Non-invasive respiration rate estimation is studied in [6] and a UWB distributed cognitive radar system is developed for accurate estimation of breathing rate. An analytical frame work is done in [7] for the development of signal processing algorithms of respiration & heart-beat rate estimation even in the presence of a wall in front of the subject. Also the accuracies of the suggested techniques are demonstrated by the conducted experiments. In [8], Continuous Wavelet Transform (CWT) with a special background subtraction method is suggested for the respiration rate detection even behind the walls up to a range of 5m and the method is demonstrated using a radar test setup.

The material penetrating properties of UWB short pulses and the high range resolution achieved by them make UWB systems also capable of imaging through the wall scenes. Through the wall imaging is studied in detail by Defence Research and Development Canada (DRDC) and works are reported. In [9], the capabilities and the limitations of the use of UWB radar system to detect targets behind walls are investigated using a procedure based on finite-difference time-domain (FDTD) method. The images of the simulated scenes are formed using back projection algorithm. Some imaging algorithms are discussed in [10] using simulated data. The effects of thick & strong walls in the imaging are observed

as: defocused target images, displacement from the true target position and formation of false targets. By including effect of the walls in the algorithm, radar images of stationary objects and the room layout are generated. The wall ambiguities are dealt in [11] and an algorithm is suggested for finding the true positions of the targets. It is stated that using different structures of transmit and receive arrays for collecting data from the scene and than solving them for the intersection gives the true position in the case of unknown wall thickness and dielectric constant. In [12], cross-correlated back projection algorithm is studied on the experimental data and it is reported that the resultant images have better cross-range resolution compared to the generated images by back projection. For through the wall imaging, the synthetic aperture radar simulations are worked in [13]. Effects of off-track platform motion on the formed images are examined.

In this thesis, the feasibility of through the wall surveillance radar system is inspected. An experimental system is set up using laboratory equipments and antennas. The resultant UWB radar system has 80 mW peak, 6 μW average transmit power, 500 kHz PRF and range resolution far better than 1 cm. Working on the data collected by this system, the propagation of UWB pulses are studied and algorithms are developed for through the wall imaging & respiration rate estimation. The breathing frequency estimation algorithm detects the motion of the chest in the collected data through the wall and estimates the respiration rate by FFT methods. For imaging application, SAR alternative is suggested instead of physical antenna array and back projection method. By the developed anti-migration algorithm, migration curves caused by the synthetic array are successfully handled and this is proved by the images generated by the algorithm.

The organization of this thesis is as follows. In chapter 2, the general hardware blocks of a UWB radar system: pulse generation & transmitter, receiver and antennas are studied in individual parts. The hardware of the experimental system is analyzed and the radar equation is worked for the system. In chapter 3, propagation and reflection of UWB short pulses are analyzed. It is discussed that someone can comment about the scene behind a wall by observing the collected reflections. In chapter 4, respiration is studied and it is experimentally proved that

the respiration of a man can be detected behind a wall, besides its rate can be easily estimated by the suggested algorithm. Chapter 5 is on the topic of through the wall imaging. The conventional back projection algorithm is analyzed and its weakness against the strong walls is emphasized. As an alternative synthetic aperture method is studied and by the suggested anti-migration algorithm experimental scenes are successfully imaged. In chapter 6, all the work is summarized and further suggestions for a dedicated UWB through the wall radar system are given.

CHAPTER 2

UWB RADAR EQUATION & HARDWARE

In this part, the UWB radar equation and hardware will be examined by comparing them with the classical narrow band systems. The UWB radar products in the market will be briefly examined. Finally, the experimental setup used as an UWB radar system will be given in detail.

2.1 RADAR EQUATION & SNR CALCULATION

The radar equation can be derived step by step for time domain (TD) UWB radar. Assume the radiation form the transmitter antenna is P_t watts. If the antenna is omnidirectional, the power density at a range R is

$$Power\ \ density = P_t \Big/ 4\pi R^2 \quad \left(W/m^2\right) \tag{2.1}$$

If the transmit antenna is directional with a gain of G_t then

$$Power\ \ density = P_t G_t \Big/ 4\pi R^2 \quad \left(W/m^2\right) \tag{2.2}$$

If an object at distance R is subject to this power density, it reradiates some portion of this, proportional to its radar cross-section σ, and the reradiated power density back at the source is

$$Power\ \ density\ \ at\ \ source = P_t G_t \sigma \Big/ (4\pi)^2 R^4 \quad \left(W/m^2\right) \tag{2.3}$$

If the effective area of the received antenna is $A_e = G_r\lambda^2/4\pi$, then the received power P_r is

$$P_r = P_t G_t G_r \lambda^2 \sigma / (4\pi)^3 R^4 \quad (W) \tag{2.4}$$

Since the effective antenna area is a function of λ, this equation is valid for narrow band systems. For the UWB case considering the pulse shape, it is obvious that, there is not a single λ, but λ at the center frequency can be used as an approximation.

The mean noise power for frequency domain (narrow band) receiver with a noise figure $F_n = SNR_i/SNR_o$ (defined at 290°K) is

$$Mean\ noise\ power = F_n k T_0 B_R \tag{2.5}$$

where k is Boltzmann's constant (1.38x10^{-23} J/K), T_0 is 290°K and B_R is the bandwidth of the receiver.

Combining the thermal noise, equipment noise, antenna noise and transmission line noise, the total system noise is defined as

$$Total\ system\ noise\ power = kT_{eq}B_R \tag{2.6}$$

where T_{eq} is the equivalent noise temperature.

For remarking a difference between the narrow band frequency domain and time domain systems, it is worth defining the mean noise energy. If t_n is the temporal sampling bin or the period in which a return is received, then the mean noise energy is defined as $kT_{eq}B_R t_n$. This equation holds for both time domain and frequency domain receivers, but to reduce the noise energy two receiver types must be designed on the idea of reducing different parameters [14].

For the narrow band receiver, it is well known that narrowing the frequency bandwidth B_R decreases noise and the optimum value is $B_R = 1/\Delta t$ where Δt is the pulse width. However, this rule of thumb is not valid for UWB time domain receivers. In the case of UWB receiver, sampling window must be decreased to reduce the noise. In others words, time domain UWB radar gains precision by narrowing Δt and by broadening or placing noise in Δf, due to

$\Delta f \cdot \Delta t$ uncertainty product. On the other hand, conventional narrow band radars gain precision by narrowing Δf and by broadening or placing noise in Δt, again due to $\Delta f \cdot \Delta t$ uncertainty [14]. Although knowing this detail, while talking about the noise power we can use the $kT_{eq}B_R$ approximation.

Dividing the received power by the noise power, the SNR (signal to noise ratio) is obtained as

$$SNR = \frac{P_t G_t G_r \lambda^2 \sigma}{(4\pi)^3 R^4 k T_{eq} B_R} \tag{2.7}$$

The UWB radar used for through the wall surveillance also experiences a loss due to the reflections and attenuation caused by the wall penetration (given in chapter 3). This loss is the wall penetration loss (One-way penetration losses for different walls at various frequencies are given in **Table 3-1**). Pulses pass through the wall twice while propagating from radar towards the target and returning back to the radar from the target. So the wall loss, L_{wall}, is the double of one-way penetration loss. After placing L_{wall} in the SNR equation

$$SNR = \frac{P_t G_t G_r \lambda^2 \sigma}{(4\pi)^3 R^4 k T_{eq} B_R L_{wall}} \tag{2.8}$$

For a concrete wall with a thickness of 15cm, the wall loss is about 22dB for the center frequency of 3 GHz (**Table 3-1**). This loss can be compensated by the processing gain in the receiver.

Processing gain is achieved by coherently summing a number of received pulses. The number of pulses that can be summed is limited by the PRF and the desired maximum rate of target movement for detection. To make it clear, the example given in [15] can be studied in more detail.

Assume a system with the given parameters in **Table 2-1**. For this system the receive SNR without the wall is 14 dB. However in the existence of the concrete wall, because of the 22 dB wall loss, the SNR decreases to -8 dB. In the text, it is given that a SNR above about 14 dB is required for reliable detection of a signal against thermal noise. 14 dB can be required for detection, but for static scene imaging applications less SNR can also give reasonable results considering

our experiments described in chapter 4. To be consistent with the example, the 14 dB SNR goal is taken.

Table 2-1: Radar parameters for a sample system

Parameter	Value in the examined system
Transmit power [W]	10
Center frequency [GHz]	3
Wavelength [m]	0.10
Total antenna gain [dBi]	13
Antenna effective area [m2]	0.01
RCS [m^2]	1
Range [m]	10
System losses [dB]	16
Bandwidth [GHz]	2
Range resolution [cm]	5
Receiver noise figure [dB]	10
SNR without wall [dB]	14
Wall loss for 20cm concrete wall [dB]	22
SNR with 20cm concrete wall [dB]	-5
Integration gain [dB]	~21.8
SNR with wall with integration [dB]	16.8

The aimed minimum unambiguous range in the example is 15m. For this range using the relation $PRF_{\max} = c/2R_{\min}$, the $PRF_{\max}$ is calculated as 10^7 Hz. Coherent integration requires that the movement is less than $\lambda/8$ during integration [15]. For 3 GHz center frequency, λ can be taken as 10cm and $\lambda/8$ is 1.25cm. If the target is a person, the max speed can be taken as 5 m/s. Then the integration time is $1.25cm/(5m/s) = 2.5ms$, that is 25000 pulse period. Since the

bandwidth is 2 GHz, the resolution cell is 7.5cm, the number of range cells is 200; so for scanning the range once, 200 pulse period time elapses. This means that $25000/200 = 125$ pulses drop into the same range cell and can be coherently integrated. That results in ~21.8 dB integration gain. As a result of the integration gain, the resultant SNR is 16.8 dB that is 2.8 dB above the aimed SNR level. The power budget is given in Figure 2-1. This SNR level is above the detectability threshold and well enough for the imaging systems.

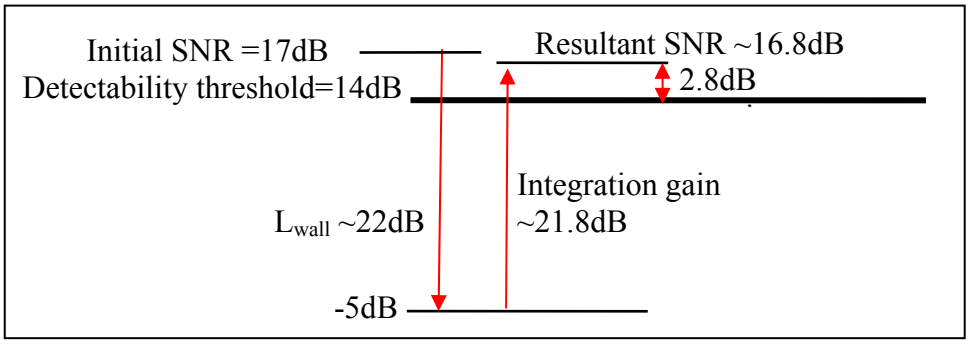

Figure 2-1: Power budget of the examined radar system

2.2 PULSE GENERATION & TRANSMITTER

The transmitters for the UWB radar systems are supposed to generate pulses with durations of hundreds of picoseconds. By using high power switching devices it is possible to obtain peak power values much higher than the conventional radar transmitters can achieve. On the contrary, the average power is considerably low since the pulse duration is shorter than nanosecond. Detection range is dependent on the signal energy which is indeed the time integral of the average power. Currently available switching devices such as light-activated semiconductor switches, bulk avalanche semiconductor switches, commutative nonlinear magnetic switches, vacuum triodes, avalanche semiconductor diodes and laser diodes would be used only for short range UWB radar applications. [14]

In UWB through the wall radar application the range is really short, on the order of tens of meters. Since the range is short, PRF can be increased to raise

the average power. This reduces the peak power level required for detection and consequently there is not a need for high power switching devices anymore. By observing the through the wall radar systems commonly used, 1.5mW average power and less than 5W peak power is well enough for this application (section 2.5). The pulses at these power levels can be produced by simple circuits based on the SRD (step recovery diode) diodes.

SRD is a two terminal P-I-N junction diode whose static (DC) characteristic are similar to a usual p-n junction diode, but with quite different dynamic (switching) characteristics. It is used as a charge controlled switch [16].

During forward conduction, charge is stored in the junction due to finite lifetime of minority carriers. When the SRD is forward biased and the anode current is constant, a charge Q_s is stored in the diode. This charge depends on the intensity of the anode current and minority carrier lifetime τ. If the diode is in steady state of forward conduction with an anode current I_A and the duration is greater than τ , then the stored charge is $Q_s \cong I_A \cdot \tau$. When the voltage bias changes abruptly to a negative value, the diode resistance is low and the anode-cathode voltage is nearly the same as the forward conduction value for a short time because of the stored charge. The stored charge Q_s starts to flow out of the device at a constant rate I_R with the reverse polarity. The stored charge is removed after $t_s \cong Q_s / I_R$ amount of time. When all the charge is removed, the diode resistance rises quickly and within the transition time t_{Tr} it reaches cut-off value. This transition time can be decreased in the production process and switching times of hundreds of picoseconds can be achieved. [17]

As an example to the usage of SRD, the impulse generator circuit in Figure 2-2 can be analyzed as follows: this circuit converts the sinusoidal input to a train of unidirectional pulses. The PRF of the impulses will be the same with the

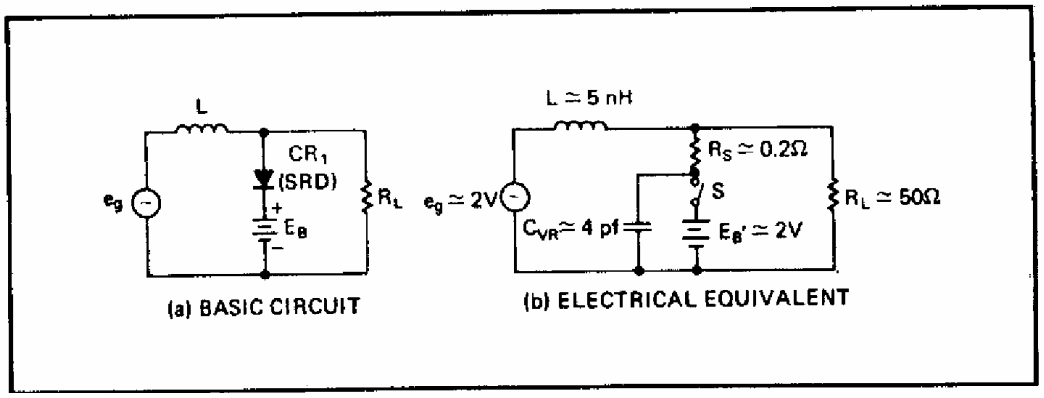

Figure 2-2: Unidirectional impulse generator circuit with SRD [16].

frequency of the sinusoidal input and can be as high as 10MHz. The pulse width can be made extremely narrow and less than 150ps. The bias battery E_B and the average diode forward voltage V_F combines to form E_B' in the equivalent circuit. R_s is negligibly small and the peak voltage of E_G is considerably greater than E_B'. During the positive cycle of the input waveform, the SRD is turned on (S closed in the equivalent circuit) and charge is stored by the positive current. On the negative cycle the direction of the current is reversed and the stored charge is removed. When the charge is removed, SRD stops conducting (S opens) and behaves as a capacitor. This rapid cessation of the current results in a transient waveform involving L, C_{VR} and R_L. If $R_L > \sqrt{L/C_{VR}}$, then the transient is a damped high frequency sine wave of frequency $f_o = 1/2\pi\sqrt{LC_{VR}}$. During the first half cycle of this transient the output impulse is formed, then the SRD is forward biased in the next half cycle and switch S closes. The voltage and current waveforms of the circuit is given in Figure 2-3. The width of the impulse is $\pi\sqrt{LC_{VR}}$ and the impulse height can be related to the E_B' as $V_P = E_B' T\pi/2t_0$ since the average output voltage over a cycle must be zero.

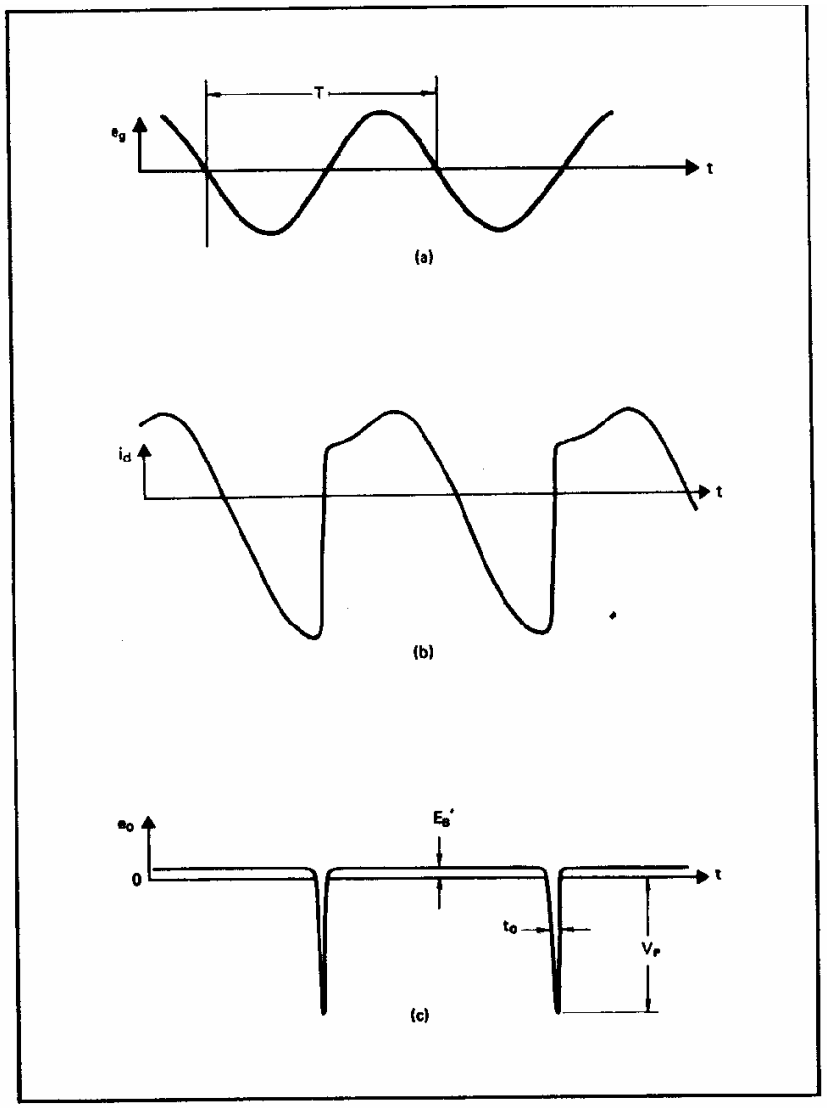

Figure 2-3: Impulse shunt generator typical current and voltage waveforms [16]

This circuit is an impulse generator circuit that can be used in simple UWB transmitters without any coding and it is given in this part to observe how the UWB impulses can be generated. More complex circuits, which are based on the similar technique of producing impulses, can be used for transmitting OOK (on-off keying) modulated, phase modulated or PPM (pulse position modulation) modulated signals.

2.3 RECEIVER

The conventional radar systems use narrowband receivers whose technology and design objectives are well-known. UWB receiver concepts can be more clearly understood by comparing them with the well-known narrowband receivers.

Narrowband receivers restrict the received signal range of interest to a small bandwidth that covers the carrier signal and its modulation which has a smaller frequency than the carrier signal [14]. These receivers generally use the envelope of the received signal, means the only interest is the instantaneous received power over a small frequency range. Detection occurs when the instantaneous received signal envelope power exceeds the receiver noise by some predetermined threshold. A narrowband receiver block diagram is given in Figure 2-4.

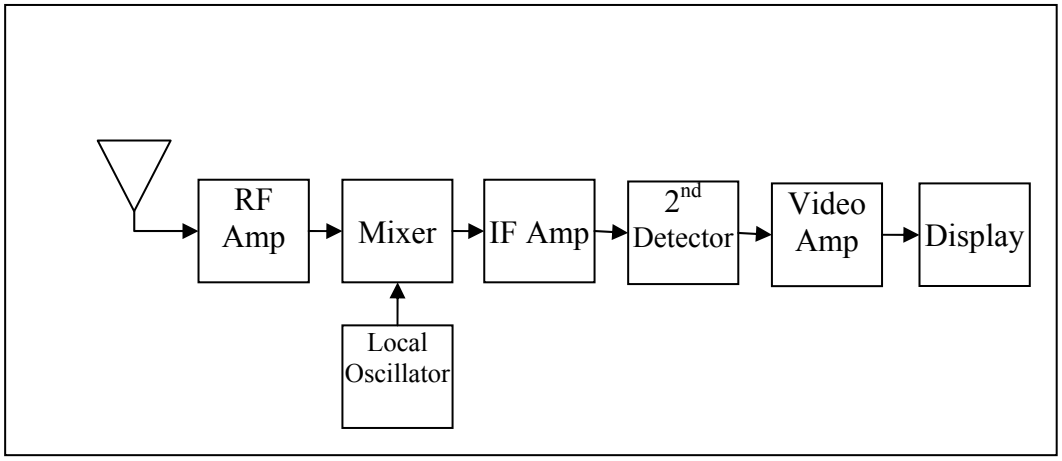

Figure 2-4: Heterodyne receiver block diagram

On the contrary, UWB receivers must have wide bandwidth enough to cover the fastest signal rise time or highest frequency component which is expected. Detection may be done on the signal itself, instead of a video signal. For detection of a signal, threshold detection or correlation with a reference signal waveform can be used. UWB receivers are usually homodyne receivers which can

preserve the received signal waveform and do not perform any frequency conversion or mixing. Homodyne receiver block diagrams are given in Figure 2-5. In the preceding parts, types of homodyne receivers will be observed.

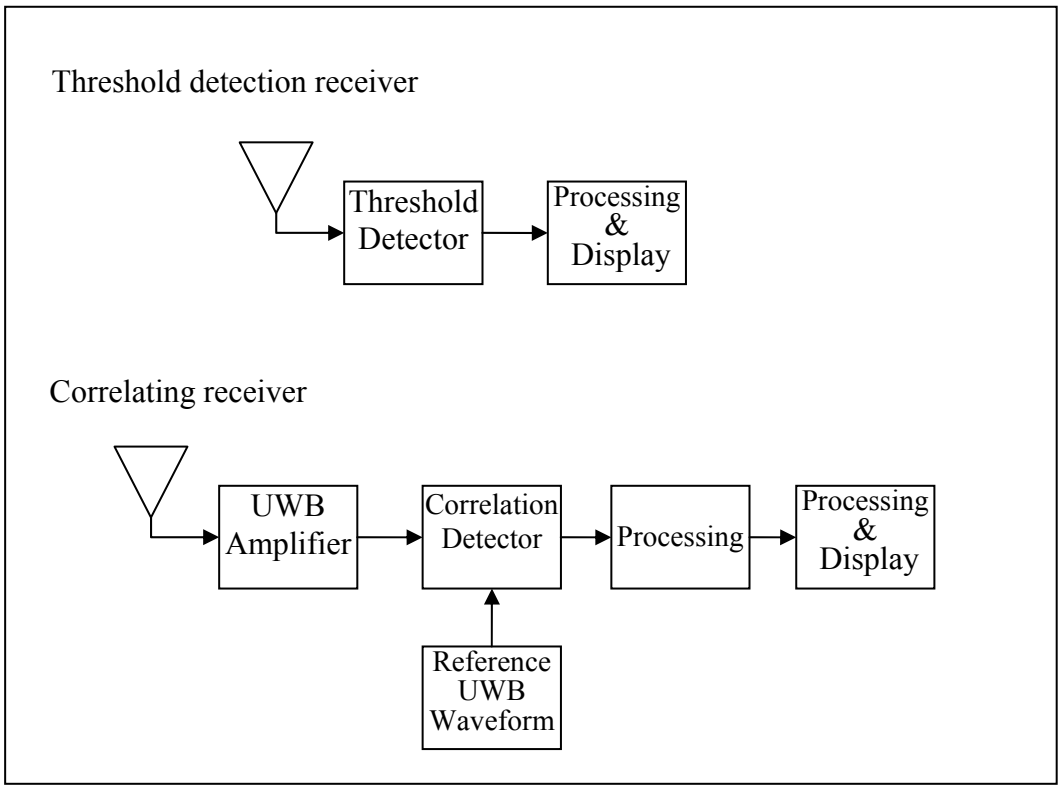

Figure 2-5: Homodyne receiver block diagrams

2.3.1 THRESHOLD DETECTOR RECEIVER

Threshold detection receivers are simpler to build and may be adequate for many applications. The important point is how to determine the impulse signal level required for detection, since it has applications in both the receiver design and interference analysis [14].

The receiver design objectives can be summarized as

- Detecting the presence of short duration UWB signal
- Converting the short duration signal into a longer signal for display

- Resolving signal time of arrival
- Preserving the signal for analysis and sensing applications

A narrowband receiver removes the modulation from the carrier signal and keeps the useful part. In UWB case, the signal waveform is the modulation and shows itself as variations in the received waveform. The homodyne receiver is the logical candidate when the waveform must be preserved [14].

Threshold receivers require a positive SNR in dB scale. The received signal must have enough energy also to overcome the band limiting effects. Then the receiver performance issue is how strong a signal must arrive for reliable detection and/or interference.

Given a receiver with a noise bandwidth B_n and an impulse with a bandwidth of B_I, the required strength of the impulse that will produce a detectable signal can be calculated. The minimum detection level for a UWB signal, M_{bbv} , can be calculated as [14]

$$M_{bbv}(volts/Hz) = 2\left|\frac{Z_i(f)}{Z_s(f)+Z_i(f)}\right|\frac{\sqrt{R_S F_{avg} kTB_n D}}{B_I{}^2} \tag{2.9}$$

where D is the detectability factor (SNR for detection and false alarm), k is the Boltzmann's constant, T is the temperature in Kelvin, R_s is the resistance (nominally 50 Ω), F_{avg} is the noise figure, Z_i & Z_s are the source and input impedances respectively. Here the design objective is to maximize the receiver impulse bandwidth (B_I), to improve impulse signal sensitivity.

Threshold detector is the simplest UWB radar receiver, but it requires an SNR of at least 10dB for 80% probability of detection and with a reasonable (10^{-3} or less) probability of false alarm [14]. For through the wall surveillance UWB radar, where there is a great level of wall attenuation, SNR is generally below this level.

2.3.2 CORRELATION DETECTOR RECEIVER

Correlation is a process that compares an interval of signal with a reference waveform and produces an output proportional to the integral of the product over that interval. It can also be equivalently defined as matched filtering, that is filtering the signal with its time reversed version. Correlation detection is advantageous over the threshold detection, since it does not require a high level of SNR. Correlation detectors can detect the presence of a signal in noise with minimum SNR. Also these detectors have a spatial resolution shorter than the actual signal duration, since the correlation provides a way to integrate the low power signal into a shorter and high power signal that exceeds the receiver noise level.

Mathematically, the correlation coefficient, r, of the two signals $x(t)$ and $s(t)$ is calculated as

$$r = \frac{\sum_{k=0}^{N} x_k s_k}{\sqrt{\left(\sum_{k=0}^{N} x_k^{\,2}\right)\left(\sum_{k=0}^{N} s_k^{\,2}\right)}} \tag{2.10}$$

The correlation coefficient r is $-1 \le r \le 1$, where 1 indicates exact match of the signals, -1 indicates a polarity reversed match and 0 indicates totally uncorrelated signals.

Correlation operation can be conceptually divided into two according to the reference signal used for correlation. In the first type, the transmitted pulse shape is used as the reference signal and in the second type an expected received pulse template, that is the transmitted pulse reshaped by the channel, is used for correlation. In our application, since the pulse will be deformed during its propagation through the wall, the received pulse will not match the transmitted pulse. Therefore, the correlation coefficient between transmitted and received waveforms can never be 1. On the other hand, it is theoretically possible to have a correlation coefficient of 1, capturing full energy in received echo, if the pulse shape of the echo signal can be determined a-priori and used as the template.

Although it is obvious that the pulse shape will be deformed, it is not possible to determine the exact pulse shape that will be received, so practically it is also very difficult to perfectly match the received signal.

The correlation can be also implemented in the frequency domain by the PSD (power spectrum density) correlation. In this method, the PSD of the received signal is calculated as taking the FFT of the signal power and compared with the expected PSD.

The correlation can be handled by analog or digital correlators. Analog correlators, correlate the received signal with a repeating reference signal, so some capability of synchronizing the arrival of the signal with the repeating reference signal is necessary [14]. The analog correlator block diagram is given in Figure 2-6. If the synchronization can not be established, the correlation value will be less than the true value.

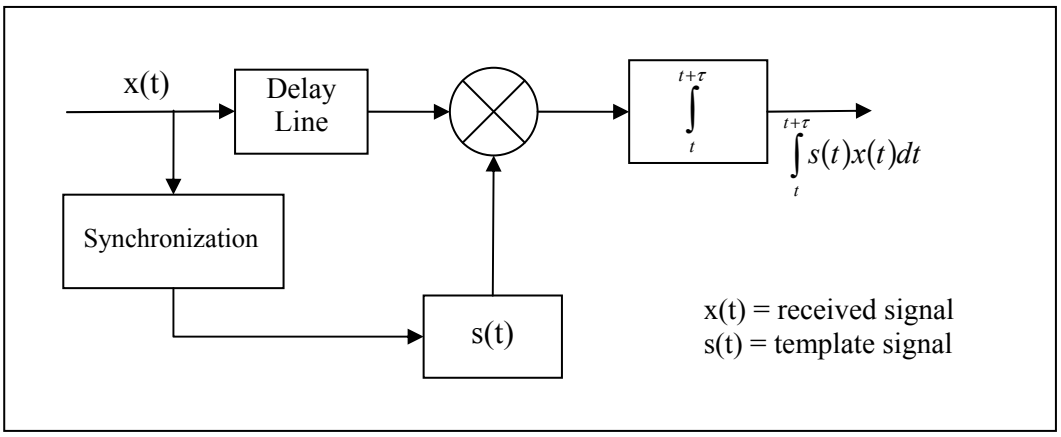

Figure 2-6: Analog correlator block diagram

Digital correlators, in other words FIR filter correlators, can correlate the signal as it occurs and provide a continuous output [14]. Unlike the case of analog correlator, for this correlator type synchronization is not a design constraint. In digital correlators, the sampling rate of the signal and the corresponding correlator lengths are design constraints which will affect the correlator performance. The FIR filter length must be long and the sampling rate must be high enough to

accurately reconstruct the wave from samples. The basic block diagram of a digital correlator is given in Figure 2-7.

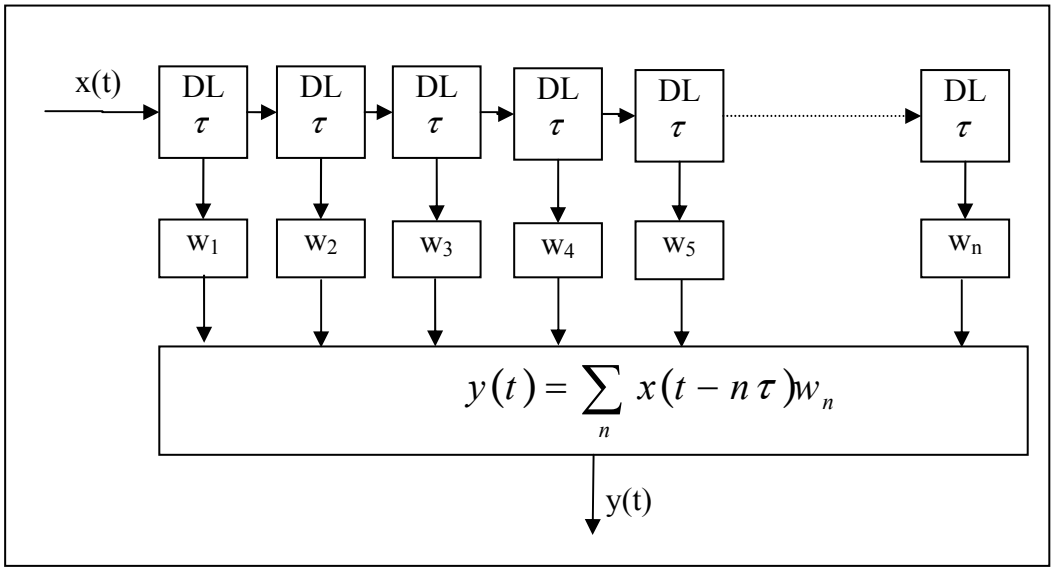

Figure 2-7: Digital correlator block diagram

For signals with bandwidth less than 100 MHz, digital implementation for matched filters are possible. Beyond this, the limited bits from the A/D converters imply that only analog processing can currently provide the required bandwidth. If analog processing is used, the integration time of the matched filter is limited to the order of tens of μs; otherwise, insertion loss becomes excessive. If compared, the digital processing has bandwidth limit, while the analog correlators do not perform well for very low duty cycle waveforms.

2.4 ANTENNAS

Antenna is one of the most critical parts of UWB systems, since it has a significant effect on the system performance. Minimum antenna distortion on the pulse shape is one of the critical issues, since the data is contained also in the

shape of the pulses. The design of such an antenna is difficult, because the fractional bandwidth is very large and the antenna must cover multiple-octave bandwidths [18].

Conventional antenna literature is about narrowband antennas and their analysis. The normal definitions and equations for antenna parameters, such as gain and beamwidth implicitly refer to parameters at a specific frequency and explicitly contain the wavelength. The UWB antenna design and analysis is an extension of conventional antenna which can be considered as an extension from steady-state to transient conditions [14].

UWB pulses are short duration impulsive signals, so they contain a number of frequency components with specific amplitude and phase relationship. If the antenna impedance varies much with frequency, then this will cause a distortion in the pulse shape. Also, if the radiation locations of different frequencies are different, radiated frequency components will travel different distances and will not arrive back at the same time [19]. This causes time dispersion in the radiated signal.

Typical broadband antennas include axial mode helices, biconical dipoles, optically based antennas (e.g. parabolic reflectors) and frequency independent antennas (spirals, conical spirals, log periodic dipole arrays, etc.) [19]. In Figure 2-8, pictures of typical broadband antennas used for UWB applications are given. These antennas offer wide impedance bandwidths, but the radiation location can move with frequency. Some type of antennas can be used for transmitting and some for receiving UWB pulses without differentiating or integrating. Conical antennas radiate an E-M field that is identical in waveform to the voltage driving the antenna and TEM horn antennas output a voltage waveform that is identical to the incident E field. [21]

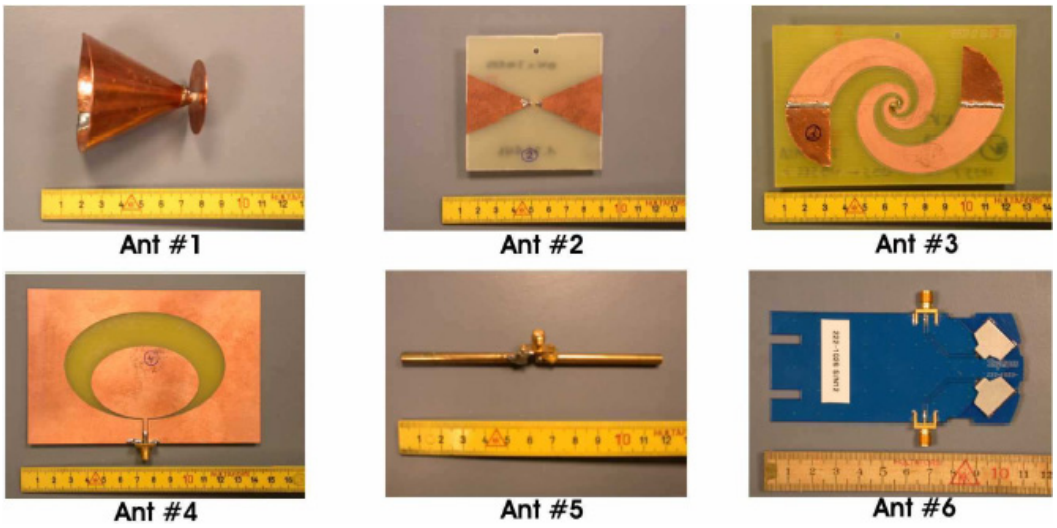

Figure 2-8: Typical broadband antennas

In various UWB applications, like through the wall surveillance, antenna arrays are used to decrease the beamwidth and increase the cross-range resolution. Loaded dipole (receive only), TEM horn, LPDA (log periodic dipole array) and spiral (receive only) antennas are the common options for the array elements. There are severe problems in designing UWB arrays because of the frequency dependence of [14]

- array parameters, particularly geometry and phasing
- grating lobes
- coupling between the adjacent elements

2.5 EXPERIMENTAL SETUP

In the previous sections of this chapter, transmitter & receiver topologies and antenna structures for the UWB radar systems are discussed. In this section, the experimental setup used in this thesis as the radar hardware is discussed in individual subsections such as pulse generation and shaping, transmit & receive antennas, receiver and finally the SNR calculation. The block diagram of the setup is given in Figure 2-9 and a picture of it in Figure 2-10.

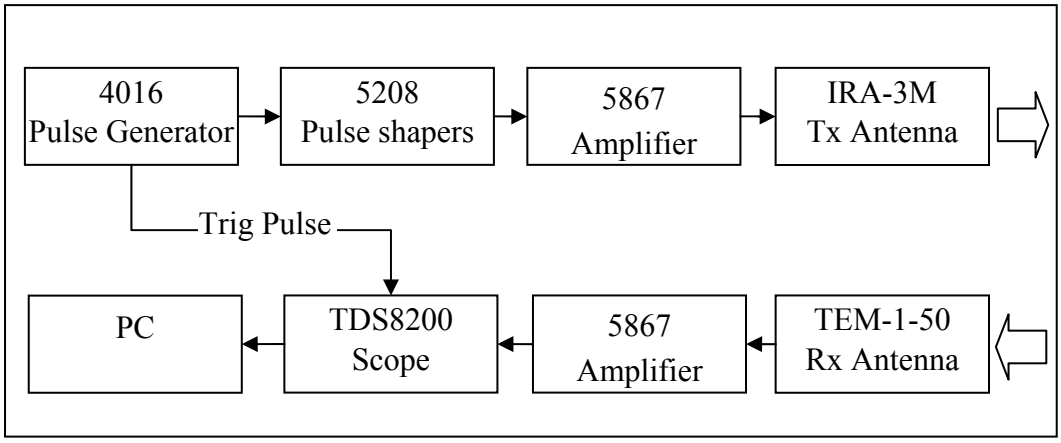

Figure 2-9: Block diagram of the experimental setup

Figure 2-10: Picture of the experimental setup

There are individual transmit and receive antennas in the system. The operating range of this system is a few meters and this is comparable with the distance between the antennas. The locations of transmit and receive antennas are not same and the distances from each antenna to the target are different. According to this, the system can be considered as a bistatic radar. Although the

location of transmit and receive antennas are different, transmit and receive hardware of the system are synchronized by the trig signal of the pulse generator. That is, the experimental system is synchronous like monostatic radar systems, where the transmitter and the receiver are on the same platform and synchronous to each other.

2.5.1 PULSE GENERATION & SHAPING

In the system, model 4016 pulse generator of Picosecond Pulse Lab is used. It generates ultra-fast pulses of -5 V with less than 5 ps fall time into an AC or DC coupled 50Ω load with a maximum PRF of 500 kHz. The output pulse shape of the generator is given in Figure 2-11.

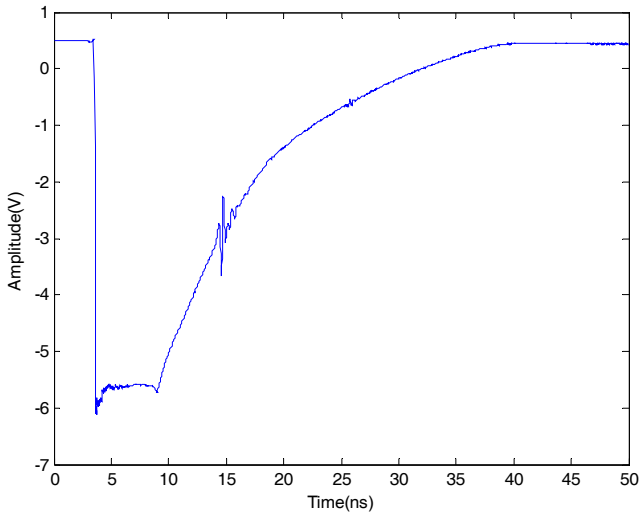

Figure 2-11: Output pulse shape of 4016

The step like pulse generated by the 4016 is then passed through two model 5208 passive impulse forming networks sequentially. 5208 provide an output that is approximately the derivative of the input waveform, that is $V(out) \approx T_c * dV(in)/dt$ where T_c is the derivative time coefficient and 8 ps for

5208. When it is driven by a step, the output is an impulse. When driven by an impulse, the output is a monocycle. According to this fact, the step like waveform from the 4016 pulse generator is converted to an impulse at the output of the first 5208 and this impulse is converted to a monocycle at the output of the second 5208. While differentiating the pulse, each 5208 filters the pulse and widens the pulse duration. Since the energy of the pulse will not increase in this passive element, the amplitude of the pulse will decrease to balance the increase in the duration. The pulse shapes at the outputs of the two 5208 are given in Figure 2-12.

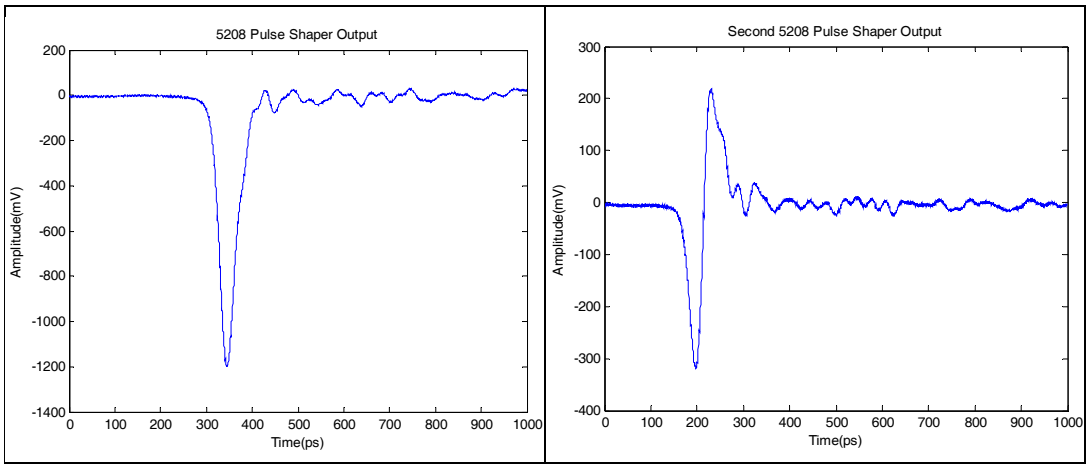

Figure 2-12: Output pulse shapes of 5208

The pulse shaped by impulse forming network is amplified by a broad band linear gain amplifier. Model 5867 amplifier of Picosecond Pulse Lab is used as the amplifier. It has a gain of 15dB and a maximum deviation of 3 degrees from the linear phase. Its characteristics are given in Figure 2-13.

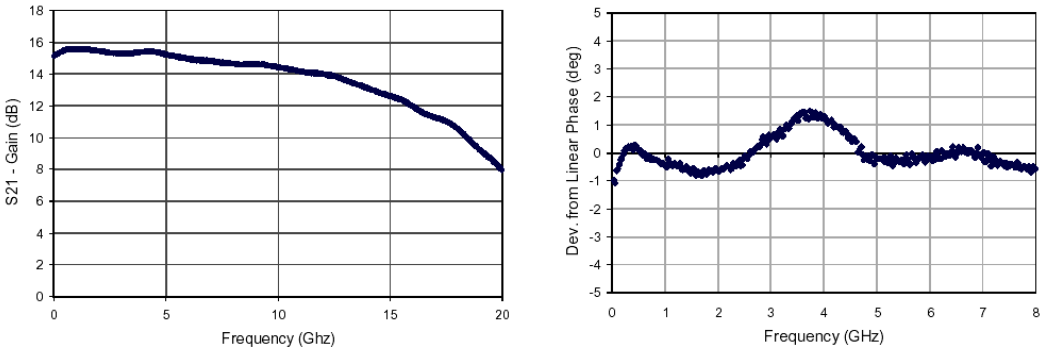

Figure 2-13: Characteristics of 5867 amplifier [29]

The monocycle pulse is inverted and amplified by 15dB by the 5867. At the output of this amplifier the pulse given in Figure 2-14 is observed. The resultant pulse has duration of ~150ps long and amplitude of ~2.5$V_{pk\text{-}pk}$. This pulse is a Gaussian monocycle and is feed to the transmit antenna for radiation.

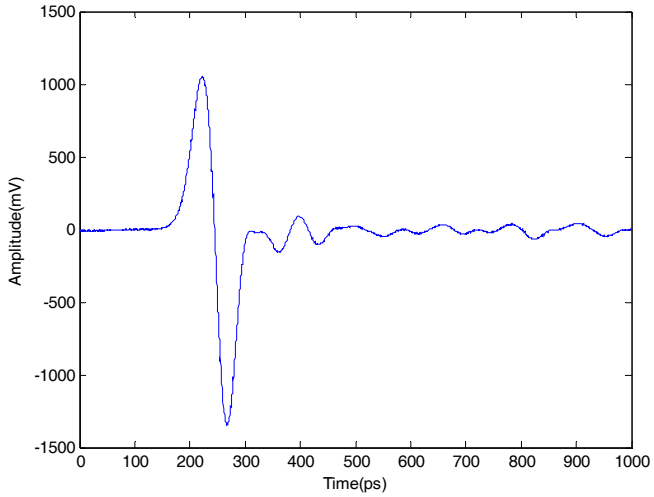

Figure 2-14: Gaussian monocycle at 5867 output

By considering the pulse shape, the frequency range over which the antenna must respond can be judged. The pulse rise time defines the highest frequency needed f_h and the pulse length defines the median frequency f_m [14]. Approximate expressions for them are (time in unit of ps)

$$f_h = \frac{500}{risetime} GHz \text{ and } f_m = \frac{500}{pulselength} GHz \text{ and } f_m = \sqrt{f_h f_l} GHz \qquad (2.11)$$

Using these expressions, the median frequency, highest and lowest frequencies can be calculated for the generated pulse. The rise time of the pulse is nearly 40ps and the duration is 150ps then

$$f_h = \frac{500}{40} = 12.5 \ GHz \qquad f_m = \frac{500}{150} \approx 3.3 \ GHz \qquad f_l = {(3.3)^2}/{12.5} \approx 870 \ MHz \qquad (2.12)$$

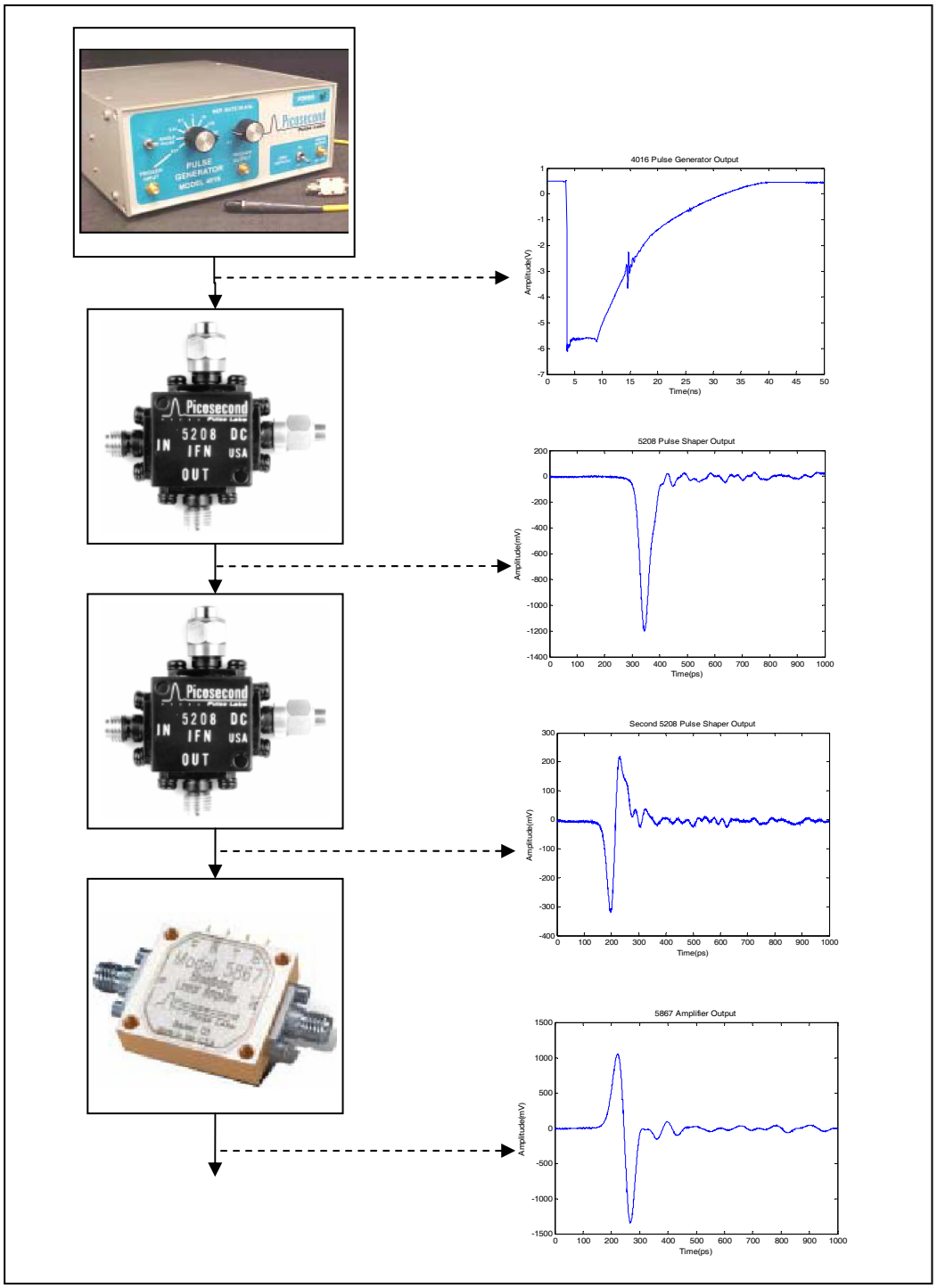

Figure 2-15: Pulse generation and shaping

2.5.2 TRANSMIT & RECEIVE ANTENNAS

For transmission, antennas which transmit E-M field that is identical in waveform to the voltage driving the antenna are used. Similarly for receiving, antennas that produce voltage waveform that is identical to the incident E field are selected. In the experimental setup, the antennas of Farr Research are used which are specially designed for radiating and receiving impulses respectively.

As the transmit antenna, IRA-3M is used. It is an 18″ diameter impulse radiating antenna with two decades of bandwidth. In the previous section, the highest and lowest frequencies of the generated pulse are calculated as 12.5 GHz and 870 MHz respectively. The median frequency is 3.3 GHz. The gain of the antenna for the pulse can be taken as the value at the median frequency. By considering the gain vs. frequency graph given in Figure 2-16 the gain of the antenna can be taken as approximately 18dB.

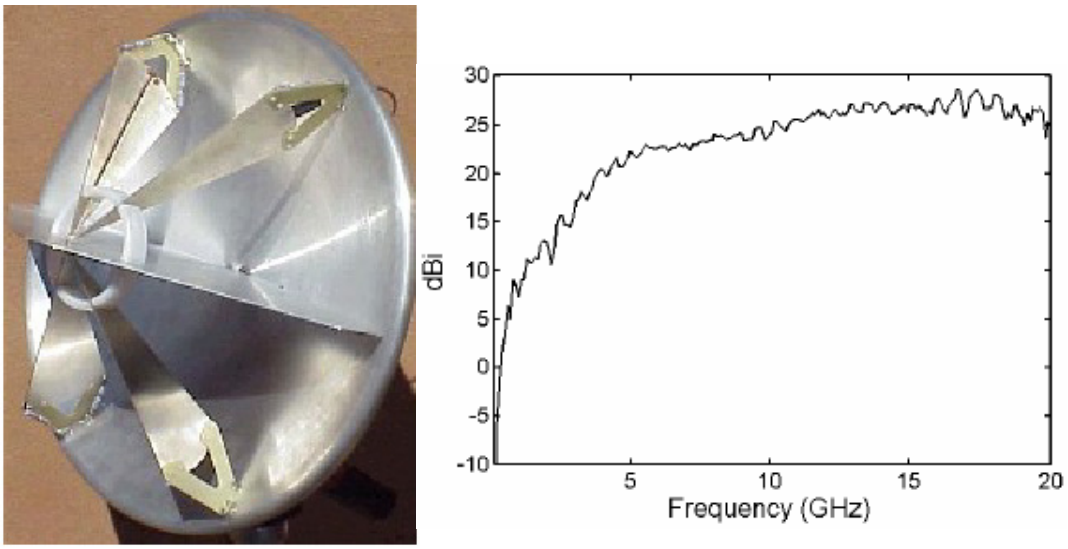

Figure 2-16: IRA-3M & its gain vs. frequency graph [31]

Model TEM-1-50 Ultra-Wideband electric field sensor which is a half TEM horn mounted on a truncated ground plane is used for receiving. Remember from section 2.4 that TEM horn antennas output a voltage waveform that is identical to the incident E field. The gain of the antenna at the median frequency of 3.3 GHz is approximately 5 dB as seen in Figure 2-18.

Figure 2-17: TEM-1-50 antenna [31]

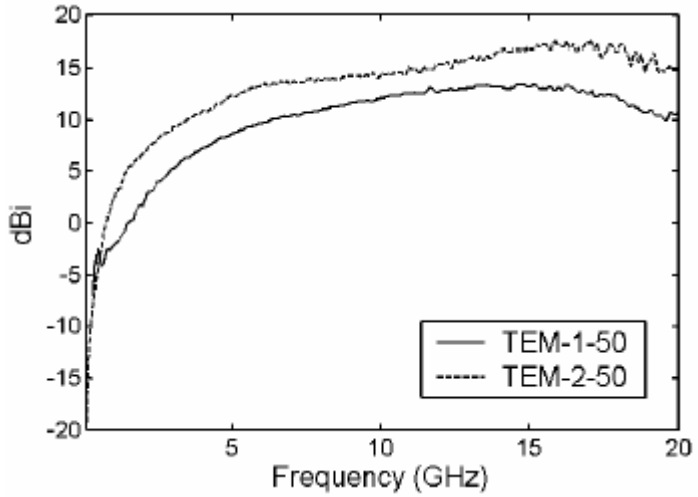

Figure 2-18: TEM-1-50 antenna gain vs. frequency graph [31]

The received pulse shape by the TEM-1-50 can be seen in Figure 2-19. The pulse shape is no more a Gaussian monocycle after it has been radiated by IRA-3M and received back by the TEM-1-50.

In conventional radar systems, a pair of antenna is enough for detecting the range and the position of the target. The antenna system can be rotated to get

the angular information about the location of the target. Although rotation gives angular information in conventional radar systems, it can not be used for through the wall surveillance UWB radar systems. If the antennas are rotated in front of a wall, the pulses usually hit the wall with incidence angles different than zero. This will cause some of them to be completely reflected from the wall without penetrating through it according to the incidence angle. Also some penetrating pulses may not return back to the receive antenna after they reflected form the target because of the angle of incidence again. Effectively, only the pulses which are radiated from the antenna when it is normal to the wall are collected back.

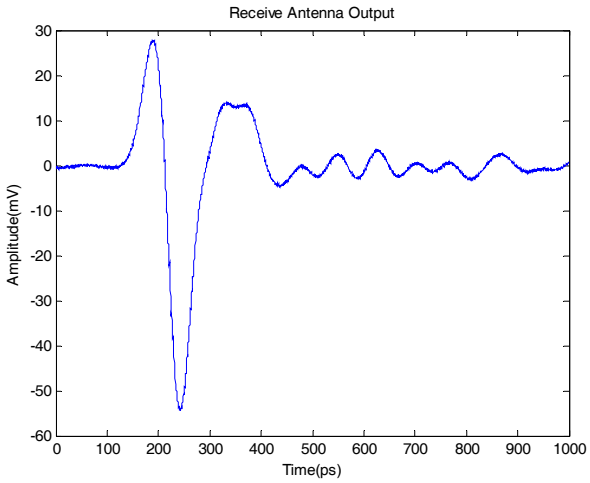

Figure 2-19: Received pulse shape by the TEM-1-50

By using non-rotating two antennas the range of the target can be measured from the travel time of the pulse in the air. From the travel time, the length of the path can be calculated and the range of the target can be found but the location of it can not. If there were more antennas in different locations, the collected reflections by these antennas could be processed together to obtain the locations of the targets. Consequently, for the imaging applications, a pair of antenna is not enough and an antenna array is necessary.

In the setup we only had a pair of antennas not an antenna array. For the imaging application we have used an alternative method, creation of synthetic

aperture array. The two antennas are moved along the wall, and at equally spaced antenna locations on the path of motion, pulses are radiated towards the wall and the reflections are collected. In this way, the two antennas are used as an antenna array.

2.5.3 RECEIVER

In the receiver side of the system, behind the receive antenna again a 5867 model amplifier is used. The pulse shape at the output of the amplifier is given in Figure 2-20.The width of the pulse ~300ps. Remember, the pulse shape was a Gaussian monocycle in front of the transmit antenna with ~150ps pulse width. Shape and duration of the pulse changes much.

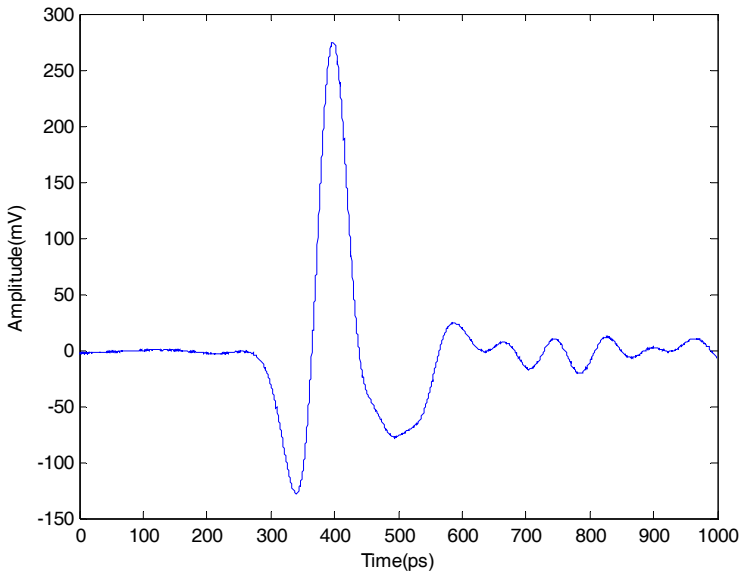

Figure 2-20: Pulse shape at the output of the receiver amplifier

The received signal amplified by 5867 is given to TDS8200 scope. The scope samples the signal by 80E01 model sampling module which has a bandwidth of 50 GHz and rise time of 7ps. The scope is not a real-time sampling oscilloscope. It is an equivalent-time sampler. These values are valid while sampling a signal which repeats itself identically [22].

Real-time samplers only need one trigger to completely sample a period of a signal after the trigger point. They start by the trigger pulse and collect equally spaced samples. On the contrary, equivalent time samplers collect only one sample, after each trigger pulse. By slightly shifting at each trigger pulse, they sample the signal, but this method needs lots of trigger pulses. For example, assume a signal x(t) with period T is sampled by an equivalent time sampler whose shift at each sampling period is Δ. When the sampler is trigged by the n^{th} trigger pulse, it samples after nΔ duration of time. Actually, the first sample is $x_0 = x(0)$, the second one is $x_1 = x(T + \Delta)$, the third one is $x_2 = x(2T + 2\Delta)$ and the n^{th} sample is $x_n = x(nT + n\Delta)$. The equivalent time sampling of the signal is shown in Figure 2-21.

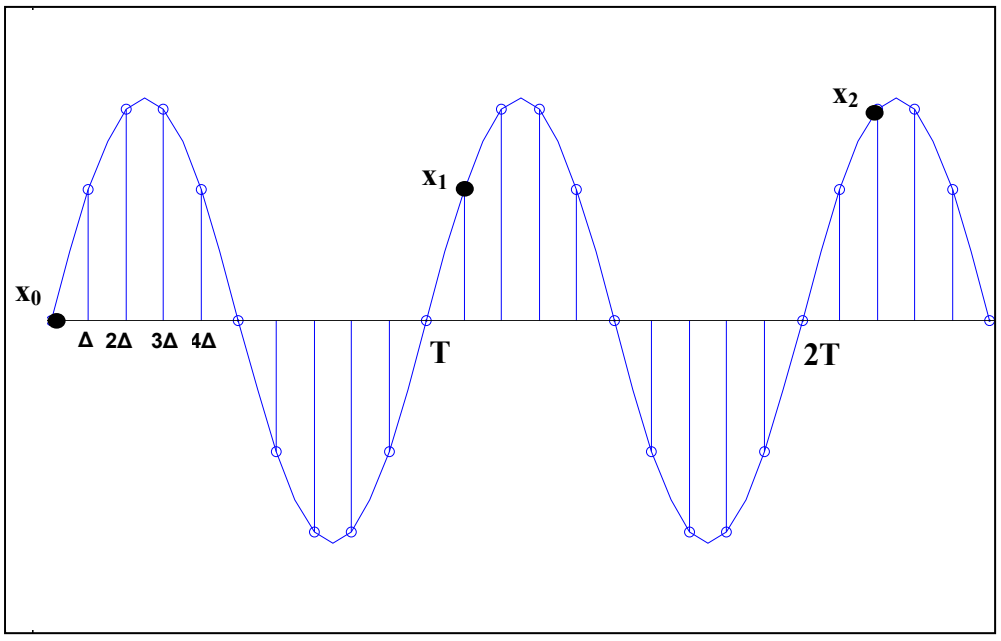

Figure 2-21: Equivalent time sampling

In a UWB radar system, the receiver must be able to catch the reflected pulses. This requirement points a real-time sampler, but real-time sampler for this application must have wide bandwidth and very high sampling rate. This is a challenge to the sampler and requires a special design. Since a real-time sampler that is capable of sampling UWB pulses could not be obtained, an equivalent-time

sampler is used in the experimental setup by accepting some constrains on the performance of the radar.

As mentioned, equivalent-time samplers can handle sampling periodically repeating signals; consequently the scene observed by the radar must be nearly static. If a target in the scene moves, the arrival time of the reflected pulse changes at each trigger pulse. Consequently, equivalent time sampler can not successfully sample the pulse.

To increase SNR in the conventional radar systems, collected pulses are coherently integrated. This also applies for the UWB radar. Remember that the integration improvement factor is called as the improvement in SNR when a number of pulses are integrated. It is defined as

$I_i(n) = \frac{(S/N)_1}{(S/N)_n}$, where $(S/N)_n$ is the required SNR per pulse when n pulses are integrated. [23]

If n pulses are coherently integrated, then the integration improvement factor is $1/n$ or in other words the integration gain is n. In the TDS8200 scope, it is also possible to use integration. It coherently integrates a number of collected waveforms and averages them. This increases SNR by a value proportional to the number of averaged waveforms. While doing so, the equivalent-time sampler needs the collected pulses to be identical, or the scene to be static, for a much more time that is proportional with the number of waveforms to be averaged. Here, there is a trade-off between high SNR and motion detection capability of the radar.

By using the experimental setup, both moving and static scenes are observed. The system has a good performance with static scenes as given in chapter 5, but has limitations in dynamic scenes as given in chapter 4.

2.5.4 SNR OF THE SYSTEM

SNR of an UWB radar system varies much with the level of radio frequency (RF) interference, radar cross-section of the target and the material of the wall between the radar and the target. Considering these effects, a general level of SNR in the experimental setup is calculated.

In the experimental setup, the pulse given in Figure 2-14 is fed to the transmit antenna. Since the impedance of the transmission line and the antenna is 50Ω, the transmitted power for this pulse shape can be calculated as

$$P_t = V^2 \big/ 2R = (1.3V)^2 \big/ 2x50 = 16.9mW \tag{2.13}$$

The gain of the transmit antenna and the receive antenna gains can be taken as 18dBi and 5dBi respectively. This means $G_t \cong 63$ and $G_r \cong 3.2$.

λ can be taken as the wavelength at the median frequency which is 3.3 GHz. $\lambda = 0.09m$ and $\lambda^2 \cong 0.0081m^2$

To work with unit radar cross-section (σ), a man can be taken as a target since it has a RCS of nearly 0 dB ($1m^2$) at the UWB frequencies [24].

Boltzman constant (k) is 1.38 x 10-23 j/°K, T is 300°K and bandwidth B is nearly 12 GHz. The noise figure for the 5867 amplifier is given as 5dB typical [29] and considering also the sampling scope, noise figure of the receiver (F_n) can be taken as 10dB or simply 10.

In the experimental setup, a 20cm ytong wall was used as the sample wall. As given in chapter 3 (section 3.3.1), the loss for this wall is calculated as ~13.4dB, then the two way wall loss (L_{wall}) is $\sim 2 \times 13.4dB \approx 26.8dB \approx 478$.

Putting these values into the SNR equation and considering a moderate range of 5 meters,

$$SNR = \frac{P_t G_t G_r \lambda^2 \sigma}{(4\pi)^3 R^4 k T B_R F_n L_{wall}} = \frac{16.9 \times 10^{-3} \times 63 \times 3.2 \times 0.0081 \times 1}{(12.56)^3 \times 5^4 \times 1.38 \times 10^{-23} \times 300 \times 12 \times 10^9 \times 10 \times 478} \tag{2.14}$$

$$SNR = \frac{P_t G_t G_r \lambda^2 \sigma}{(4\pi)^3 R^4 k T B_R F_n L_{wall}} \cong 0.092 \cong -10.36 dB \quad (2.15)$$

This SNR level is really low. For increasing the SNR, a number of received pulses can be integrated in trade-off with decreasing the capability of detecting moving objects. For coherently integrating 50 pulses, as given in section 2.1, the target must not move more than $\lambda/8$ in the acquisition time of the pulses. It takes ~2sec for the scope to acquire the required number of samples, since it is an equivalent time sampling scope. The number of points in a waveform is set to 4000 and for 50 waveforms $50 \times 4000 = 200000$ samples are required. It samples one point from the signal at each trigger pulse. When the PRF is 500kHz (maximum rate of the pulse generator), the scope is trigged at each pulse at 2μsec. The acquisition is expected to last for $200000 \times 2 \times 10^{-6}\ \text{sec} = 400 m\,\text{sec}$, but it is measured as ~2sec since it also includes the processing time for averaging and the transfer time of the data to the PC over GPIB. In this period, target must not move more than $\lambda/8 = 0.0125 m$. In other words, coherent integration of 50 pulses is possible if the target is moving with a velocity less than $0.0062\, m/\text{sec} = 0.62\, cm/\text{sec}$, which means nearly a static target. The SNR with integration is

$$SNR = \frac{P_t G_t G_r \lambda^2 \sigma\, G_{proces\,\sin g}}{(4\pi)^3 R^4 k T B_R F_n L_{wall}} \cong 0.092 \times 50 \cong 4.6 \cong 6.63 dB \quad (2.16)$$

As seen from the equations, the experimental setup is not suitable for working in dynamic scenes, because of the required acquisition time of the sampling scope. When working in static scenes, it is also possible to further increase number of integrated pulses and consequently the SNR.

2.6 COMMERCIAL UWB THROUGH THE WALL RADAR SYSTEMS

In this part, some through the wall imaging systems in the market are given. Time Domain Corporation is the most advanced firm which has a group of

proven products. Radar Vision 2 is the enhanced version of Radar Vision, which is the first through the wall radar system of the firm. It detects the motion of people behind walls and shows the motion location on the scene map by the help of a 2-D graphical display. The features of this system are given in **Table 2-2**.

Table 2-2: Features of RadarVision 2

Emission Type	Coded UWB pulses
Bandwidth	2.1 – 5.6 GHz
PRF	10 MHz
Transmit Power	50 microwatts
Unobstructed Line of Sight	30 feet through wood, brick, gypsum wall & 20cm solid concrete
Horizontal Modes	0 to 9 ft, 0 to 15 ft and 0 to 30 ft
Range Accuracy	± 3 feet (± 1 feet typical)
Field of view	± 60° (horizontal) ± 45° (vertical)
Weight	4.5 kg
Dimensions	22” x 14.5” x 5.5”

Figure 2-22: Picture of Radar Vision 2

Soldier Vision is the product of Time Domain Corporation that is designed for the military applications. It has a higher range of detection compared to the Radar Vision 2 and has a 10 m stand-off distance.

Table 2-3: Features of Soldier Vision

Emission Type	Coded UWB pulses
Bandwidth	1-3.5 GHz
PRF	10 MHz
Transmit Power	1.5 mW (average)
Unobstructed Line of Sight	20 meters through wood, brick, gypsum wall & 20cm solid concrete
Horizontal Modes	0 to 3m, 0 to 5m and 0 to 10m
Range Accuracy	± 1 m (± 0.5 m typical)
Field of view	± 60° (horizontal) ± 45° (vertical)
Range Resolution	~20 cm range ±2 ft at 10 m in cross-range
Pulse Width	<1.5 ns
Antenna Type	11 transmit and 11 receive spiral antenna
Antenna Gain	1 dBi
Weight	4.5 kg
Dimensions	56cm x 35.5cm x 20.3cm

Figure 2-23: Picture of Soldier Vision

Cambridge Consultants, the firm that has over 20 years experience in designing and developing radar systems, designed products also in the UWB radar category. Prism-200, that is their second generation product after Prism-100, offers providing 3D feedback on the location and movement of people inside buildings on a color display.

Table 2-4: Features of Prism-200

Emission Type	UWB
Center Frequency	1.7 – 2.2 GHz
Transmit Power	-10dBm / MHz
Detection Range	Up to 15 m and 40 cm thick wall
Field of view	±70°(horizontal) ±70°(vertical)
Range Resolution	30 cm
Display	2D and 3D colour display
Weight	3kg
Dimensions	305 × 450 × 210mm

Figure 2-24: Picture of Prism-200

There are also other UWB through the wall radar systems, but there is not information on the features of them. These systems are Xaver-800 (Camero), Man Portable Sense Through The Wall System (CACI), Radar Flashlight (Georgia Tech), 2D-CPR (Hugues) and MDR-1A (Hugues).

CHAPTER 3

UWB SHORT PULSE PROPAGATION & REFLECTION

3.1 BACKGROUND FOR PROPAGATION & REFLECTION

UWB communication systems promise excellent indoor alternative due to through-the-wall propagation (penetration) capabilities. This property of UWB technology, also make it candidate for the through the wall surveillance. The main reason is low signal attenuation at low frequencies [25]. While telling the advantage of UWB signals, this sentence also gives a hint about the main challenge of the propagation analysis which is the difference in behavior of different frequency components forming the UWB signal.

We know that, any periodic waveform can be represented as a linear combination of sinusoidal signals and this is called Fourier series representation. Consider

$$x(t) = x(t+T) \text{ for all t,} \tag{3.1}$$

then x(t) can be written as :

$$x(t) = \sum_{k=-\infty}^{+\infty} a_k e^{jk\left(2\pi/T\right)t} = \sum_{k=-\infty}^{+\infty} a_k e^{jkw_0 t} \tag{3.2}$$

where fundamental frequency $w_0 = 2\pi/T$ [26]

UWB waveforms can also be represented as Fourier series. Think of an UWB pulse generator, like the one in our experimental setup, with a PRF of 500 kHz. The generated pulses can be represented as a Fourier series with fundamental frequency of 500 kHz (500000 Hz).

$$x(t) = \sum_{k=-\infty}^{\infty} a_k e^{j2\pi k 500000\, t} \tag{3.3}$$

Propagation parameters are different for each frequency component. Let we focus on a single frequency as given in [25]. Assuming steady-state time-harmonic electro-magnetic fields, a TEM (transverse electromagnetic) plane wave propagating in the +z direction can be represented as $E(z,w) = E_0 e^{-\gamma z}$ where $w = 2\pi f$ and radian frequency (f is the frequency in Hz) and γ is the complex propagation constant defined as

$$\gamma(w) = \alpha(w) + j\beta(w) = jw\sqrt{\mu\varepsilon} \tag{3.4}$$

where α(Np/m) is the attenuation constant, β(rad/m) is the pahse constant, ε and μ are respectively the permittivity and permeability of the material. For non-magnetic materials, μ can be taken as μ_0.

Accounting for the dielectric losses the permittivity can be replaced by complex permittivity $\varepsilon(w) = \varepsilon'(w) - j\varepsilon''(w)$ where $\varepsilon'(w) = \varepsilon_r \varepsilon_0$ is the real permittivity (relative permittivity $\varepsilon_r \geq 1$) and ε'' is the imaginary part that corresponds to the dielectric loss. The ratio of the imaginary and real parts of the permittivity is called as loss tangent, that is $p(w) = \tan\delta = \varepsilon''(w) \big/ \varepsilon'(w)$.

Also the conductivity loss can be modeled by adding a term to the imaginary part of the permittivity. Then the complex permittivity is

$$\varepsilon(w) = \varepsilon'(w) - j\left(\varepsilon''(w) + \sigma(w) \big/ w\right) \tag{3.5}$$

where $\sigma(w)$ is the macroscopic conductivity and the loss tangent is replaced by an effective loss tangent of the form

$$p_e(w) = \frac{\varepsilon'' + \sigma / w}{\varepsilon'} = \frac{\varepsilon''}{\varepsilon'} + \frac{\sigma}{w\varepsilon'} \tag{3.6}$$

Using effective loss tangent, a complex effective relative permittivity is defined as

$$\varepsilon_{re}(w) = \varepsilon_r(w)\left[1 - jp_e(w)\right] \tag{3.7}$$

and consequently, the complex propagation constant is written as

$$\gamma(w) = \frac{jw}{c}\sqrt{\varepsilon_{re}} = \frac{jw}{c}\sqrt{\varepsilon_r\left(1 - jp_e\right)} \tag{3.8}$$

where c is the speed of light.

Using the definitions made up to now, for a TEM plane-wave propagating in a lossy material we can write

$$E(z,w) = E_0 e^{-\gamma(w)z} = E_0 e^{-j\beta(w)z} e^{-\alpha(w)z} \tag{3.9}$$

where

$$\alpha(w) = \frac{w}{c}\left\{\frac{\varepsilon_r}{2}\left[\sqrt{1+p_e^2} - 1\right]\right\}^{1/2} \text{ Np/m} \tag{3.10}$$

$$\beta(w) = \frac{w}{c}\left\{\frac{\varepsilon_r}{2}\left[\sqrt{1+p_e^2} + 1\right]\right\}^{1/2} \text{ rad/m} \tag{3.11}$$

When propagating, if the electromagnetic wave impinges on another medium with a different intrinsic impedance, it also experiences a reflection [27]. To simplify the analysis of the reflection phenomena, assume that both medium are lossless and the incident wave is normal to the boundary. The incident electric and magnetic field vectors are

$$E_i(z) = a_x E_{i0} e^{-j\beta_1 z} \quad \text{and} \quad H_i(z) = a_y \frac{E_{i0}}{\eta_1} e^{-j\beta_1 z} \tag{3.12}$$

where $\eta = \sqrt{\mu/\varepsilon}$ is called the intrinsic impedance of the medium with μ and ε.

Because of the discontinuity at z=0, incident wave is partially reflected back. For the reflected wave $a_{kr} = -a_z$

$$E_r(z) = a_x E_{r0} e^{j\beta_1 z} \quad \text{and} \quad H_r(z) = (-a_z) \times \frac{1}{\eta_1} E_r(z) = -a_y \frac{E_{ro}}{\eta_1} e^{j\beta_1 z} \tag{3.13}$$

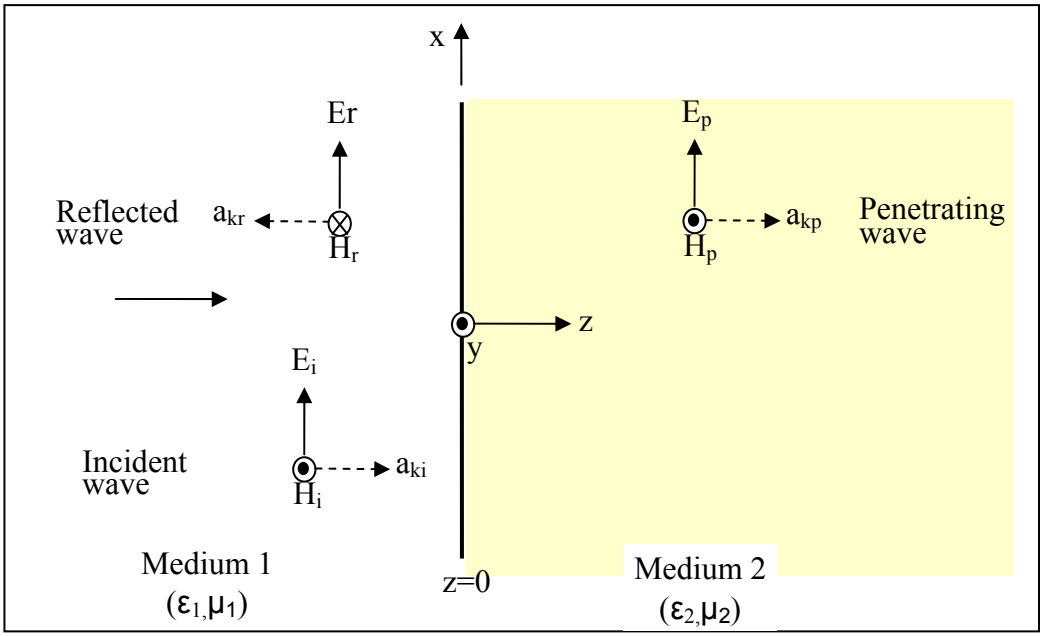

Figure 3-1: Plane wave incident normally on a plane dielectric boundary

For the penetrating wave $a_{kp} = a_z$

$$E_p(z) = a_x E_{p0} e^{-j\beta_2 z} \text{ and } H_p(z) = a_z \times \frac{1}{\eta_2} E_p(z) = a_y \frac{E_{po}}{\eta_2} e^{-j\beta_2 z} \tag{3.14}$$

The directions of E_r and E_p vectors in Figure 3-1 are arbitrarily drawn, because depending on the relative magnitudes of the dielectric parameters of the two medium their directions may be opposite due to sign change of E_{r0} and E_{p0}. To determine E_{r0} and $E_{p0,}$ the boundary condition equations must be solved for electric and magnetic fields.

$$E_{io} + E_{r0} = E_{p0} \qquad \text{and} \tag{3.15}$$

$$H_{io} + H_{r0} = H_{p0} \qquad \text{or} \qquad \frac{1}{\eta_1}(E_{io} - E_{r0}) = \frac{E_{p0}}{\eta_2} \tag{3.16}$$

The solution of the two gives

$$E_{ro} = \frac{\eta_2 - \eta_1}{\eta_2 + \eta_1} E_{i0} \qquad \text{then} \qquad \frac{E_{ro}}{E_{i0}} = \frac{\eta_2 - \eta_1}{\eta_2 + \eta_1} = \Gamma \tag{3.17}$$

and

$$E_{po} = \frac{2\eta_2}{\eta_2 + \eta_1} E_{i0} \qquad \text{then} \quad \frac{E_{po}}{E_{i0}} = \frac{2\eta_2}{\eta_2 + \eta_1} = \tau \tag{3.18}$$

The ratio of E_{r0}/E_{i0} is called the *reflection coefficient* and the ratio E_{p0}/E_{i0} is called the *transmission coefficient*. Reflection and transmission coefficients are related by the equation:

$$1 + \Gamma = \tau \qquad \text{(normal incidence)} \tag{3.19}$$

These definitions also apply when the medium are dissipative, means when η_1 and/or η_2 are complex.

There is a special case of the complex intrinsic impedance for good conductor, the medium for which $\sigma / w\varepsilon >> 1$ [27]. Metallic walls and metallic objects are examples of good conductors that the wave can encounter while propagating. Using the above relation the dielectric constant for the good conductor can be rewritten as

$$\varepsilon_{conductor} = \varepsilon - \frac{j\sigma}{\omega} = \varepsilon\left(1 + \frac{\sigma}{j\omega\varepsilon}\right) \cong \varepsilon \frac{\sigma}{j\omega\varepsilon} = \frac{\sigma}{j\omega} \tag{3.20}$$

Putting this in the intrinsic impedance equation of the good conductor

$$\eta_{conductor} = \sqrt{\frac{\mu}{\varepsilon_{conductor}}} \cong \sqrt{\frac{j\omega\mu}{\sigma}} \tag{3.21}$$

For $\sigma \to \infty$, the intrinsic impedance is negligibly small, so $\eta_{conductor} \cong 0$. Then the reflection and transmission coefficients are

$$\Gamma = \frac{\eta_2 - \eta_1}{\eta_2 + \eta_1} \cong \frac{-\eta_1}{\eta_1} = -1 \text{ and } \tau = \frac{2\eta_2}{\eta_2 + \eta_1} \cong \frac{0}{\eta_1} = 0 \tag{3.22}$$

This means that the pulse is totally reflected back by inverse polarity when it encounters a good conductor.

The velocity of the wave propagating in the medium is also frequency dependent. In a medium with μ and $\varepsilon(\omega)$, the velocity of the wave is $\upsilon = 1/\sqrt{\mu\varepsilon(\omega)}$.

According to the given equations in this part, propagation is carried out for individual frequency components of the UWB pulse, which are then recombined to yield the resulting post propagation pulse shape [14].

3.2 SIMULATIONS OF PROPAGATION & WALL PENETRATION

Since the propagation analysis for the UWB signals must be done by solving electromagnetic equations, it necessary to use some tools for the analysis. I also used a FDTD (The Finite Difference Time Domain) based algorithm given in [28] to make some simulations. The Matlab code of [28] is modified for this purpose.

In this section, first the propagation of UWB pulses from lower dielectric to higher dielectric medium and from higher dielectric to lower dielectric medium cases will be analyzed. Then based on those analyzes, the wall penetration phenomena will be explained. For simplicity, it is assumed that the waves are always normally incident to the plane boundary between two mediums and the mediums are lossless.

3.2.1 PULSE PROPAGATION TO HIGHER DIELECTRIC MEDIUM

A Gaussian pulse will be used in the simulations. Assume medium one is free air while medium two, higher dielectric medium, is a lossless dielectric with $\varepsilon_2 = 2\varepsilon_0$.

$$\varepsilon_1 = \varepsilon_0 \text{ and } \mu_1 = \mu_0 \qquad \Rightarrow \eta_1 = \sqrt{\mu_0 / \varepsilon_0} \tag{3.23}$$

$$\varepsilon_2 = 2\varepsilon_0 \text{ and } \mu_2 \cong \mu_0 \qquad \Rightarrow \eta_2 = \sqrt{\mu_0 / 2\varepsilon_0} \tag{3.24}$$

Then $\eta_2 \cong 0.7\eta_1$ and

$$\Gamma = \frac{\eta_2 - \eta_1}{\eta_2 + \eta_1} = \frac{0.7\eta_1 - \eta_1}{0.7\eta + \eta_1} \cong -0.18 \quad \Rightarrow E_{ro} = -0.18E_{i0} \tag{3.25}$$

$$\tau = \frac{2\eta_2}{\eta_2 + \eta_1} = \frac{1.4\eta_1}{0.7\eta_1 + \eta_1} \cong 0.82 \qquad \Rightarrow E_{po} = 0.82E_{i0} \tag{3.26}$$

For verifying these coefficients and observe the reflection & transmission, a simulation is made by using the code in [28]. Figure 3-2 below shows the

simulation result is consistent with the above calculations. While the pulse is propagating into higher dielectric medium, an inverted reflection from the boundary plane is observed.

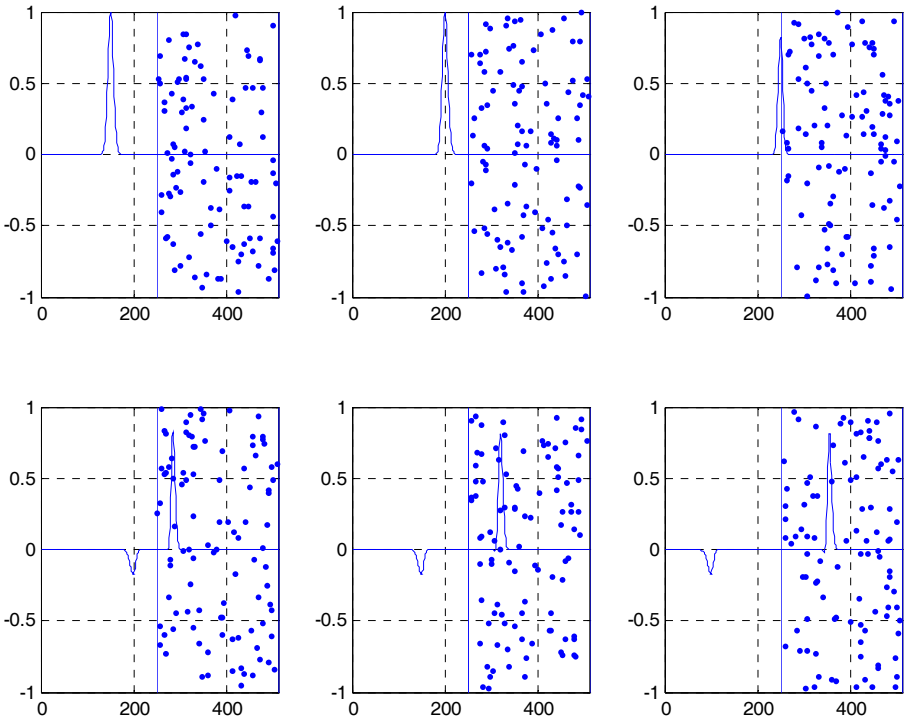

Figure 3-2: Pulse propagation to higher dielectric medium

3.2.2 PULSE PROPAGATION TO LOWER DIELECTRIC MEDIUM

For this propagation scenario, the reverse case of the previous can be used. Now medium one is with $\eta_1 = \sqrt{\mu_0/2\varepsilon_0}$ and medium two is free air, so $\eta_2 = \sqrt{\mu_0/\varepsilon_0}$. The ratio between these impedances is $\eta_1 \cong 0.7\eta_2$ and

$$\Gamma = \frac{\eta_2 - \eta_1}{\eta_2 + \eta_1} = \frac{\eta_2 - 0.7\eta_1}{\eta_2 + 0.7\eta_1} \cong 0.18 \quad \Rightarrow E_{ro} = 0.18E_{i0} \tag{3.27}$$

$$\tau = \frac{2\eta_2}{\eta_2 + \eta_1} = \frac{2\eta_2}{\eta_2 + 0.7\eta_2} \cong 1.18 \quad \Rightarrow E_{po} = 1.18E_{i0} \tag{3.28}$$

The propagation is simulated and Figure 3-3 shows the simulation results. From the figure it can be observed that, electric filed intensity increases when the pulse propagates into a lower dielectric medium.

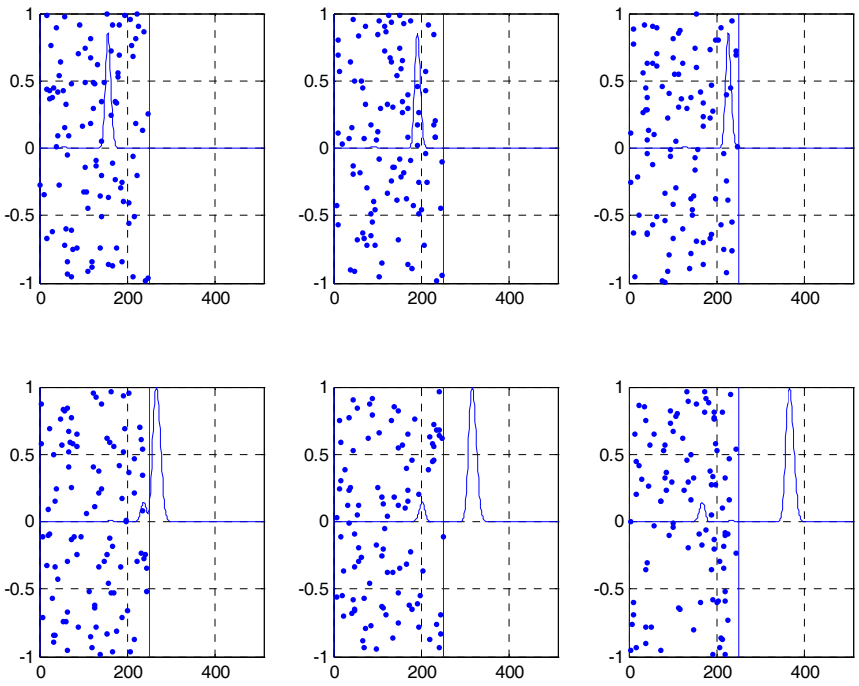

Figure 3-3: Pulse propagation to lower dielectric medium

3.2.3 PROPAGATION THROUGH THE WALL

Through the wall propagation scenario is the combination of the previous two scenarios. While the pulse propagates in air, it encounters a wall, a higher dielectric medium compared to air. At the boundary plane, pulse is divided into two: an inversely reflected pulse back and the forward propagating pulse into the wall. In the wall, pulse attenuates as it propagates and reaches the second boundary plane between the wall and air. At this boundary, again the pulse is divided into two: a positively reflected pulse back into the wall and the forward propagating pulse into air with higher electric field intensity. The pulse propagating backwards in the wall also reaches the first boundary plane again and passes to air. The simulation result of this scenario is given in Figure 3-4.

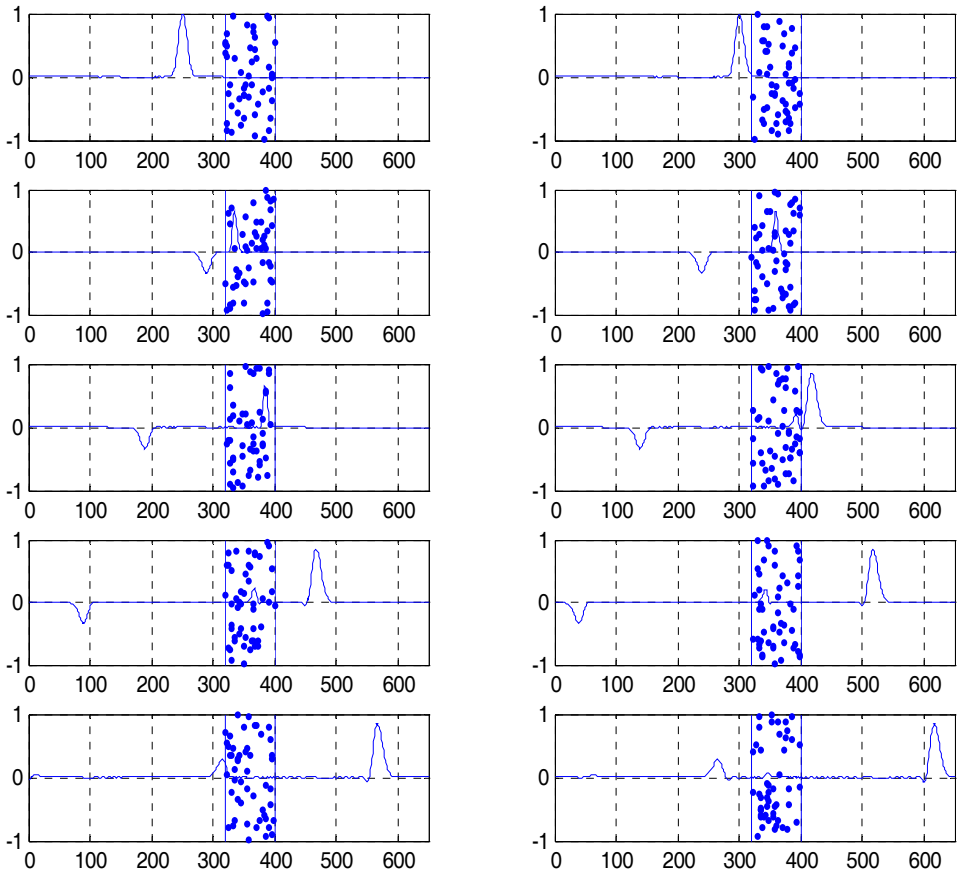

Figure 3-4: Pulse penetrating a wall with $\varepsilon_r = 4\varepsilon_0$

3.3 EXPERIMENTS & PROCESS OF COLLECTED DATA

In this section, the results of some experiments are examined to compare the consistency of the theory is with the practice. In addition, the collected data are processed to identify the scene.

3.3.1 WALL PENETRATION EXPERIMENT

For observing the effect of the wall penetration on the pulse shape, a simple experiment is done. UWB pulse is transmitted from the tx antenna and

received by the rx antenna without/with a wall between them as in Figure 3-5. The wall is built up by ytong blocks of 20 cm width.

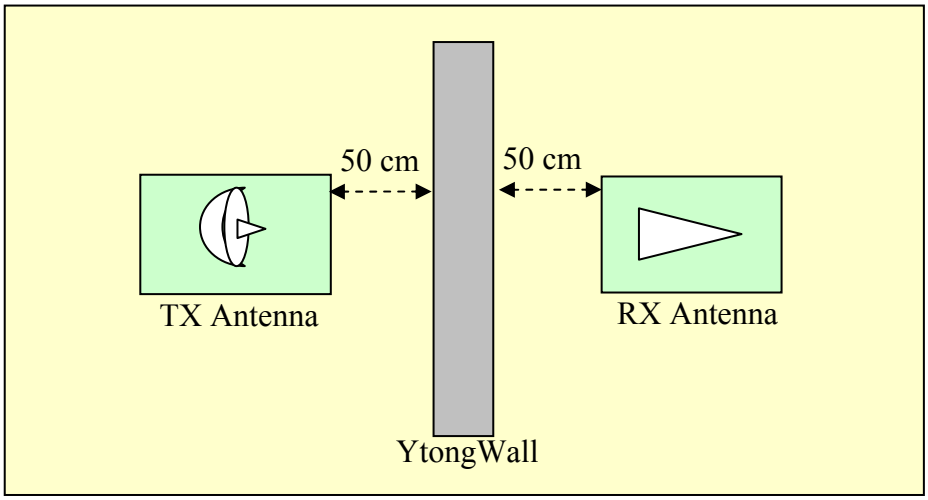

Figure 3-5: Wall penetration experiment

As seen in Figure 3-6, without the wall, width of the pulse is 300ps and the peak is 280mV. With the wall, the width of the pulse expands to 350ps and the peak level degrades to 60 mV.

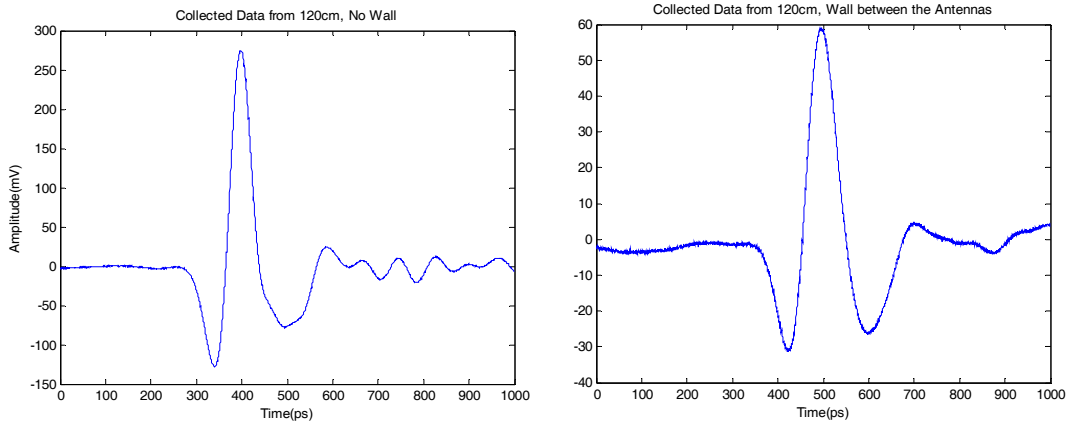

Figure 3-6: Comparison of the collected pulses with/without the wall

The increase in the width and smoother shape means that high frequency components of the pulse are attenuated more by the wall or in other words, low

frequency components can penetrate the wall more easily. By considering the peak voltage levels, it can be said that, the attenuation in this 20cm ytong wall and the reflection from its front side (tx antenna side) causes a total loss of ~13.4dB in the pulse received by the rx antenna. Approximate attenuation values for some materials at different frequencies are given in **Table 3-1**[25].

Table 3-1: Approximate attenuation values for some materials

Frequency	**Attenuation (dB/m)**			
GHz	**Plywood**	**Door**	**Bricks**	**Concrete**
1	-	15	36	70
2	48	25	54	72
3	65	31	70	75
4	85	40	90	80
5	100	47	110	85
6	120	57	125	90
7	138	63	146	100
8	152	72	-	-
9	172	80	-	-
10	187	88	-	-
11	208	97	-	-
12	225	102	-	-

3.3.2 REFLECTIONS FROM A WALL & AN OBJECT BEHIND

For collecting reflections, tx and rx antennas are placed directed towards a wooden wall with thickness of 2.5 cm and behind the wall a metal cabinet is placed as in Figure 3-7.

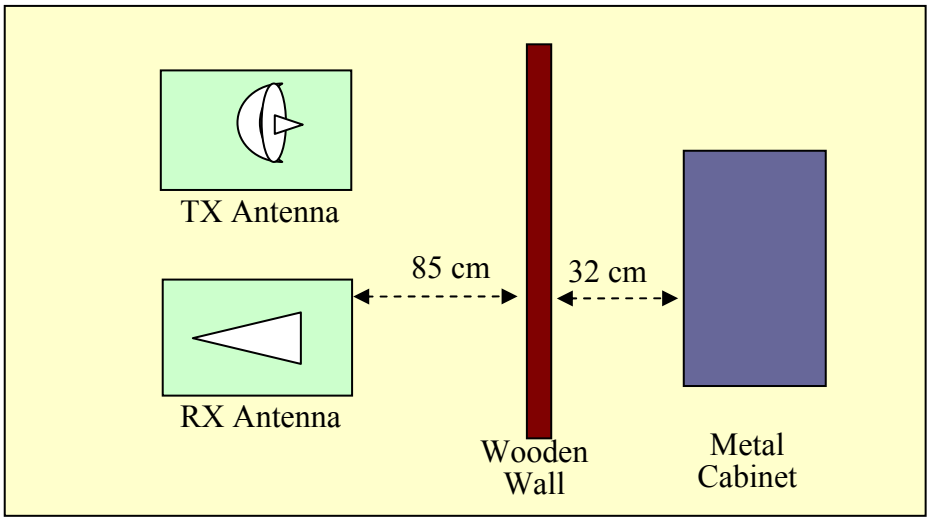

Figure 3-7: Antenna locations for collecting reflections

By considering the background given in this chapter and looking at the scene, we can comment on the propagation of the pulse and the reflections. The wooden wall is a dielectric with a higher permittivity compared to the air; so an inverted reflection is expected from the front face and a non-inverted reflection from rear face of the wall as studied in section 3.2.3. When the part of the pulse propagating through the wall reaches the cabinet, it can not penetrate through its metallic surface which is a good conductor. It would be inverted and completely reflected back. The plot of the collected signal by the rx antenna is given in Figure 3-8. The figure is consistent with the above comments.

It can be said that if the scene is known, some one can comment on the possible reflections from the scene. Then it is sure that, the inverse case is possible. In other words, if the back reflected signal is decomposed into pulses then one can comment on the scene by observing them. Through the wall surveillance is based on this is the idea.

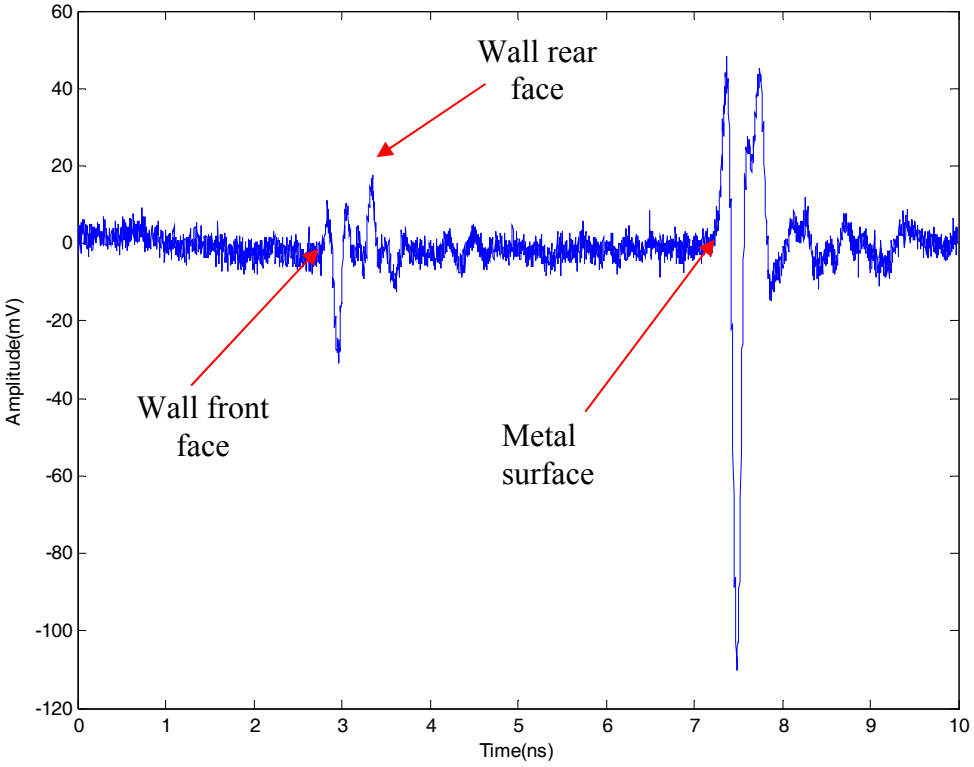

Figure 3-8: Collecting reflections from the wall & the cabinet

An algorithm for decomposing the signal into pulses is proposed as follows:

1. A template pulse is correlated with itself (convolved with time flipped version of itself) and the maximum of this correlation is taken as unit magnitude.
2. A threshold is calculated by the user defined dB level below the unit magnitude.
3. Then the data is correlated with the template pulse and the maximum correlation index of the data array and the maximum correlation ratio is defined in terms of the unit magnitude.
4. In a second array called clean, this correlation ratio is stored at the same index.

5. The template pulse is multiplied with the correlation ratio and subtracted from the data. In this way the first pulse is defined and cleaned from the data

6. Returned to step 3 and the algorithm goes on processing until the maximum correlation value decreases below the defined threshold level.

By this algorithm, the collected signal can be decomposed into pulses and the clean array contains the relative magnitudes at the related index. Figure 3-9 shows the cancellation of the pulses in descending correlation.

The algorithm detects and cancels the front and rear face reflections of the wall successfully, since the template matches these pulses well. But when the pulse passes through the wall, it is distorted and it does not match the template as well as before. Consequently, the reflection from the metal surface could not be cancelled at one step. After one cancellation, the remaining signal level also gives correlation over the threshold level and a few more cancellations are done around the exact reflection. At each cancellation the relative amplitude of the cancelled pulse is written at that index. Figure 3-10 shows the output of the algorithm.

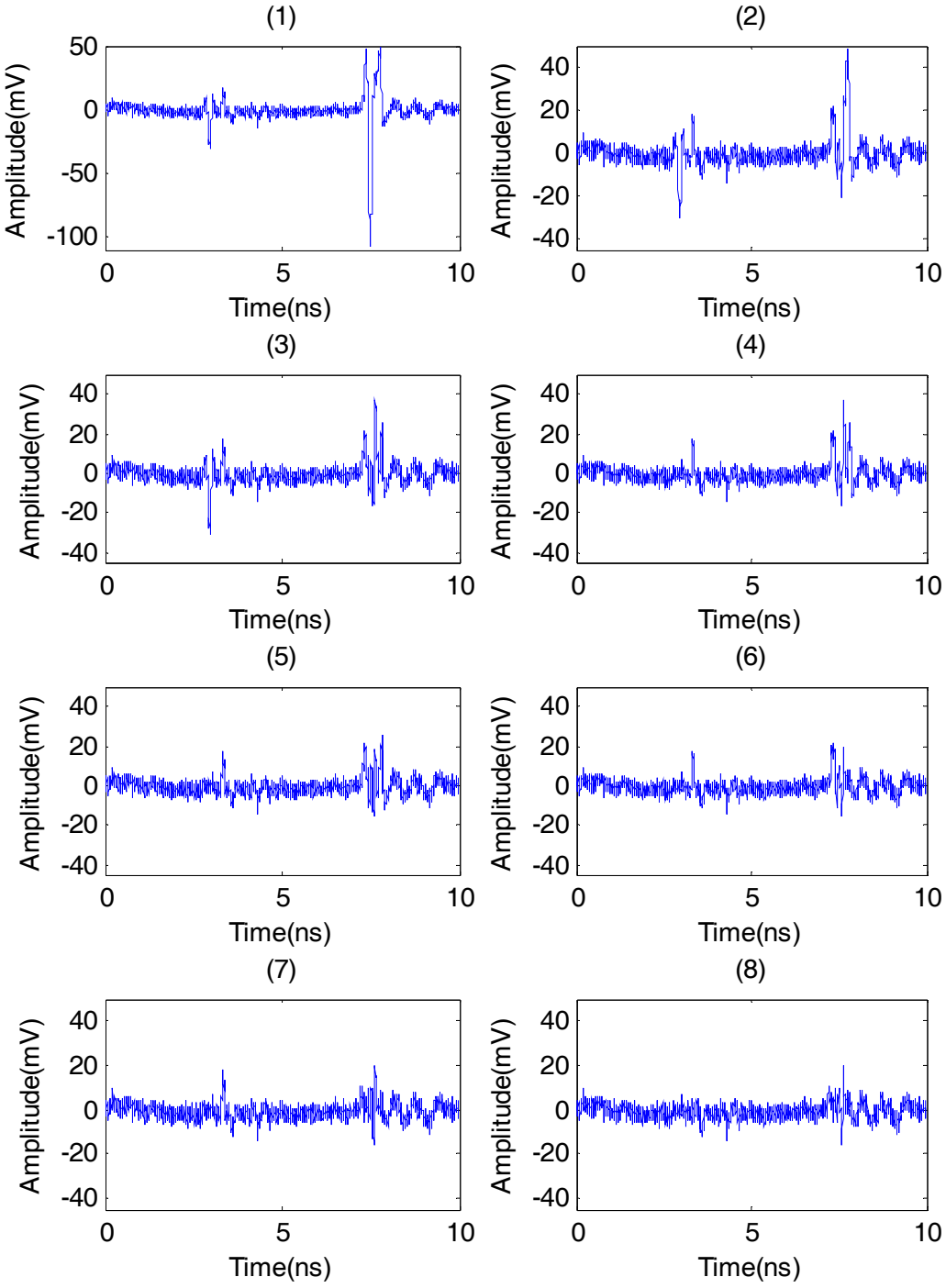

Figure 3-9: Cancellation of pulses in descending correlation order

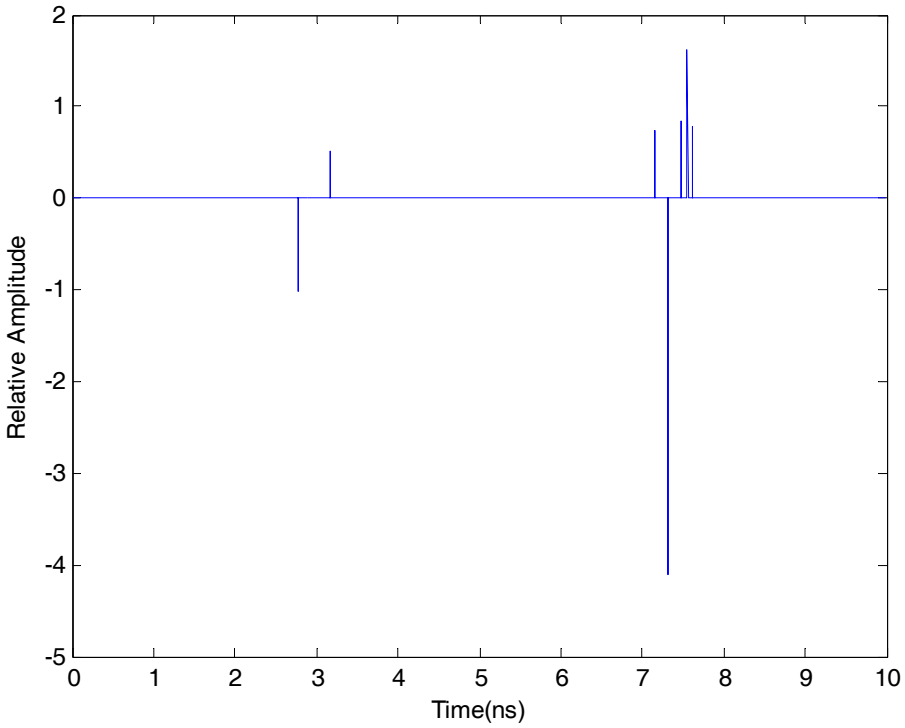

Figure 3-10: Output of the algorithm

We can make the following comments on Figure 3-10. The first inverted and direct reflection pair is a sign of a wall. The other reflections are not easy to explain. While expecting again an inverted reflection from the front face of an obstacle, we observe a direct reflection which is not reasonable. At this point a comment can be done also considering the expected distortions. The inverted reflection at ~7.4ns is very strong compared to the reflection from the wall, although it is coming from behind of the wall (attenuated by the wall two times). Then it is probable that this strong inverted reflection is from a metal surface.

As we observe, discretely detecting each reflected pulse is not a straight forward process as the pulse shape is distorted by the wall. Instead, using imaging algorithms on the collected reflection data and presenting an image to the operator can be more practical.

CHAPTER 4

1-D STUDIES : DETECTION OF RESPIRATION

4.1 VITAL PARAMETERS DETECTION

Remote sensing the vital parameters of a person is studied for many years since it has a potential for various applications. In 70's and 80's microwave doppler radars were developed for sensing the respiratory movements [3]. Georgia Tech Research Institute (GTRI) worked on radar vital signs monitors (RVSM) under the sponsorship of United States Department of Defense (DoD) and experiments were conducted on determining which wounded soldiers on the battlefield had vital signs. GTRI also designed a RVSM for the 1996 Atlanta Olympics that is used for the evaluation of athletes' performances [4].

For the application of remote sensing of vital parameters, UWB radar technology is better than the microwave Doppler radar technology. Since UWB pulses have good material penetration properties, through the wall measurement of vital parameters is possible by UWB. Some applications of this technology can be listed as [3]

- Through-the-wall health monitoring of victims in hostage rescue

- Detecting people trapped in the debris and monitoring their condition
- Continuous assessment of a patient's respiration and heart rates in a non-invasive manner
- Vital-signs monitoring for lie-detector tests and athletic performance monitoring

4.2 DATA COLLECTION AND RESPIRATION DETECTION

In the experimental setup, tx & rx antennas are placed in front of a wooden wall and a man behind the wall as shown in Figure 4-1. The generated pulses are transmitted by the tx antenna. The reflected pulses from the man are collected by the rx antenna and sampled by TDS8200 sampling scope.

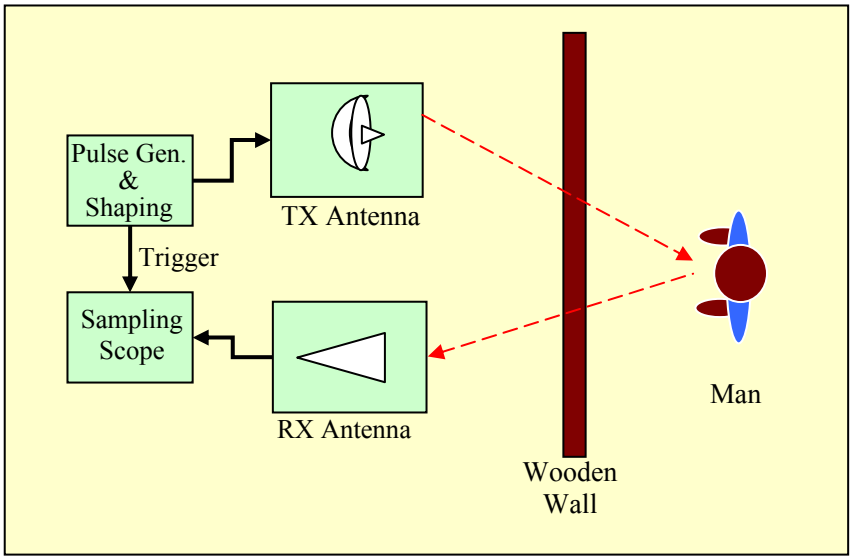

Figure 4-1: Experimental setup for breathing detection

As the man breathes, a change in the distance of man to the antenna system is expected due to his chest cavity movement. The nominal distance of the man to the system is

$$d_0 = \left\| x_m - x_{rx\_antenna} \right\| + \left\| x_m - x_{tx\_antenna} \right\| \tag{4.1}$$

As the man breathes his chest cavity expands and contracts periodically. This causes a periodical change in the measured distance. It fluctuates sinusoidally around the nominal distance d_0 by the respiration frequency f_b.

$$d(t) = d_0 + \Delta_d . \sin(2\pi f_b t) \tag{4.2}$$

where Δ_d is the maximum deviation from the nominal distance. If the scene is static except the breathing man, then the channel impulse response can be modeled as

$$h(t,\tau) = \sum_i \alpha_i \delta(\tau - \tau_i) + \alpha_b \delta(\tau - \tau_b(t)) \tag{4.3}$$

where t is the observation time or slow time and τ is the fast time. In this model each $\alpha_i \delta(\tau - \tau_i)$ corresponds to a target that is static along slow time t and $\alpha_b \delta(\tau - \tau_b(t))$ corresponds to the breathing man. $\tau_b(t)$ shows the change in the time of arrival of the pulses reflected from the man .

$$\tau_b(t) = \frac{d(t)}{c} = \frac{d_0 + \Delta_d . \sin(2\pi f_b t)}{c} = \tau_0 + \tau_d . \sin(2\pi f_b t) \tag{4.4}$$

Say $g(t)$ models the total distortion on the transmitted pulses caused by the channel (tx & rx antennas, amplifiers and the reflection phenomena from a surface) complete channel response can be written as

$$h_{channel}(t,\tau) = g(t) * h(t,\tau) \tag{4.5}$$

Then, received reflections from the channel is

$$r(t,\tau) = \underbrace{p(t) * g(t)} * h(t,\tau) \tag{4.6}$$

$$r(t,\tau) = \quad p_r(t) \quad * \quad h(t,\tau) \qquad , \; p_r(t) \text{ is the received pulse shape} \tag{4.7}$$

$$r(t,\tau) = \sum_i \alpha_i p_r(\tau - \tau_i) + \alpha_b p_r(\tau - \tau_b(t)) \tag{4.8}$$

The measurements are done at discrete observation instants in slow time $t = mT_o$ and also in fast time τ, the received signal is sampled by the scope at the

sampling period $\tau = nT_s$. Say a total number of N_o observations are taken and the sampling window is $N_s T_s$ seconds long. Then, after collecting the reflections from the scene a $N_s x N_o$ matrix is obtained.

For achieving maximum SNR, this matrix is matched filtered with the expected return pulse shape. The template for this return pulse shape is obtained by averaging the collected reflections from a flat metallic surface. Figure 4-2 shows the pulse shape p(t) that is fed to the tx antenna and the returned pulse shape $p_r(t)$ which is sampled by the scope after passing through the rx antenna and the amplifier are given.

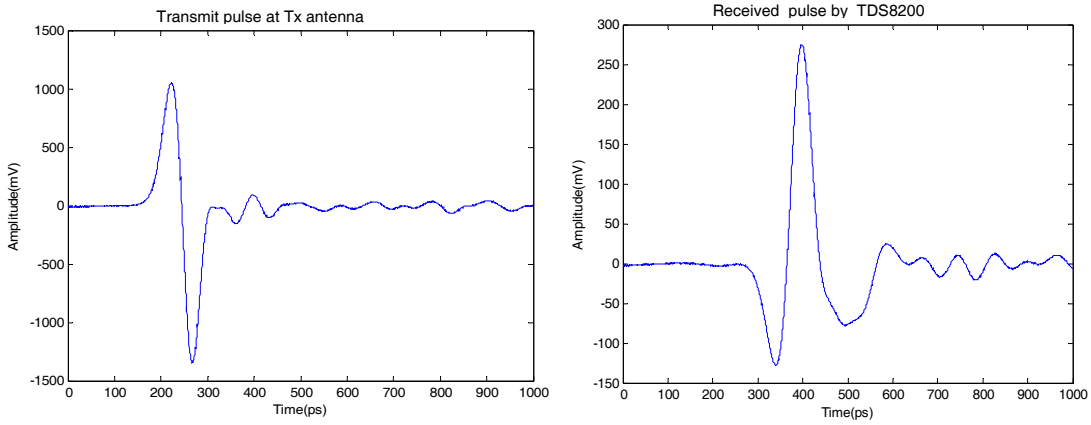

Figure 4-2: Transmitted pulse p(t) and received pulse $p_r(t)$

The maximum acquisition length of TDS8200 is 4000 samples and for 150 observations data is collected in a 4000x150 matrix form. After matched filtering, the matrix is imaged by *imagesc* function of Matlab and *colormap* is set to *grayscale*. The resultant image is given in Figure 4-3. In the image, distance of the wall (location in fast time) does not change with slow time as expected; but the distance of the man changes around a nominal value in a periodical manner. The fluctuation in the distance along the slow time is the sign of a breathing man behind the wall.

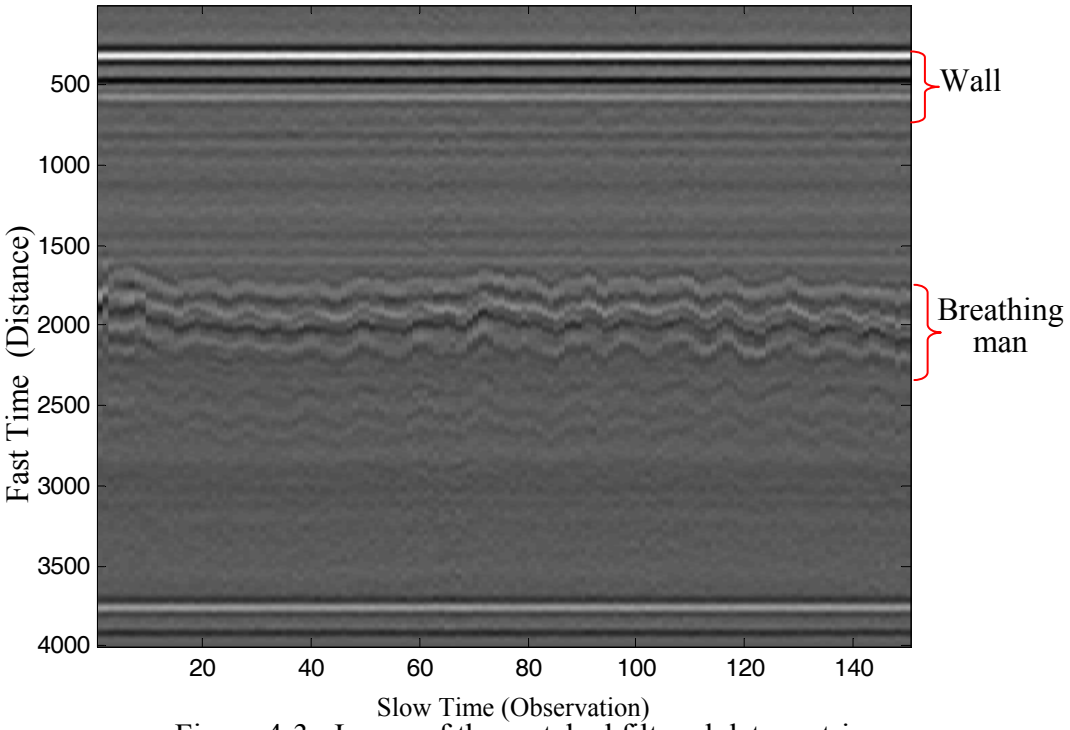

Figure 4-3: Image of the matched filtered data matrix

After filtering, the data matrix is processed by the suggested successive-channel estimation algorithm, which was given in chapter 3.3.2. By this function, each observation or in other words each column is decomposed into reflections. The fast time can be converted to distance by the relation of

$$d = d_{offset} + n.d_{increment} \quad \text{, where n is the fast time} \tag{4.9}$$

and for this experiment $d_{offset} = 77{,}5cm$ and

$$d_{increment} = {c\tau_{sample}}/{2} = {3.10^{10}.1{,}25.10^{-12}}/{2} = 0{,}01875cm \tag{4.10}$$

When the resultant matrix is plotted by *plot* function, columns each corresponding to one observation are plotted on the same figure. As seen from Figure 4-4, the reflections from the wall are at the same distance in all plots, while the reflections from the man are fluctuating around ~113 cm in distance.

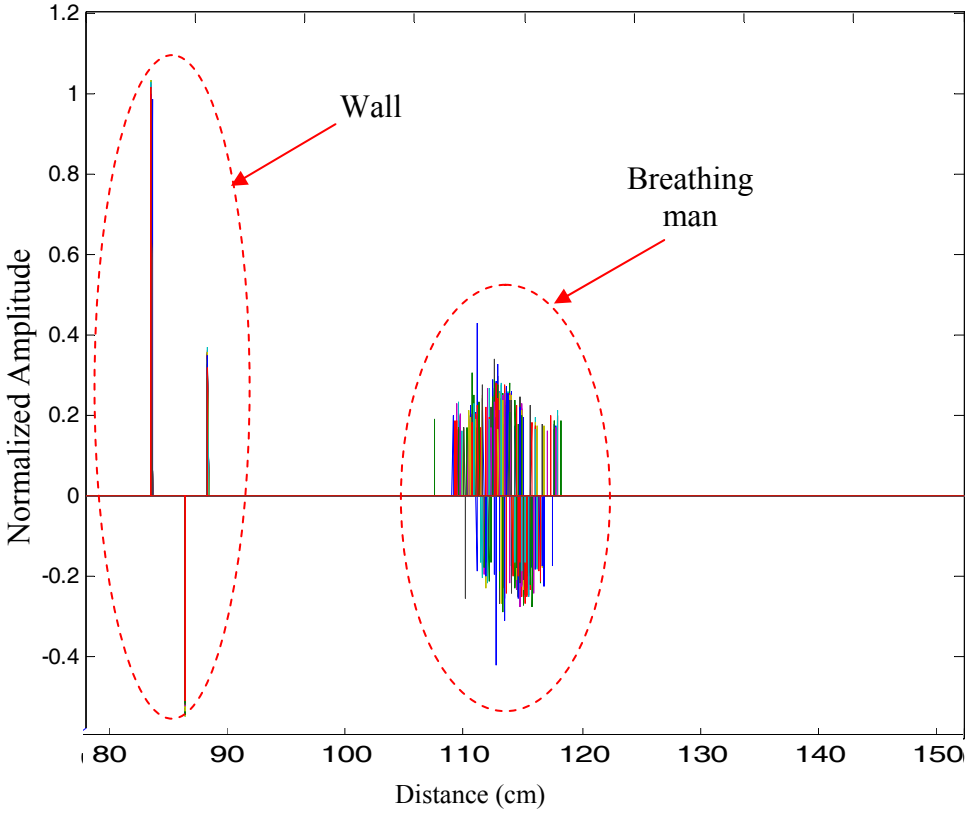

Figure 4-4: Plot of decomposed data

4.3 RESPIRATION RATE ESTIMATION

Although the reflections can be separated and the presence of respiration can be detected from this experimental data; frequency of respiration could not be directly calculated by FFT algorithms. As seen in Figure 4-3, the return signal is not of pure sinusoidal nature, but it is periodic.

Remember that, the sampling scope used in the setup is not a real time sampler, but an equivalent time sampler as mentioned in chapter 2.5.3. Since the equivalent-time samplers shift and sample one point at each trig pulse, they need the sampled signal to repeat itself perfectly. Also for SNR improvement, a number of collected waveforms are averaged in the scope and one observation column in the data matrix is obtained. Averaging corresponds to coherent

integration for the case of perfect repeating waveforms. This experimental data is collected by averaging 10 times. One set of waveform is composed of 4000 sample points and for the case of 10 averages, 40000 samples are required. The PRF in the experimental setup is 500kHz, or in other words the PRI is 2 μsec, means 40000 samples can be collected in $40000x2\mu s = 80ms$.

Real-time scopes need only 10 trigs for 10 averaging, this makes $20\mu s$. Although 80ms time is much longer than $20\mu s$; considering the nyquist theorem, this sampling period seems well enough for sampling the chest movement which can not have a frequency more than 1Hz.

In addition to the problems of equivalent time sampling, the scope produces an output bit stream at every 0.9 seconds on the average. In other words, the collected samples are returned to receiver (computer) at the period of 0.9 seconds. This significantly limits the tracking capabilities of dynamic scenes. The extensive delay in communication between scope and computer is partly related to GPIB standard. There is not a known method by us to improve the communication delay. Figure 4-5 shows the delays between two consecutive observations reaching the computer. As can be noted, there are some observations with ~3 seconds delays due to the problems with GPIB standart and Matlab interface.

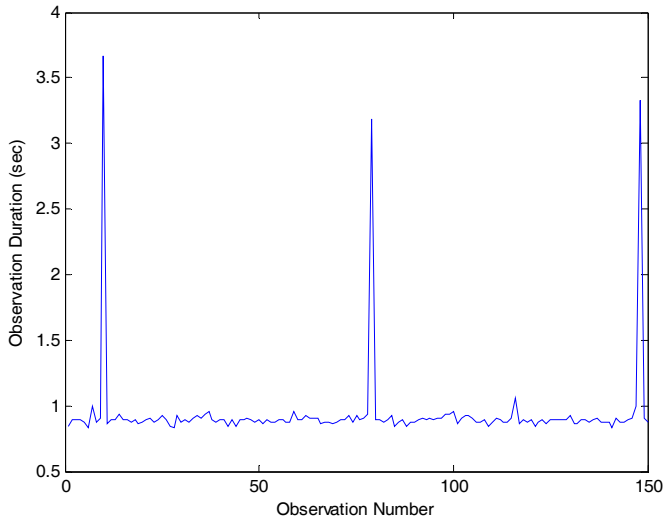

Figure 4-5: Observation times measured in the experiment

On certain conditions, it can be said that if the man's respiration rate is below ~0.5 Hz and he does not move during the observations, his respiration rate could be estimated. An experiment is designed to check the theoretical expectations. For this experiment transmitted pulse shape is changed and the auto-correlation function is improved. (The new pulse shape is obtained by removing one pulse shaper from the pulse shaping network. The details are given in Chapter 5.3.2.3. The auto-correlation of the former pulse shape had -4dB side lobes while the new pulse shape has -7dB side lobes (Figure 4-6).)

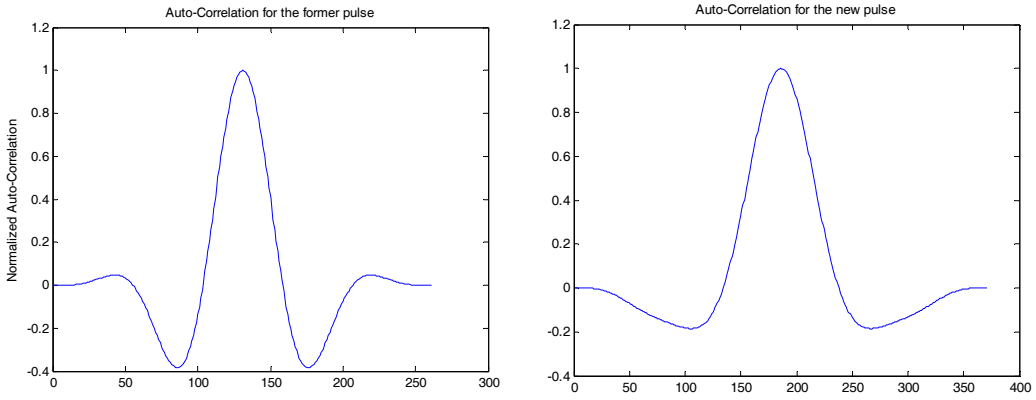

Figure 4-6: Auto-correlations of the former and new pulse shapes

In this new experiment, the man breathed slowly and care has been taken not to move his body during the observations. The image of the collected data is given in Figure 4-7 and the matched filtered image is given in Figure 4-8.

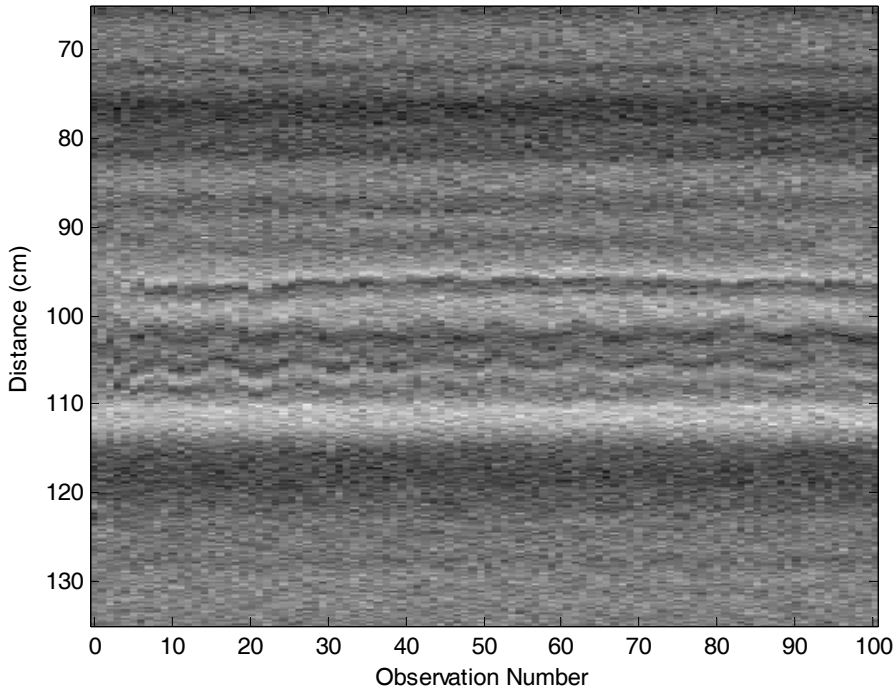

Figure 4-7: Image of the collected data

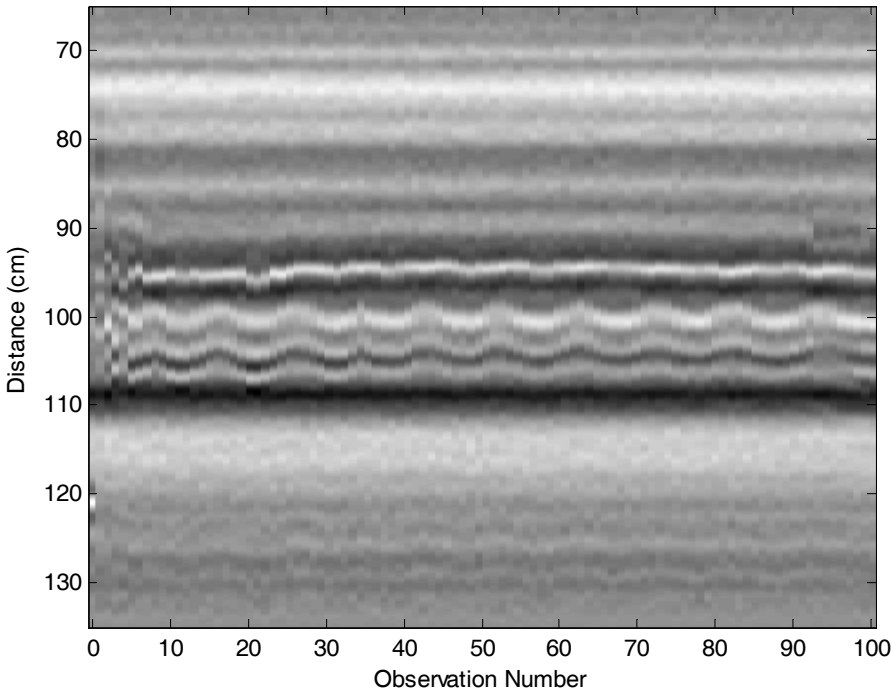

Figure 4-8: Image of the matched filtered data

The respiration movement can be observed in Figure 4-8 between the distances of 100 and 108 cm. For estimating the rate in a candidate piece of the matched filtered image, a simple algorithm can be used as fallows:

- for each column (observation) find the locations of the maximums and write them to an array
- take 256 points of FFT

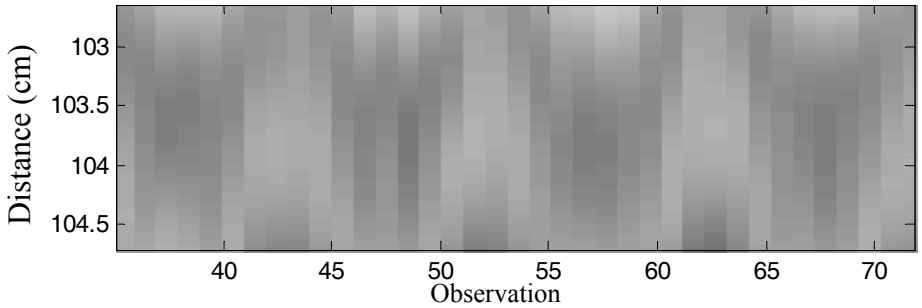

Figure 4-9: A piece of the image in Figure 4-8

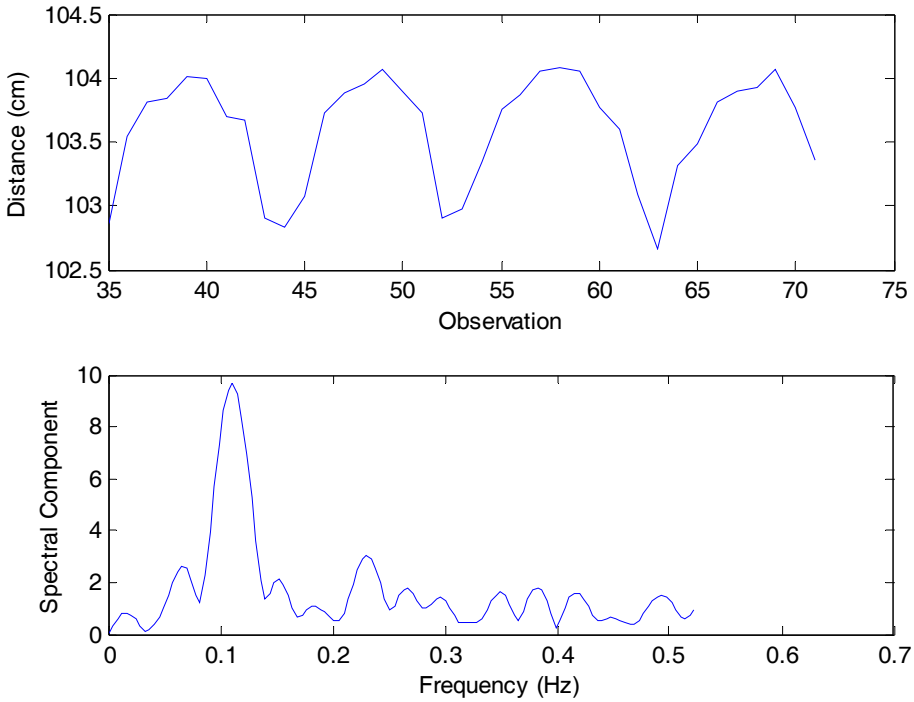

Figure 4-10: Detected movement of the chest and estimated respiration rate

If this algorithm is applied to the piece of image given in Figure 4-9, the maximum locations in distance and 256-points FFT of the variation in the distances can be obtained as given in Figure 4-10 (The experimental system could measure 1 cm variations in the maximum locations and this proves that its range resolution is far better than 1 cm.). The respiration rate is estimated as 0.11 Hz by the algorithm.

This shows that, the frequency information can be extracted from the image by processing the relevant windows of it. To automate the system, a window of 3 cm in distance is chosen and 45 observations are taken for estimating the frequency. Then the suggested breathing frequency estimation algorithm can be summarized as:

- Matched filter the collected data by the template.
- By taking the mean of the observation times, find the sampling period for the FFT.
- Scan the image by sliding the window in both distance and observation axis in an overlapping manner.
- At each time calculate the 256-points FFT in the window and check if there is a dominant frequency component by comparing the maximum value with a threshold of 7.8dB over the mean value.
- If there is a dominant frequency, add the FFT result to the overall FFT. In this way, the common frequency contents will add up.
- When the entire image is scanned, the peak in the overall FFT is the dominant frequency in the image. That is the respiration frequency in our case.

To check the validity of the algorithm, the image in Figure 4-7 is processed by this algorithm and the resultant overall FFT is given in Figure 4-11. By the breathing frequency estimation algorithm, respiration rate in a collected data can be extracted without a priori information.

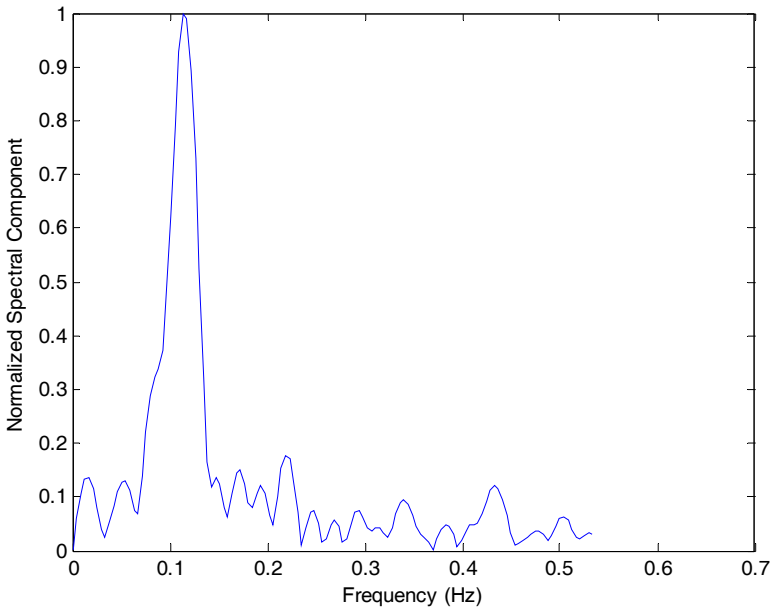

Figure 4-11: Overall FFT of the image

As a result of this chapter, the respiration of a man can be detected behind a wall, and if the man does not move much the respiration rate can be easily estimated by the suggested breathing frequency estimation algorithm.

CHAPTER 5

2-D STUDIES: THROUGH THE WALL IMAGING

5.1 IMAGING BEHIND THE WALLS

In previous chapters it is shown that by the help of UWB pulses, reflections form other side of walls can be obtained and by processing them presence of an object or a man can be detected. Further more; in this chapter it will be proved that imaging of the scene behind a wall is also possible.

First, the most popular way of UWB imaging, using antenna array and back projection algorithm, will be inspected. Then an alternative method which is proposed in this thesis will be presented, using synthetic array and anti-migration algorithm.

5.2 ANTENNA ARRAY & BACK PROJECTION

Most popular method for through the wall imaging is collecting data by an antenna array and processing it by back projection algorithm. Each antenna element in the array collects the reflected pulses from the scene and the distance of the objects can be calculated using the time-of-flight of each reflection. Since

the angle of arrival is not known, each collected pulse can theoretically be from anywhere on the ellipse whose foci are locations of transmit and receive antenna elements. After finding the ellipses for each receive element, the intersection point of these ellipses is found. This intersection point is the location of the target.

For a single transmitter system, say the location of the transmitter is (x_t,y_t), location of each receive antenna element is (x_n,y_n) and the location of the target is (x_i,y_i). Then the distance between the transmit antenna and the target is

$$R_t = \sqrt{(x_i - x_t)^2 + (y_i - y_t)^2} \tag{5.1}$$

and the distance between the target and the receive antenna element is r

$$r = \sqrt{(x_i - x_n)^2 + (y_i - y_n)^2} \tag{5.2}$$

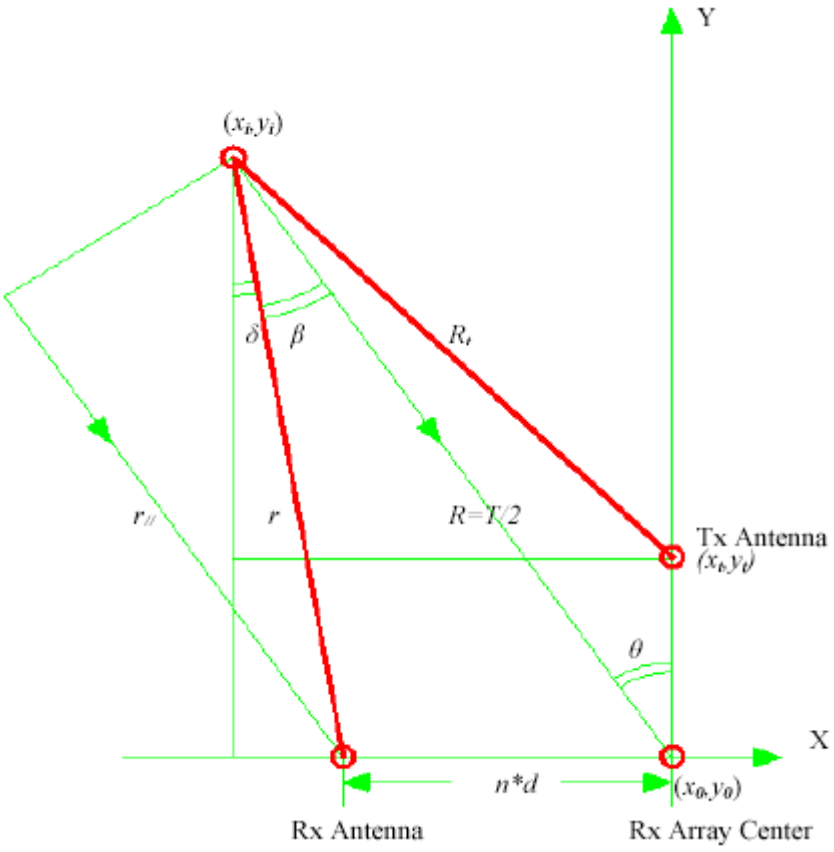

Figure 5-1: Locations of the array elements and target [33]

$$r_{//} = R + nd\sin\theta \tag{5.3}$$

$$\Delta r = r - r_{//} = (R + nd\sin\theta).\left(\frac{1}{\cos\beta} - 1\right) \tag{5.4}$$

For each receive antenna element the range profile function $f_n(t)$ is collected and while forming the image for each location corresponding parts of the range profiles of all receive elements are added. Then the back projected signal at image location (R,θ) is

$$s(R,\theta) = \sum_n f_n(t_n), \text{ where } t_n = \frac{R_t + R + nd\sin\theta + \Delta r}{c} \tag{5.5}$$

This summation is coherent at the points where the received pulses in the range profiles overlap. These points are at the locations of the targets.

The scene shown in Figure 5-2 is used for an UWB imaging application. In this application stepped-frequency UWB is used instead of short pulse UWB, but this application is selected as an example because the reflections are collected by an antenna array and the image is formed by back projection.

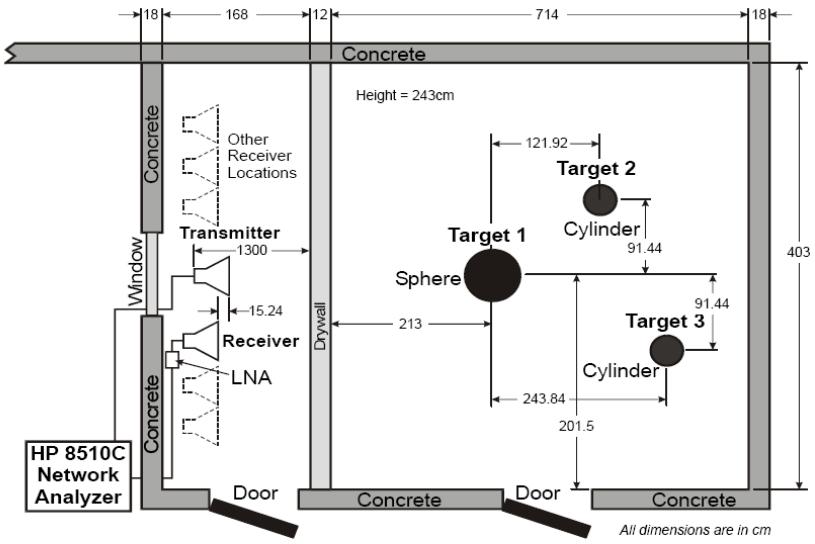

Figure 5-2: Experimental scene for back projection application [33]

In the scene three metallic objects are used as targets, one sphere and two cylinders. The transmit antenna is placed in the center of the receive array. Actually, there is not a receive array, but a receive antenna is moved to different locations and reflections are collected as if there is an array. HP 8510C network analyzer is used as the signal source and receiver.

When the collected data is imaged by back projection, the image shown in Figure 5-3 is obtained. In the figure the drywall is imaged as a curved surface because of its proximity to the transmitter. Actually, all the objects in the image are a bit curved due to the ellipses used in this technique.

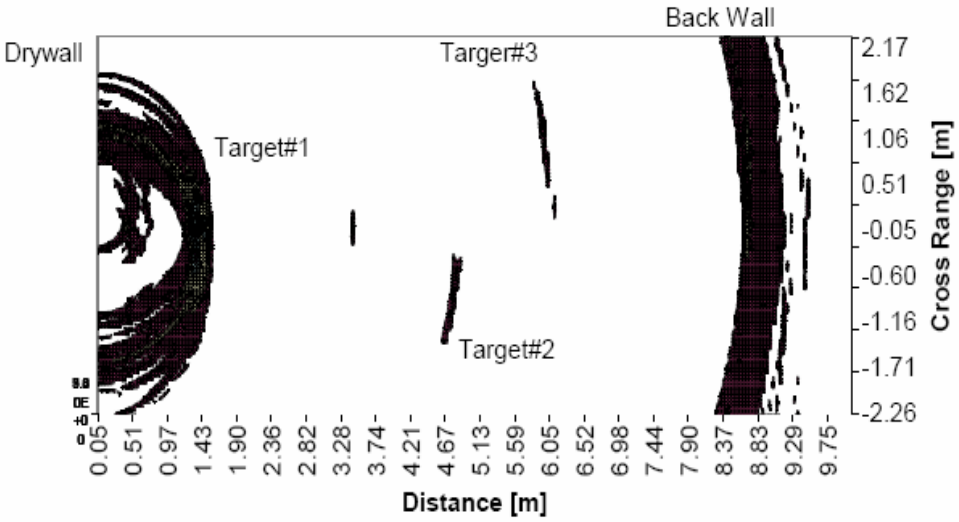

Figure 5-3: Image of the scene formed by back projection [33]

Also it is easily observable that targets get wider in cross-range as they are getting far away from the antennas. This is due to the fact that cross-range resolution decreases as the distance increases in the back projection algorithm.

An improved version of this algorithm is called cross-correlated back projection. This algorithm improves the cross-range resolution of the images nearly to the pulse-width of the UWB signal by cross-correlating array elements with a remote element [33]. This algorithm can be performed in two ways:
point-to-point and intra-pulse cross-correlation. In point-to-point, the range profiles of the receivers are correlated to the range profile of the reference

channel on the point-to-point basis. In the intra-pulse method, the same correlation is calculated but within the pulse duration.

If the reference channel is the k[th] element in the array, M is the total number of sample points in one pulse and T is the sampling period, then the intra-pulse cross-correlation is

$$P(R,\theta)=\sum_{\tau=0}^{M} f_k(t_k).S(R,\theta) \text{ where } t_k=\frac{R_t+kd\sin\theta+\Delta r}{c}+\tau T \qquad (5.6)$$

For M=1, this representation correspond to the point-to-point cross-correlation. By rewriting (6) using (5)

$$P(R,\theta)=\sum_{n}\sum_{\tau=0}^{M} f_k(t_k).f_n(t_n) \qquad (5.7)$$

In this equation the reference channel is assumed to be one of the elements on the array. In [31] it is given that the cross-range resolution can be improved more if the reference channel is selected far away from the array center.

Compare the two images, Figure 5-4 and Figure 5-5, of a scene in which a man and a cylinder are placed behind a drywall. Since the goal is to compare the cross-range resolutions of the images, the targets are located nearly 20m away from the antennas. One of the images is formed by back projection and the other one is formed by cross-correlated back projection.

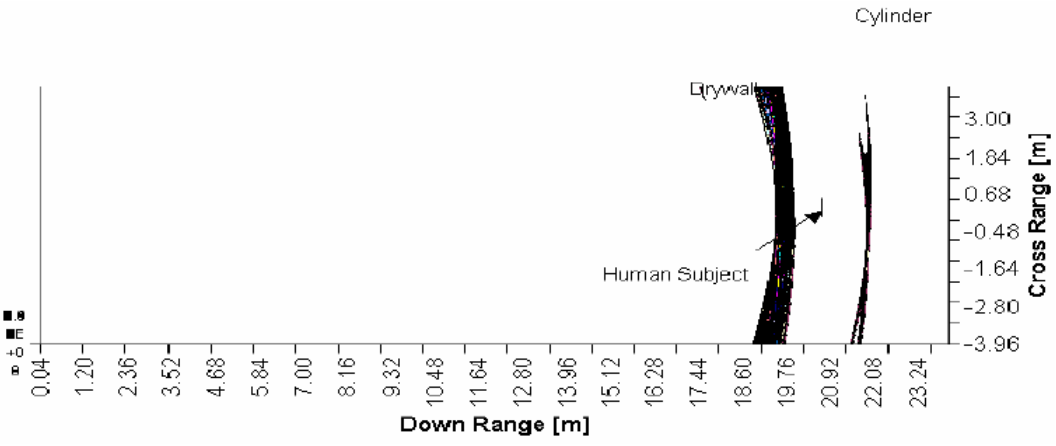

Figure 5-4: Back projection image [33]

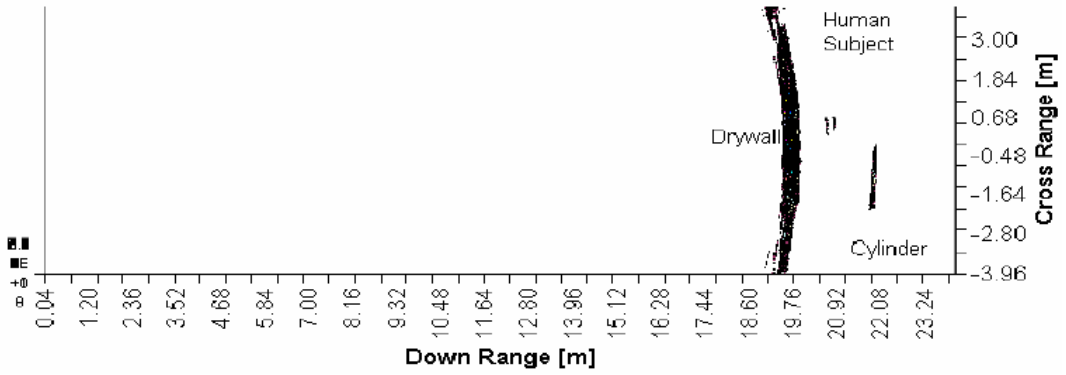

Figure 5-5: Cross-correlated back projection image [33]

The improvement cross-correlation can be easily observed by checking the cylinder in the images. Besides, in the cross-correlated image the man has two layers, front and back faces of his body, as expected from a dielectric material.

As seen from these images back projection or cross-correlated back projection is valid for imaging simple walls such as drywall or wood. These walls have practically no impact on the performance of UWB radar. For thick concrete or ytong walls, the refraction and propagation of the pulse through the wall is more complex. These walls have significant effects on propagation.

The losses caused by concrete and ytong walls are very large compared to the loss of drywall. For drywall with thickness 1.15cm a loss of 0.45dB is given in [25], while for a 20cm concrete wall this value is ~13.6dB. The loss for the 20cm ytong wall used in the setup is measured as ~13.4dB in chapter 3. These are single pass loss values. In imaging, pulses pass through the wall two times; so the losses are twice.

In these back projection applications, a single transmit antenna is used and the scene is illuminated by the radiation of this single antenna. The targets in the scene are usually not illuminated by the center of main lobe of the transmit antenna and similarly the elements in the receive array do not usually receive the reflections from the center of their main lobe. This means, gains of these antennas are not efficiently used in back projection methods. For ytong and concrete wall

cases the loss values are more than 26dB and with the inefficient use of antenna gains, back projection systems may not be able to image the scene.

Due to single transmitter structure of the system, usually incidences of the returned pulses are not normal to the wall. Oblique pulses are shifted (Figure 5-6) in a parallel way due to Snell's law of refraction [27]. Compensating this shift is not easy in the lack of the knowledge of thickness & permittivity of the wall and the angle of arrival. This increases the error and ambiguity in the location of the targets.

Although the cross-range resolutions of the cross-correlated back projection images are better than those of back projection images, these resolutions are not well enough. For example, the cylinder in Figure 5-5 has a diameter of 22.5 cm, but in the image it is observed as a target of ~150 cm wide. If one more cylinder were placed in 75 cm proximity of it, they would be seen as a single wide object in the image.

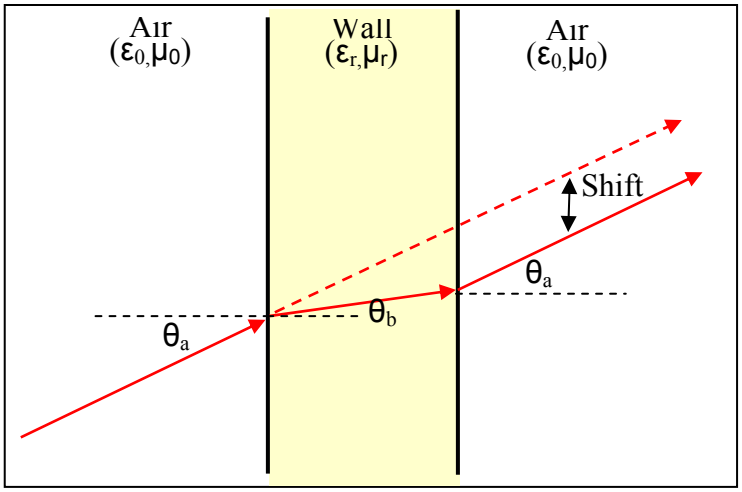

Figure 5-6: Shift due to Snell's law of refraction

5.3 SYNTHETIC APERTURE & ANTI-MIGRATION

Back projection algorithm is a popular algorithm for imaging. This algorithm and the algorithms derived from it are worked commonly for UWB imaging; but as mentioned in the previous section, antenna array and back projection is not the best choice for through the wall imaging. The alternative suggested in this thesis is synthetic aperture and anti-migration algorithm.

In the experimental setup there is a single transmit and single receive antenna. Two antennas are enough for 1-D studies given in chapter 4, but for imaging, an antenna array is necessary. A physical array can not be implemented by two antennas, so by sliding these antennas a synthetic aperture is formed.

The 1-D experimental system is upgraded to a 2-D imaging system by the help of a plate of cardboard. The tripods of the tx and rx antennas are placed on the plate. In this way a mobile antenna system is obtained, where the relative locations of the two antennas in the system are fixed (Figure 5-7).

The first imaging experiment is done for imaging a metallic sphere hanged on a stretched string as in Figure 5-7. A line is drawn on the floor parallel to the string and each 5cm on the line is marked. The tx and rx antennas are placed on the plate as the distance between the centers of the antennas are 46 cm. Then the plate is sequentially slided over these marks and at each mark location pulses are radiated and reflections are collected. The total length of the sliding path is 140cm and the sphere is located 310cm ahead of the midpoint of this path and 114 cm above the floor.

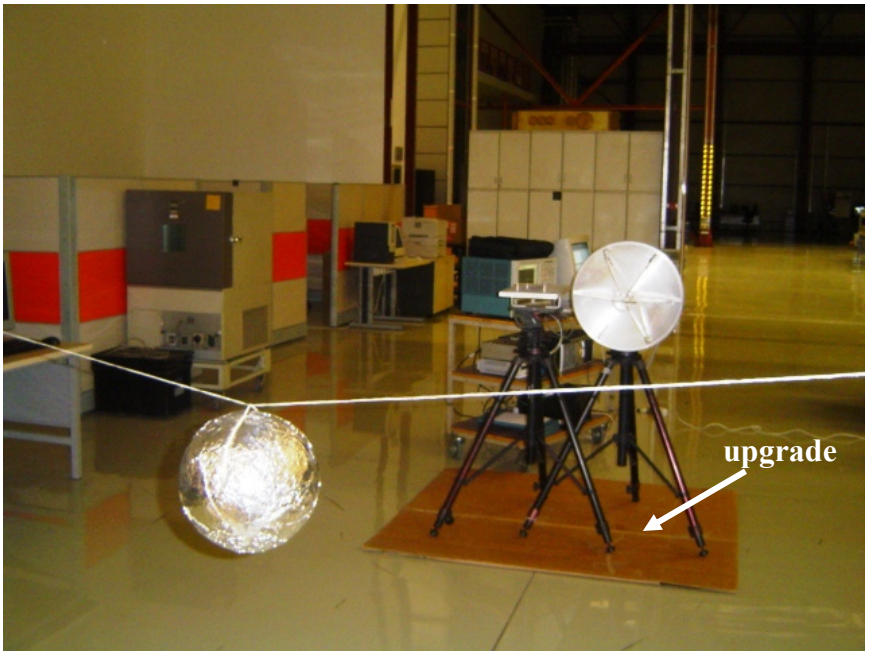

Figure 5-7: SAR imaging experiment of a sphere

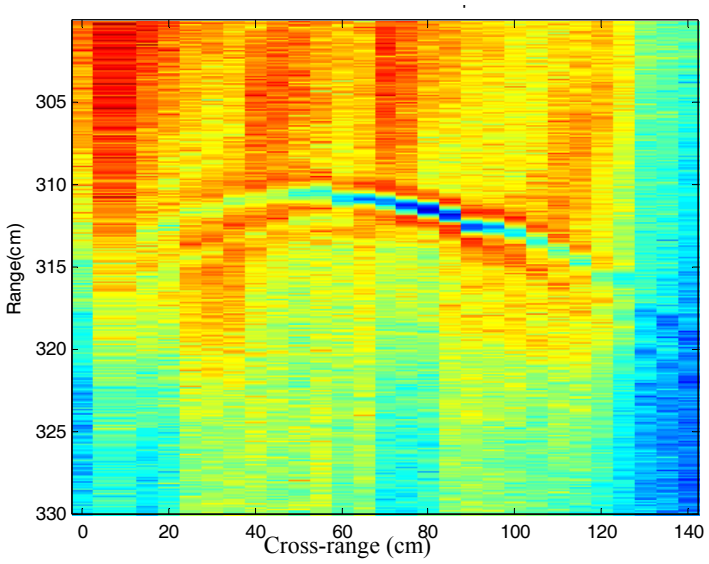

Figure 5-8: Raw SAR image of the sphere

The collected raw data matrix is shown in Figure 5-8. The sphere which has a diameter of 22cm is seen as a curve of length ~100cm. This curve is known as *range migration curve*. It is the range-to-target vs. platform position curve and the range to the target changes as the radar moves along the track. The range is smallest when the radar is aligned with the target and it increases as the radar

moves in either direction as in Figure 5-9. The curvature of the migration curve is related to the ratio between the distance to the target and the length of the track on which the reflections from the target are received. Since the angle of arrival information does not exist, the received reflections at each platform location are recorded in a separate column as if the targets are aligned with the radar. Figure 5-8 is a good example for the range migration curve.

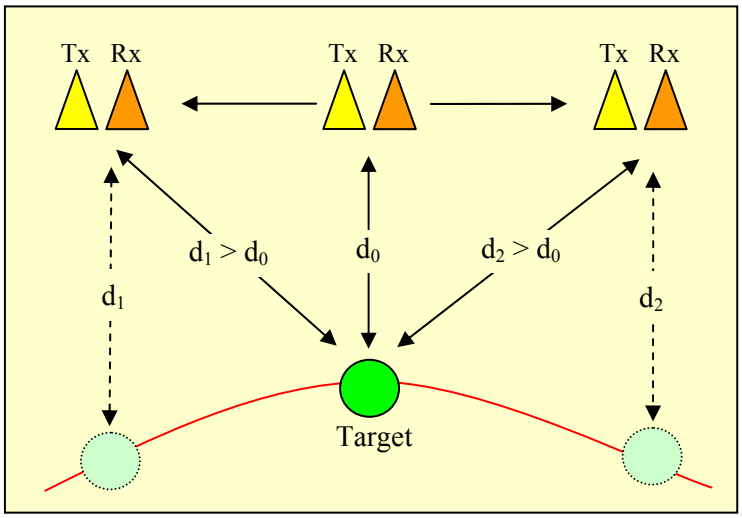

Figure 5-9: Range migration curve

If the curve in Figure 5-8 is observed, one can realize it is not symmetric about the center in the sense of color intensity or in other words, in signal level. This is due to the antenna locations in the experimental system. Tx and rx antennas are two separate antennas and the distance between them are comparable with the range of the targets. As shown in Figure 5-10 when the tx antenna is aligned with the target, the target is illuminated maximum and the collected reflection is maximum. When the rx antenna is aligned with the target, the symmetric case of the previous about the center, the radiation of the tx antenna illuminates the target less and consequently the collected reflection level is less.

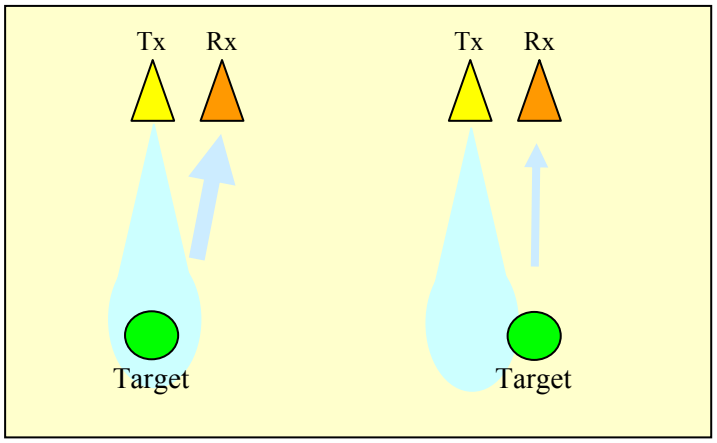

Figure 5-10: Asymmetric range migration curve

5.3.1 ANTI-MIGRATION ALGORITHM

Due to the nature of the data collection technique in SAR application, a migration curve is obtained in the raw data image for each target. Since the formation mechanism of these curves is well understood, an algorithm for handling them can be suggested.

Say the collected data is stored in a *nxm* matrix D[i,j] where each column of D[i,j] is an array $D_j(i)$, that is the collected data at one stop on the motion track. T(i) is the array that is the template for the expected return pulse shape. The array obtained by matched filtering each $D_j(i)$ by T(i) is $M_j(i)$ and the resultant matrix is M[i,j]. Then the suggested anti-migration algorithm can be applied as follows

- Matched filter each observation column of the collected data with the template and obtain the matched filtered data image M[i,j].

$$M_j(i) = D_j(i) * T(i) \tag{5.8}$$

$$M[i,j] = \left[M_1(i) \quad M_2(i) \quad M_3(i) \quad \ldots\ldots\ldots \quad M_m(i) \right] \tag{5.9}$$

- For each pixel M_{ij} in the image, assume this pixel is the center pixel of a migration curve. Calculate r_{ij}, the distance from the location

corresponding to this pixel to the antennas. The real distance in the field which is between two sequential pixels of range axis is

$$d_{increment} = \frac{c\tau_{sampling}}{2}, \text{ where } \tau_{sampling} \text{ is the sampling period} \quad (5.10)$$

and the distance to the antenna center is

$$r_{ij} = d_{increment}.i + d_{offset} \quad (5.11)$$

where d_{offset} is the min distance in the image

- Considering the distance and the track movement, detect the pixels in the neighboring columns that can be on this migration curve (Figure 5-11). For the center pixel M_{ij}, the pixels from the neighboring columns and on the migration curve have a range axis index of

$$s = round\left(\frac{\sqrt{r_{ij}^{\ 2} + [(j-k).d_{track}]^2}}{d_{increment}}\right) \quad (5.12)$$

where d_{track} is the distance between two stops on the track, k is the column number s is the rounded range index value in the k^{th} column.

- Sum the values of these pixels to the pixel which is assumed to be the center. Obtain the new image matrix $N[i,j]$ by the summation results.

$$N_{ij} = M_{ij} + \sum_{k=j-w}^{j+w} M_{sk}, \text{ where } w \text{ is the width for summing} \quad (5.13)$$

$$N[i,j] = \begin{bmatrix} N_{11} & \dots & N_{1m} \\ \vdots & \dots & \vdots \\ N_{n1} & \dots & N_{nm} \end{bmatrix} \quad (5.14)$$

- If that pixel is really the center of a migration curve, then the selected pixels are also on the curve and the sum grows up.

This algorithm is applied to the data in Figure 5-8. By matched filtering the image in Figure 5-12 is obtained. If examined carefully, the effect of matched filtering is not only increasing the SNR, it also corrects the range of the target. In Figure 5-8, the center pixel seems to be at a distance more than 310 cm, but in the

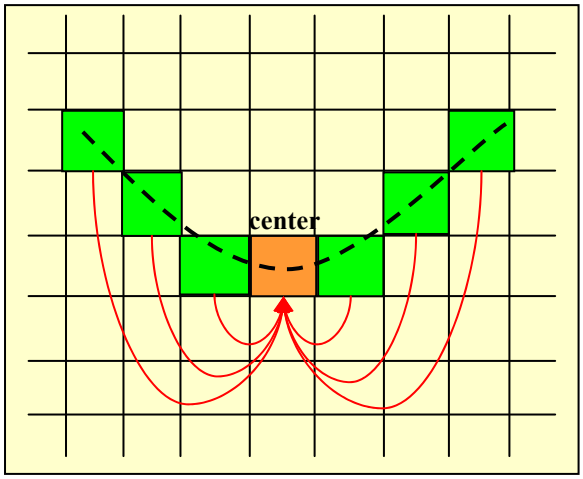

Figure 5-11: Anti-migration algorithm

matched filtered Figure 5-12 it seems to be at the true distance of 310 cm. This is due to the fact that, in the raw image the color intensity is more at the peak of the received pulse, not at the beginning of the pulse. In the matched filtered image, the color intensity is more at the maximum correlation point where the template overlaps the pulse. This point is the beginning of the received pulse and shows the true distance. Obviously, the matched filtering part of the algorithm improves the image in the range axis.

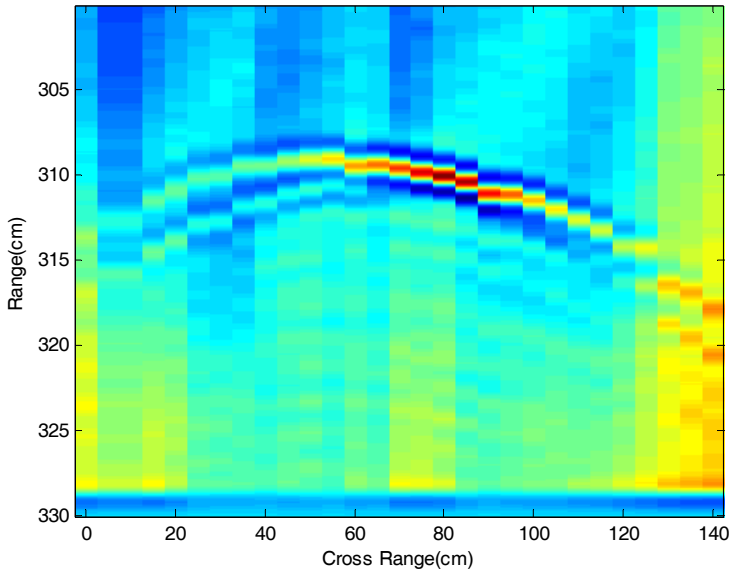

Figure 5-12: Matched filtered SAR image of the sphere

The resultant image of the algorithm is given in Figure 5-13. The migration curve in the raw data image (Figure 5-8) is beaten by the algorithm and the target now extends from 45 to 70 cm the cross-range, which is very reasonable for a sphere with a 22 cm diameter. Also when compared with the images of Figure 5-8 and Figure 5-12, the asymmetric intensity in the target caused by the two antennas of the system is removed. The peak intensity was at the cross-range of 80 cm in those images, where in the resultant image the peak intensity is around 60 cm. This is the center of the migration curve and the true location of the target. This result means, after matched filtering, this second part of the algorithm improves the image in both range and the cross-range axes. The effect of the algorithm can easily be realized by comparing the mesh images of the raw data and output of the algorithm given in Figure 5-14.

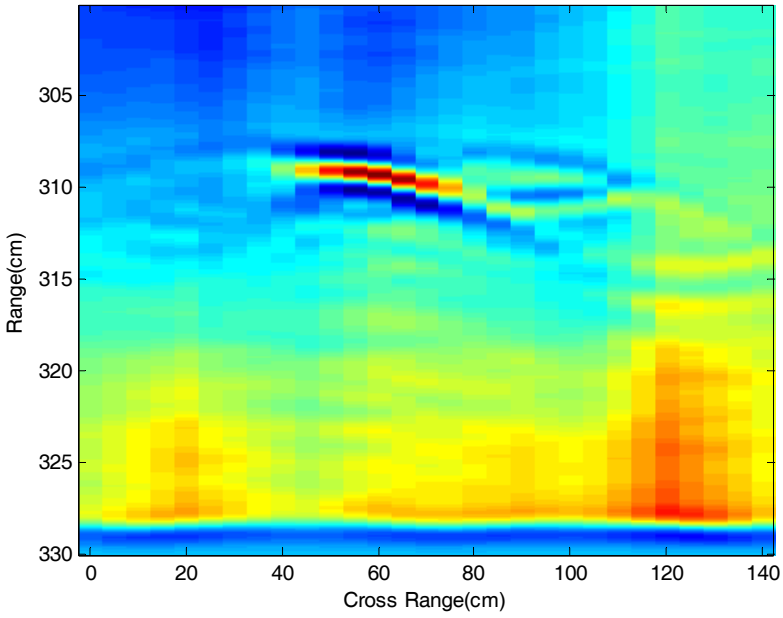

Figure 5-13: SAR image by the Anti-migration algorithm

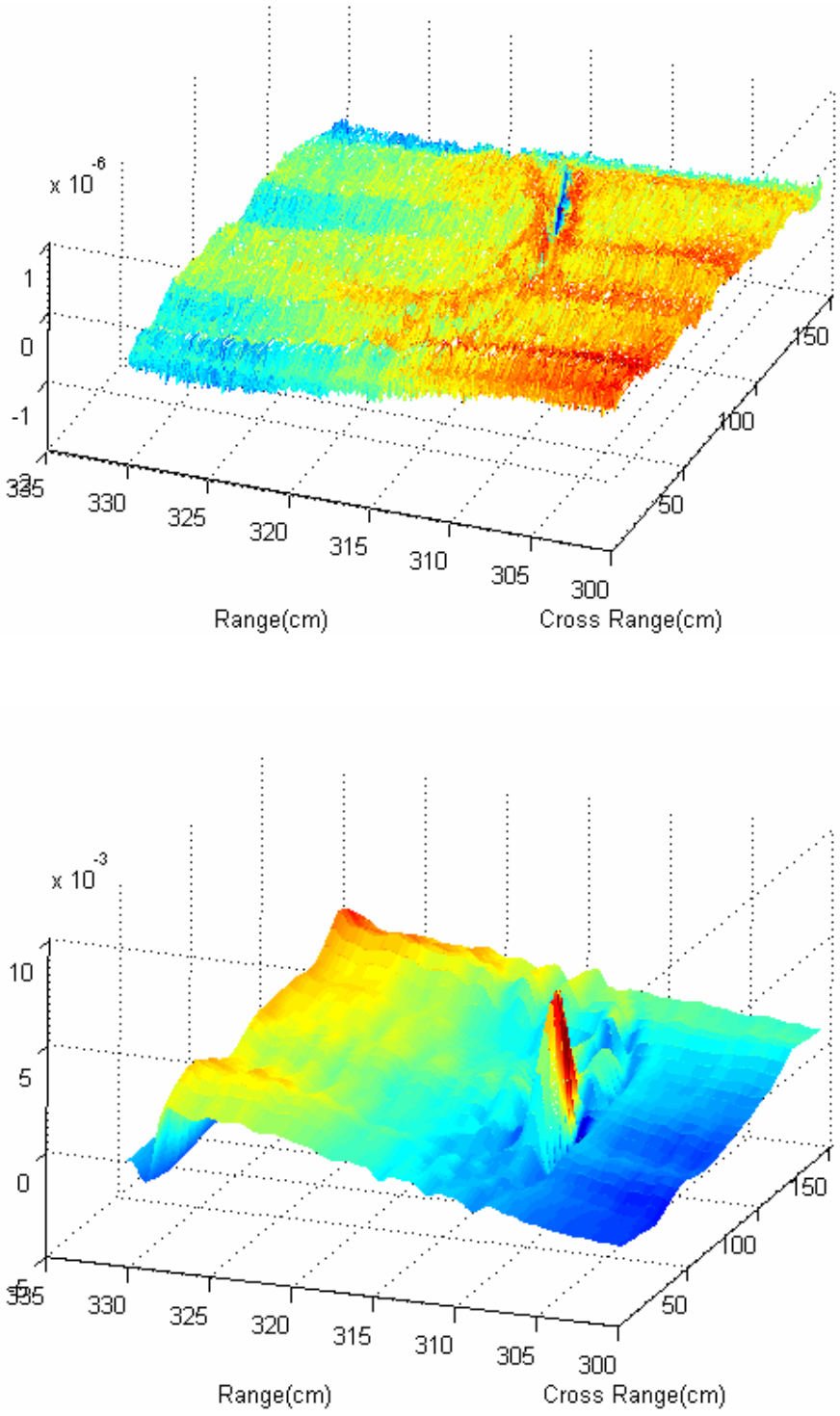

Figure 5-14: Mesh plots of raw (top) and the resultant (bottom) data

Since the goal of the algorithm is imaging through the wall, another experiment is done in front of a 5 cm thick drywall as shown in Figure 5-15 and Figure 5-16. A water container with a radius of 26 cm is covered using aluminum

Figure 5-15: Antennas in front of the wall

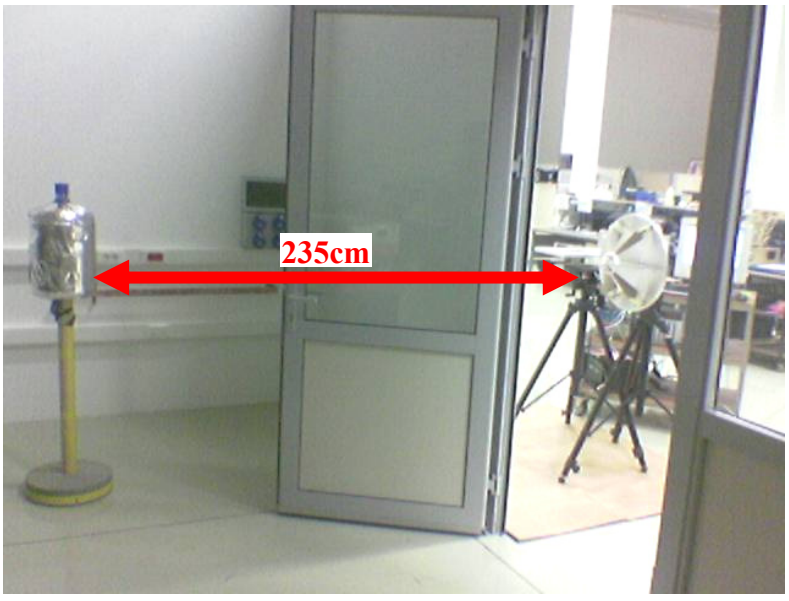

Figure 5-16: The target and antennas

foil and placed 160 cm away the wall,100 cm over the floor. The antennas are placed 80 cm away in the front side of the wall on the plate and the distance between the antennas is 41.5 cm. The plate is slided in steps of 5 cm for a total track length of 140 cm, as it touches the wall for keeping the distance to the wall constant. When the collected raw data and the output of the algorithm are imaged, the images in Figure 5-17 and Figure 5-18 are obtained.

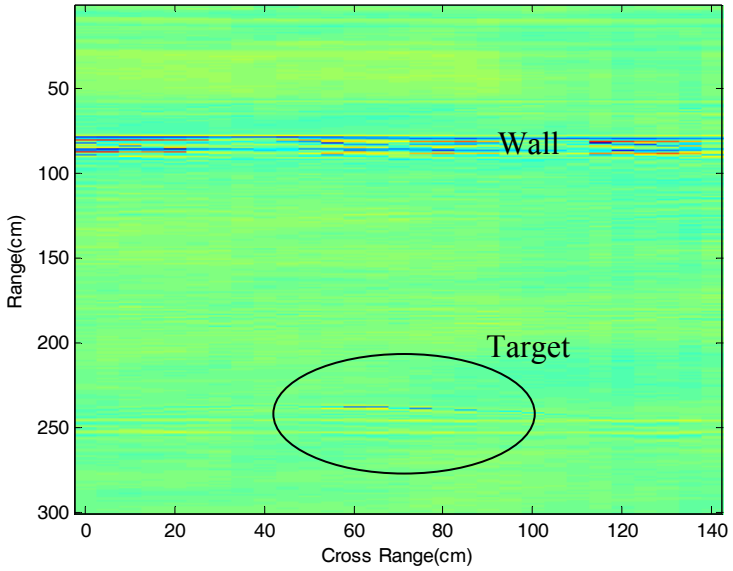

Figure 5-17: The raw image of the scene

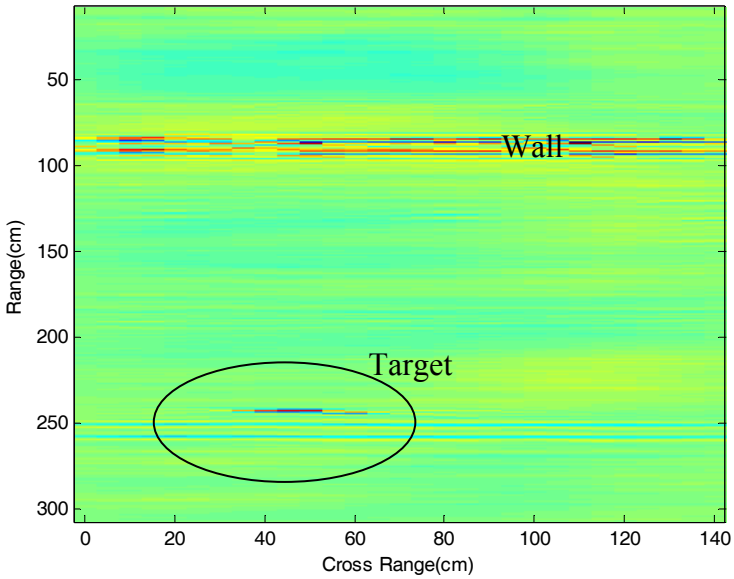

Figure 5-18: The output image of the algorithm

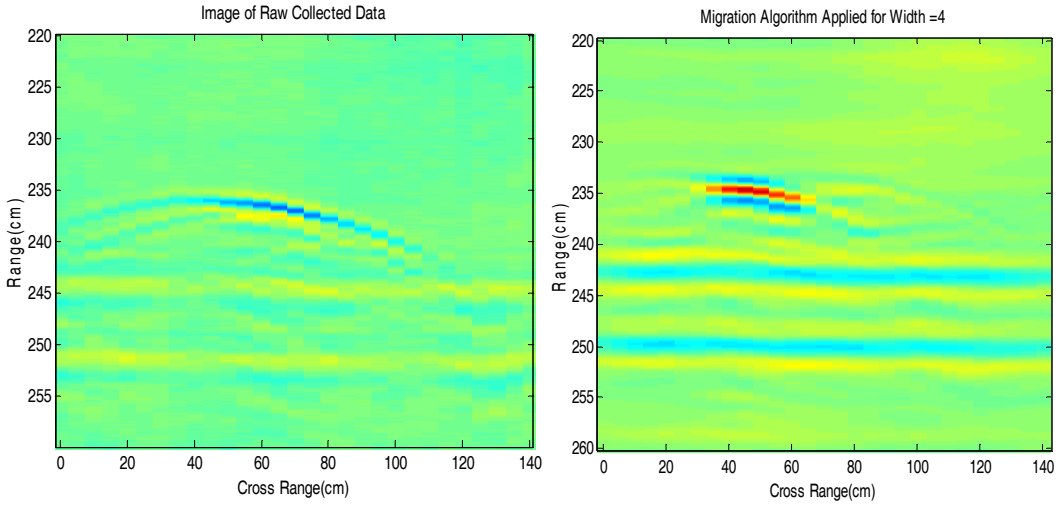

Figure 5-19: Comparison of the target in the two images (zoomed)

If the zoomed portions of the images around the target are observed, the effect of the algorithm can be understood better. The target in the raw image is shown as a migration curve and the intensity is more around 60cm cross-range although the center is around 45cm. Also the range of the target seems as if it is more than 237cm. In the processed image, the migration curve is beaten and the target is seen at the center of the curve at its true cross-range location. The range is also corrected as 235cm. The result of the algorithm can also be realized better by checking the mesh plots in Figure 5-20. The lines passing through the range of 243cm and 250cm are not a result of the algorithm, but caused by a problem in the setup. The problem and its solution will be discussed later.

This experiment proves the algorithm works well; and also the algorithm and the setup have a satisfactory imaging capability for drywall. Although this setup works well, the setup and consequently the algorithm can be improved for handling stronger walls and longer range. This is discussed in the following chapter.

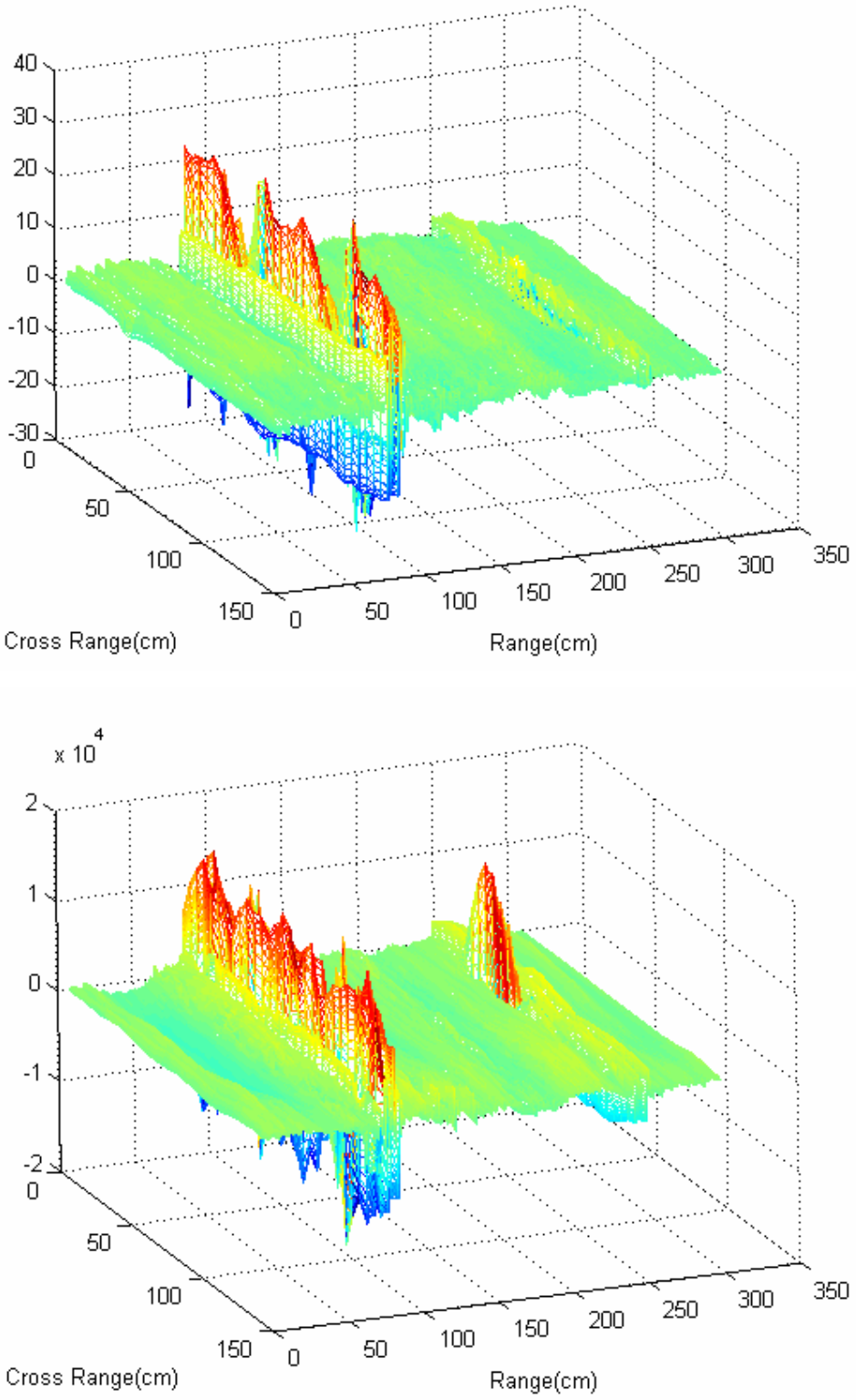

Figure 5-20: Mesh plots of the scene, raw (top) and the resultant (bottom) data

5.3.2 IMPROVEMENTS ON THE SYSTEM

The experimental system is formed of a pulse generator, a sampling scope and two antennas. These are general purpose devices and the experimental system is not a dedicated system for through the wall imaging. Consequently, it has some limitations on the performance. For increasing the system performance three items are worked:

- changing the tx and rx antenna placements for effectively receiving the reflections
- sliding the antennas automatically
- improving the pulse shape and switching off the undesired second pulse

5.3.2.1 CHANGING ANTENNA PLACEMENTS

In the former studies, the antennas were mounted on two tripods and placed side by side. As the experiments are performed, it is realized that by doing so the antennas are not efficiently used. The total gain of the antennas can be increased by placing the antennas not side by side but one antenna over the other.

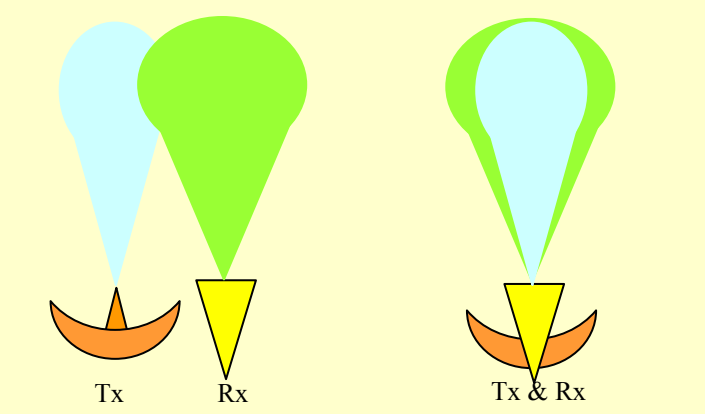

Figure 5-21: Antenna beams for two different installations of the antennas

In this way the main lobes of the antenna beams are overlapped (Figure 5-21) and the total gain of the antenna system is increased. This placement is ideal for SAR application.

The effect of the antenna placement on the total antenna gain can be observed in Figure 5-22. For the both cases, pulses reflected from a wall are collected and plotted. When the rx antenna is near tx antenna, the received peak-to-peak pulse voltage is 18.07 mV. When the rx antenna is over the tx antenna, the received peak-to-peak pulse voltage is 26.86 mV. This means the new antenna placement gives an extra antenna gain of 3.44 dB.

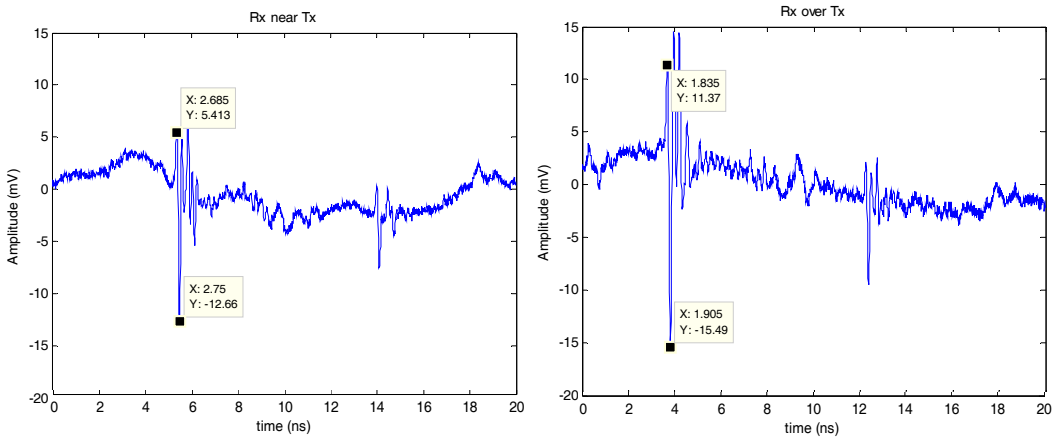

Figure 5-22: Antenna beams for two different placements of the antennas

The system operates in the x-y plane parallel to the surface, means it does not process the height. In the previous placement, the locations of the tx and rx antennas were different in the x-y plane and consequently the systems was not a perfect monostatic radar. The distance of the target to the rx antenna was not the same as the distance to the tx antenna and the location of the target was calculated by also considering the distance between the antennas. By placing the antennas on top of each other, the locations of the antennas are made the same in the x-y plane. This simplified the target range calculations and increased the accuracy of the target location.

As mentioned, by the new placement the total gain of the antenna system and the target locationing accuracy are increased. This makes the system capable of imaging longer range and handling thicker & stronger walls.

5.3.2.2 AUTOMATICALLY SLIDING THE ANTENNAS

In the former SAR setup, the antennas were mounted on tripods and they were placed on a plate of cardboard. The antenna system was moved by sliding the plate on the floor along a drawn line. Accurately sliding in this way was so difficult and also required a long time. For sliding, an automated solution was required.

Figure 5-23: The antenna slider used in the experimental setup

As a solution to this problem the slider in Figure 5-23, Thomson's belt driven slide guided positioning unit, is used. It has user interface software and can be controlled by an operator from a PC over RS-232; but for controlling it by Matlab the command set of the slider was necessary. (For obtaining the commands sent over RS-232, a serial monitor software is used during the

operation and the messages between the PC and the slider are logged. By studying these logs, the necessary commands to be send by Matlab are detected.)

The total track length can be maximum 4m, as the length of the slider, and the step size, distance between the stops on the track, can be adjusted to any value in mm resolution. In the experiments 4cm step size is used. Using the commands, a code is written for automatically sliding the antennas and collecting data sequentially from each stop on the track. The code works as follows:

- send the antennas to the first stop on the track and wait for the antennas to reach the stop
- initiate the scope and start acquisition of the data
- wait for the acquisition completed signal from the scope
- pull the data from the scope and send the antennas to the next stop on the track

By the help of the slider, the system gained the ability of automatically collecting data in an accurate way from the scene. This also decreased the time required for experiments.

5.3.2.3 IMPROVING THE TRANSMIT PULSE SHAPE

The former pulse shape used in the setup was formed by passing the output step pulse of the 4016 pulse generator from two 5208 pulse shapers sequentially as shown in Figure 2-15. This pulse was then amplified and transmitted. The former transmit pulse shape and its matched filter output at the receiver side are given in Figure 5-24.

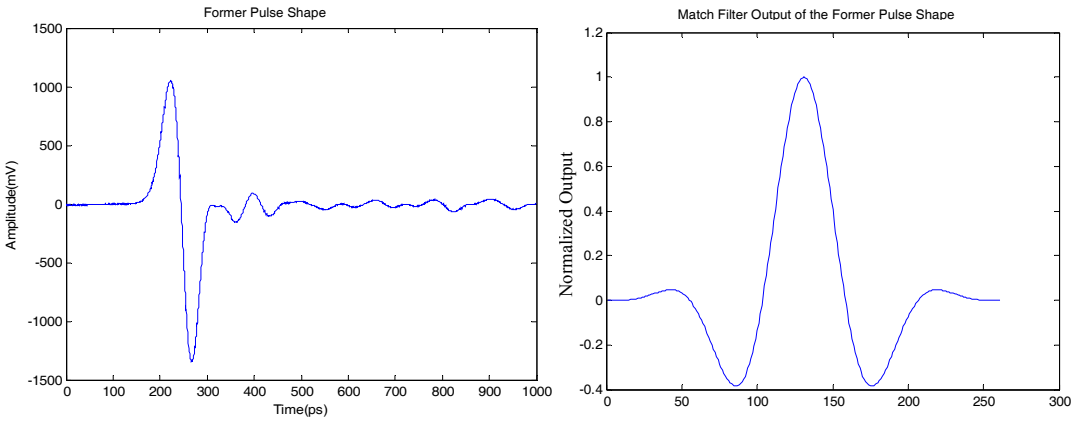

Figure 5-24: Former pulse shape and its matched filter output

As seen from the figure, the matched filter output of this pulse had one positive peak and two negative peaks at a level of -4dB. In theory the perfect matched filter output should be as close as possible to impulse function and practically the best matched filter output is the one which has a single narrow peak. For obtaining a better matched filter output, the pulse shapes that can be produced in the system are studied. It is realized that using a second pulse shaper for generating a Gaussian monocycle is not meaningful, since the generated pulse shape is integrated once more by the transmit antenna and the resultant shape is not a Gaussian monocycle anymore. By removing the second pulse shaper from the network, an impulse like pulse in Figure 5-25 is obtained. When this pulse is given to the transmit antenna, it is radiated as Gaussian monocycle. At the receiver side, matched filter output of the Gaussian monocycle pulse has a dominant positive peak and two negative peaks at a level of -7dB. This filter output is more like an impulse and better than the matched filter output of the former pulse shape. Consequently, the targets in the images will be observed more clearly.

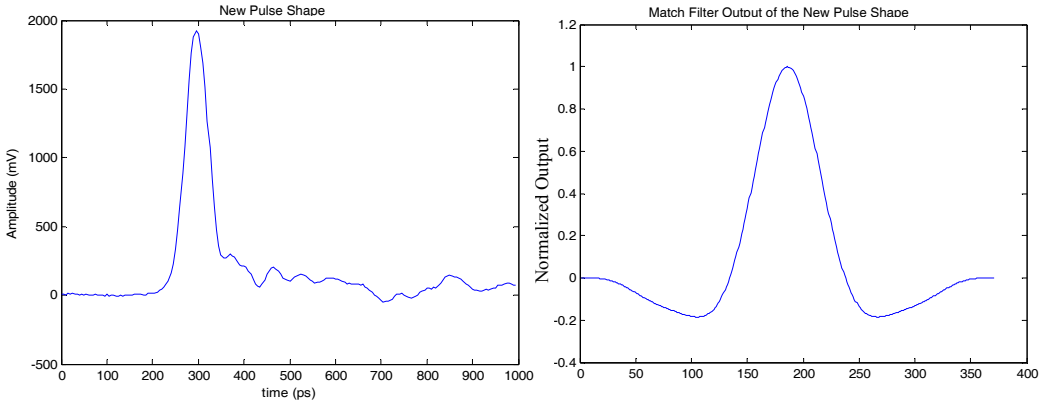

Figure 5-25: New pulse shape and corresponding matched filter output

Another improvement at least as important as the new pulse shape is switching off the second pulse generated by the pulse generator. The existence of this second pulse is realized while working on the images of the experimental scenes. Remember the straight lines in Figure 5-19.

For observing the problem, the image in Figure 5-26 can be studied. In the image, the wall is observed at 80cm range for all the cross-range and at 243cm range a similar shape is observed again along the full cross-range. The distance between the wall and this shape is 163cm. It seems as if there is a second wall at the back of the scene.

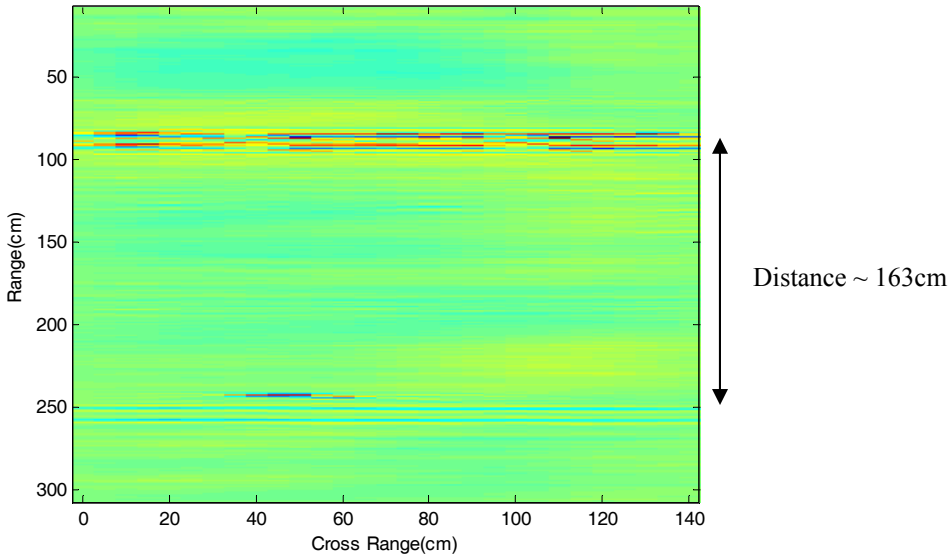

Figure 5-26: Ghost image of the wall 163 cm after the true location

The distance of 163cm in the image corresponds to t_{travel} duration

$$163cm = \frac{c.t_{travel}}{2} = \frac{3.10^{10}.t_{travel}}{2} \tag{5.15}$$

$$t_{travel} = \frac{163.2}{3.10^{10}} \cong 11ns \tag{5.16}$$

This means, two reflections are collected from the wall and between these two reflections there is a time difference of ~11ns. If the antenna transmits a second pulse 11ns later the transmission of the first pulse this can be observed, upon the examination of transmit pulse a second pulse which is undesired is spotted in the transmitted pulse as in Figure 5-27.

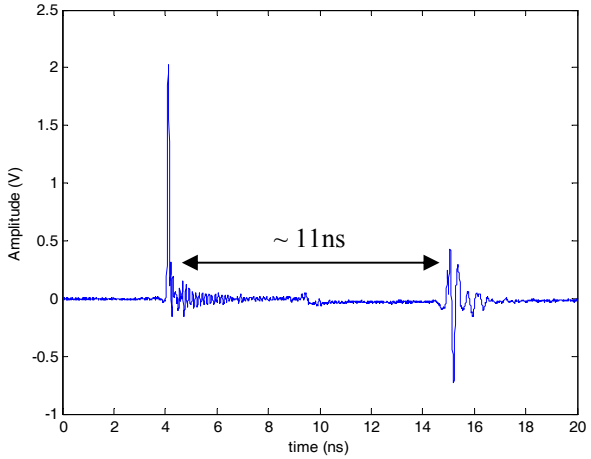

Figure 5-27: Signal fed to the transmit antenna

The input signal to the pulse shaper is the output of the 4016 pulse generator given in Figure 5-28. In this signal a small fluctuation can be observed ~11ns later the steep falling edge. This fluctuation seems to be the source of the second pulse. Then this means that when the signal given in Figure 5-28 is input to the 5208 pulse shaper, the output is like in Figure 5-27.

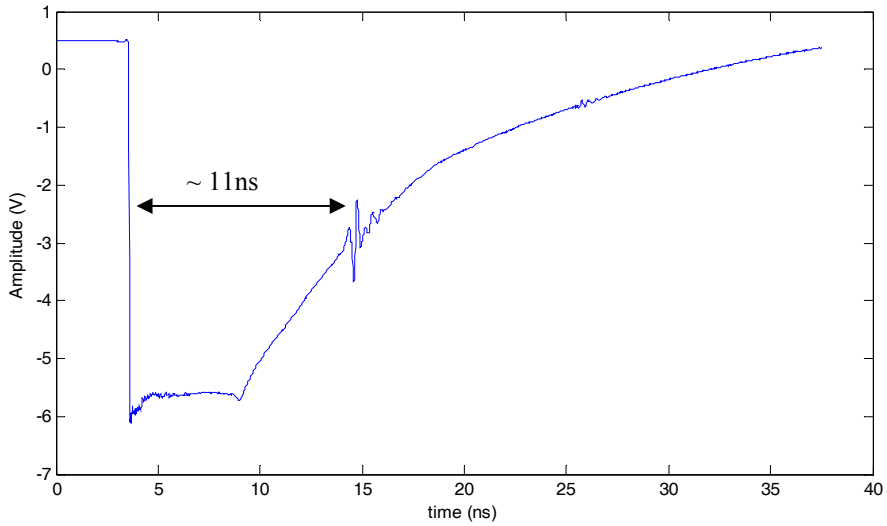

Figure 5-28: Signal at the output of the 4016 pulse generator

This pulse shaper differentiates the signal in time-domain. The output of it for an input V(in) is given as

$$V(out) \approx T_c * dV(in)/dt \tag{5.15}$$

where T_c is the derivative time coefficient and 8 ps for 5208 [30]. The derivative of the steep falling edge in Figure 5-28 must be like an impulse. The derivative of the flat signal portion from 4ns to 9ns is nearly zero and the slow rise from 9ns to the end is also ignored by the pulse shaper since the slope of this part is really small except the fluctuations around 15ns. The fluctuations seem like a Gaussian monocycle. Actually Figure 5-27 is consistent with these. The first pulse is like an impulse and the second one is like the derivative of a Gaussian monocycle.

This second pulse limits the operating range of the system. The first target in the image is repeated 165cm later and after this range the replicas of the near targets and the images of the far targets are overlapped. The real targets and the replicas can not be separated from each other.

The radiation of the second pulse from the transmit antenna could be prevented by switching off the path to the antenna after the desired pulse is transmitted. This could be managed by a very fast switch that can be completely switched off in a few ns and also has a broad band. The HMC547LP3 series

SPDT switch of Hittite Microwave is selected for this purpose. It switches one of its two input channels RF1 and RF2 to its output. It has a switching time of 6ns from one channel to the other and has a broad band from DC to 20 GHz [32].

The output of the pulse generator is connected to RF1 input of the switch and RF2 input is terminated by 50Ω load, which is used as the off state of the switch. The switch needs two complementary negative control lines of -5/0 V named as A and B. These control signals are generated from the trigger pulse output of the 4016 pulse generator. It outputs a 80ns long, 2.3V (to 50Ω) trigger pulse from the trigger output port, 60ns before generating the pulse at the pulse output port. The positive trigger level is shifted to negative by four BAV99 dual diodes in serial (a total of eight diodes) and delayed by passing through fifteen inverter gates from three 74HCT04 Hex Inverter (Figure 5-29).

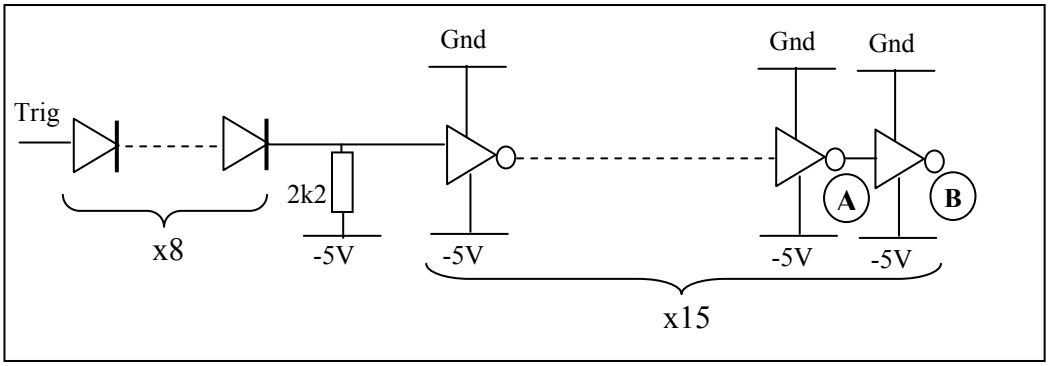

Figure 5-29: Designed level shift and delay circuitry

Each gate has a delay of nearly 4ns and the total delay of the path is slightly more than 60ns. Output of the 14th inverter is connected to A and the 15th inverter is connected to B control input of the switch. In this way, the path to the transmit antenna is switched off at 66ns later the rising edge of the trigger pulse and it is hold in off state for 80ns. Actually the switch is connected between the pulse generator and the shaper. After the falling edge of the step pulse, it switches to the 50Ω terminated channel and the fluctuation in the generator output is not transferred to the shaper. Consequently, the first pulse is generated and

transferred to the antennas while the second pulse is never generated. The timing diagram is given in Figure 5-31.

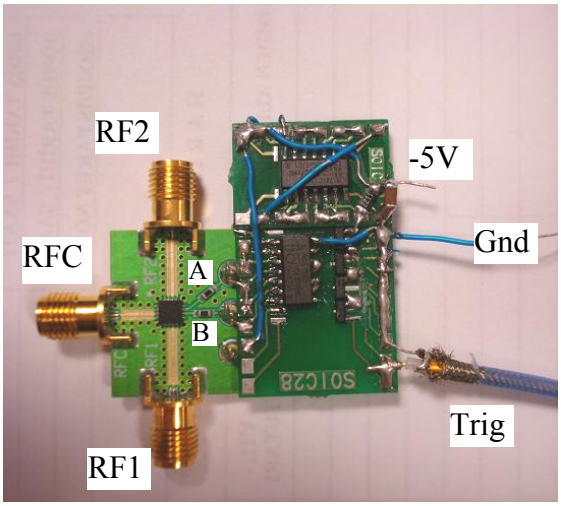

Figure 5-30: Designed circuitry mounted on the switch (front side)

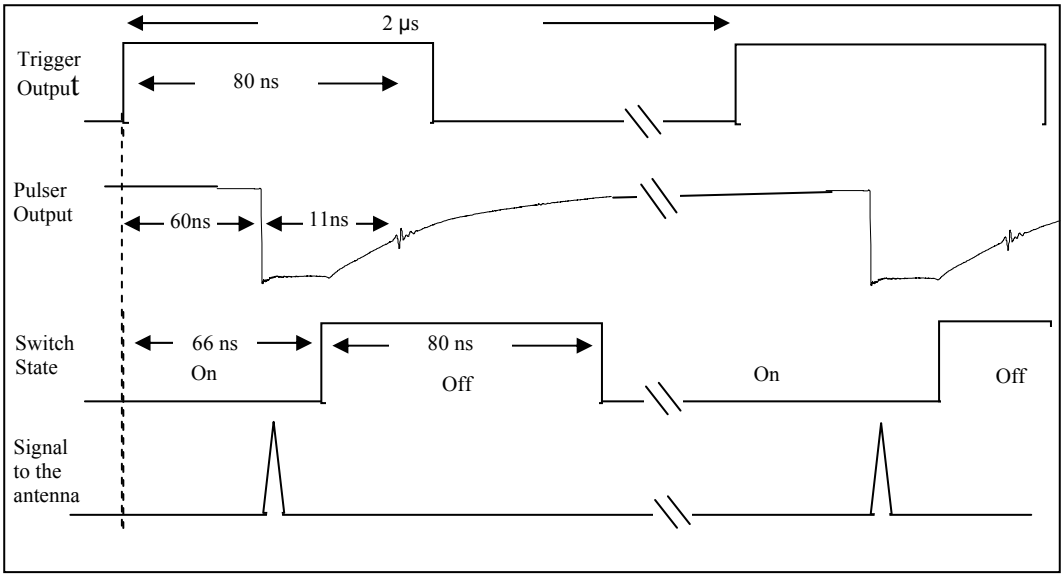

Figure 5-31: Timing diagram for switching

The switch has an insertion loss around 2 dB and attenuates the pulse, but this loss can be accepted regarding the clean pulse it offers (Figure 5-32). By the

help of this switch and the circuitry, range of the system is increased. The block diagram of the improved setup is given in Figure 5-33.

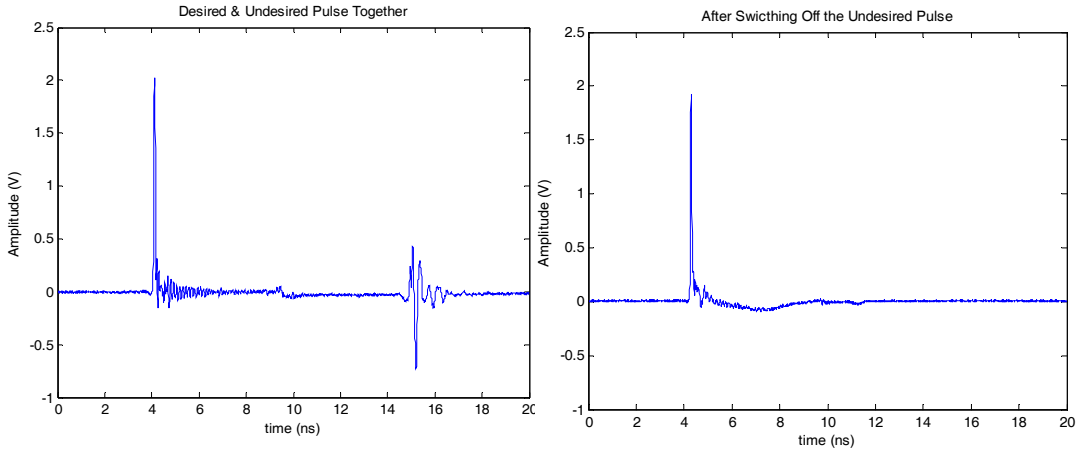

Figure 5-32: Pulse shape without/with switching

The peak voltage of the new pulse shape is ~2 V and its duration is 150 picoseconds. Since the system is an 50 Ω system, the peak transmit power can be calculated as

$$P_{peak} = \frac{V^2}{R} = \frac{4}{50} = 80 \ mW \tag{5.16}$$

The PRI of the system is 2 μsec, so the average transmit power is

$$P_{avg} = P_{peak} x \frac{\tau}{PRI} == 80x \frac{150x10^{-12}}{2x10^{-6}} = 6 \ \mu W \tag{5.17}$$

These power levels are very low compared to the power levels of the commercial systems discussed in chapter 2.6.

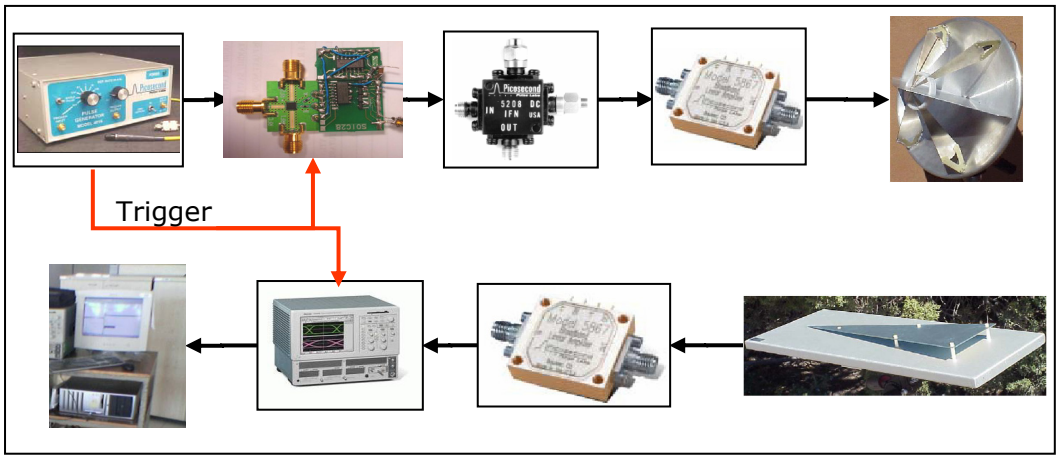

Figure 5-33: Block diagram of the improved setup

5.3.3 EXPERIMENTS WITH THE IMPROVED SYSTEM

After the mentioned improvements, new imaging experiments are done for observing their effects. In the experiments the automated antenna slider system is located 60cm ahead from a 20cm ytong wall. This is really stronger than the drywall since it has a measured loss of ~13.4 dB while the loss of drywall is given as ~0.5 dB in [25]. As the target a cardboard box is used. Its floor

Figure 5-34: The covered cardboard box

and the two flaps are cover with aluminum folio as in Figure 5-34. It is chosen as a target because the migration curves of the two flaps will interfere to each other. If the suggested anti-migration algorithm works well, it must be capable of handling these interferences and could clearly image the two flaps and the floor of the box. The box is located as the flaps are 93 cm and the floor of the box is 130 cm away the wall as in Figure 5-35. The automated setup is activated and the scene is imaged using the updated version of the anti-migration algorithm for the improved setup.

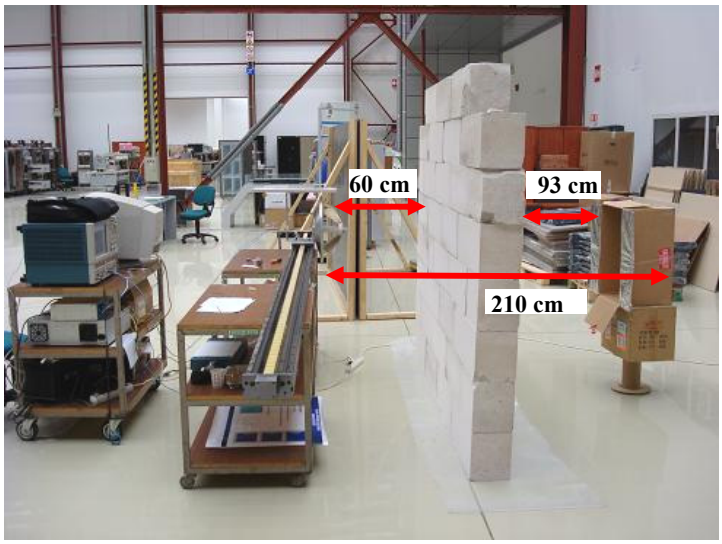

Figure 5-35: The experimental scene

The matched filtered image of the scene is given in Figure 5-36. It is the image before applying the anti-migration algorithm and the migration curves can be clearly observed on the zoomed portion of this image in Figure 5-37. The curves of the two flaps are interfered as expected. It can also be realized that, different from the previous images, the migration curves are symmetric around their centers. This means, locating the antennas on top of each other made the antenna system symmetric in the x-y axis and improved the data collection.

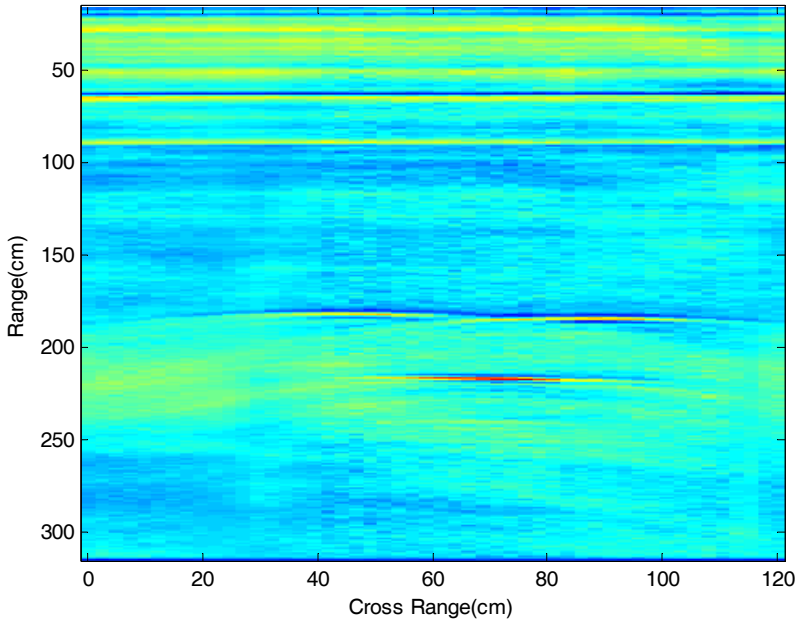

Figure 5-36: Matched filtered image of the experimental scene

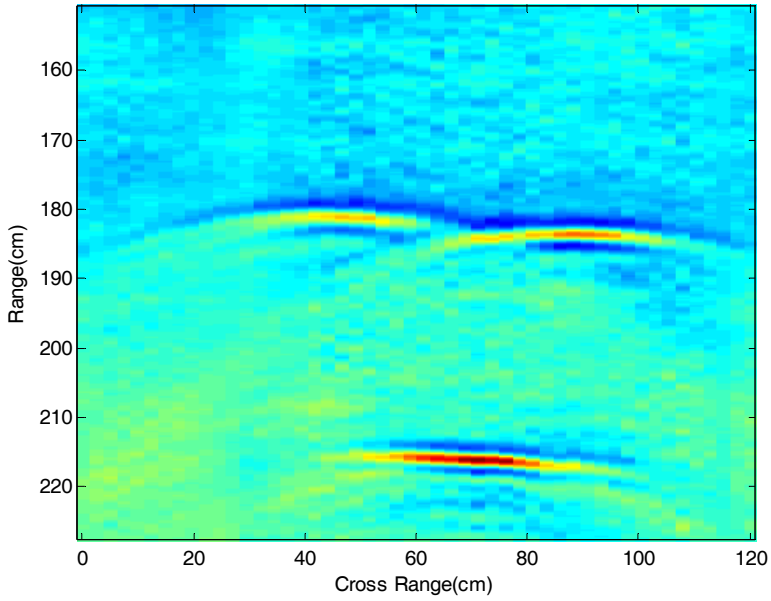

Figure 5-37: Matched filtered image zoomed around the target

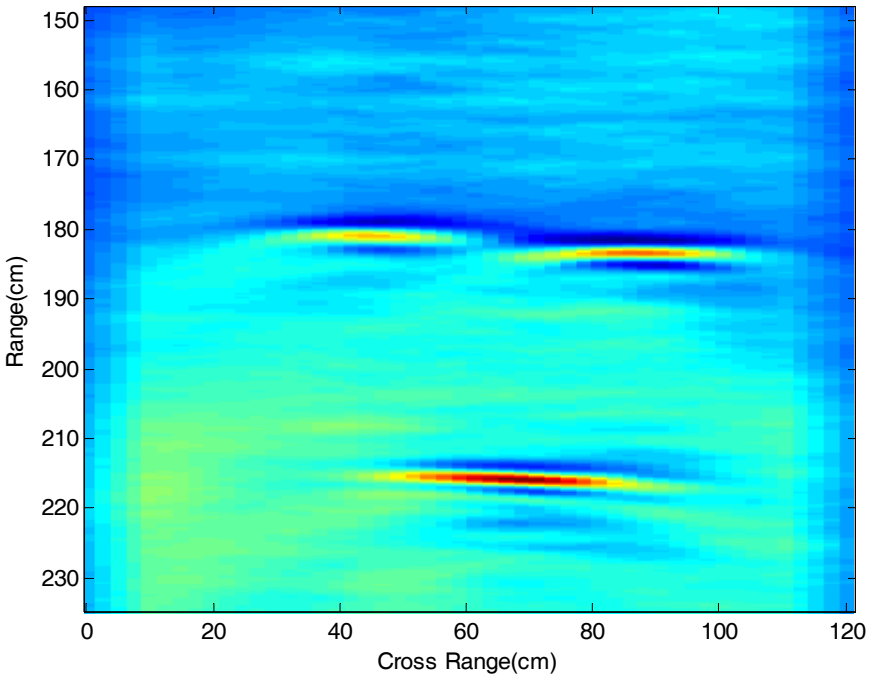

Figure 5-38: Anti-migration applied image zoomed around the target

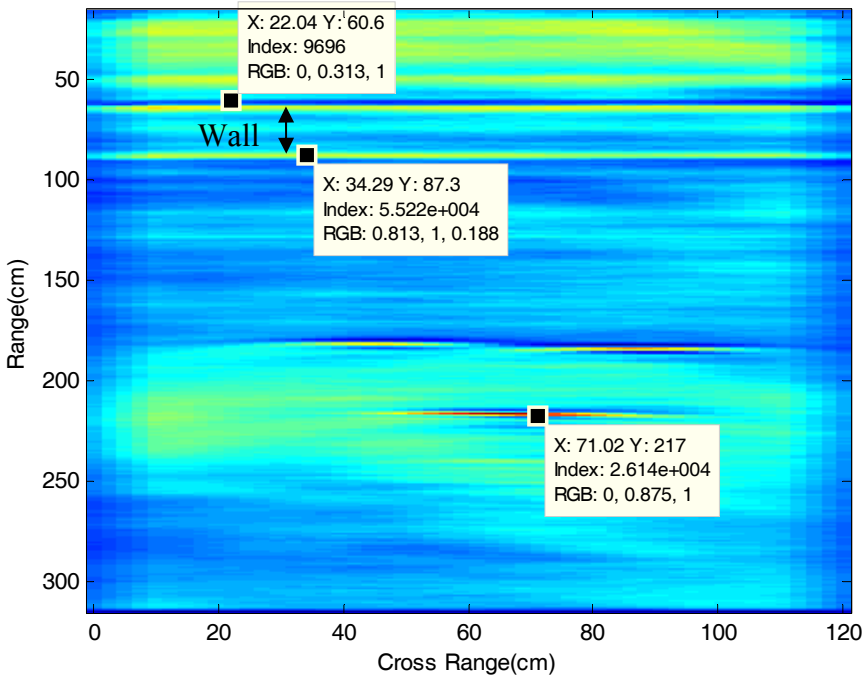

Figure 5-39: Anti-migration applied image

As seen in Figure 5-38, the migration curves are beaten by the algorithm. The floor of the box is actually at 210 cm from the antennas, but in the figure it seems at a further range. This is because of the decrease in the speed of the pulse while passing through the wall. The wall is 20 cm thick, but in Figure 5-39 it seems as if it is ~27 cm thick and consequently the floor of the box seems shifted ~7 cm in range to 217 cm from its true location. Actually, the distance between the inner face of the wall and the box is measured correct as 93 cm; means the scene behind the wall is accurately imaged and the target locations are correct relative to the inner face of the wall. Only the wall seems thicker in the image and this can not be compensated without knowing the dielectric constant of the wall a-priori.

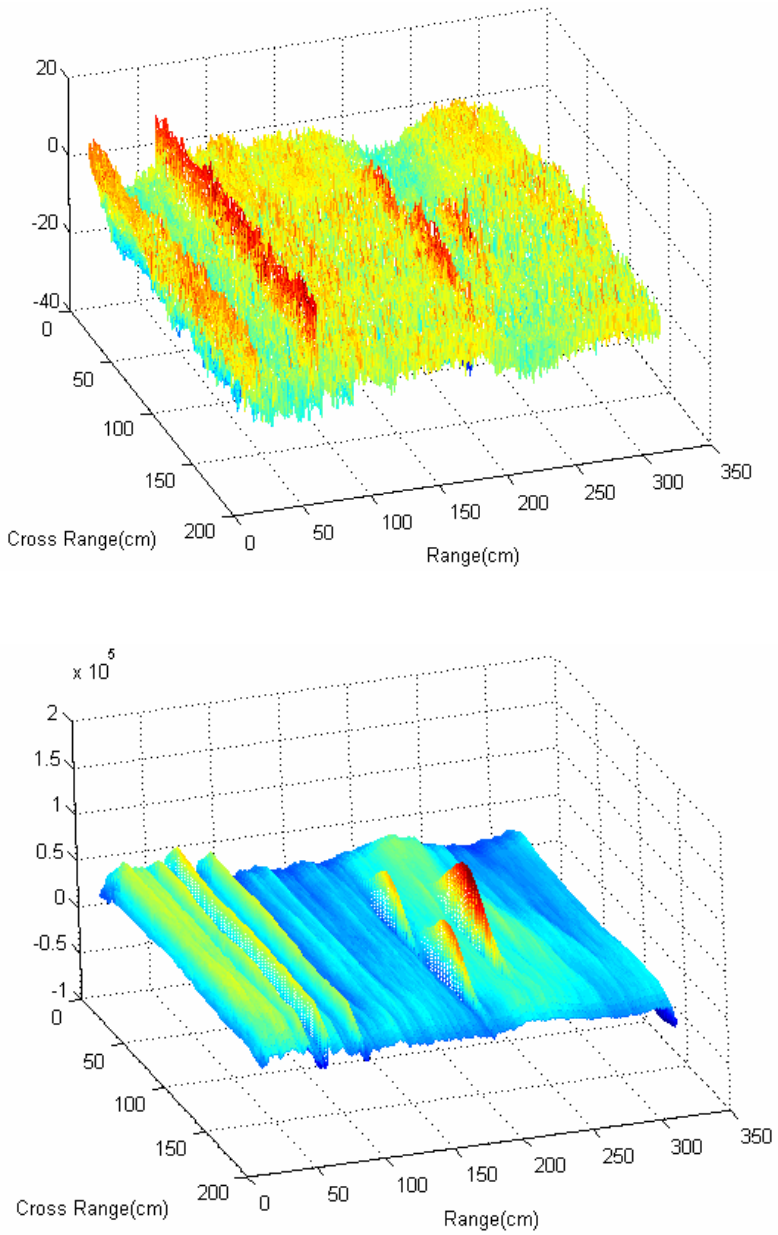

Figure 5-40: Mesh plots of raw (top) and processed data (below)

Another experiment is done in the same scene. This time the box is shifted further to 269 cm in range and the maximum range of record for the system is increased to 760 cm. Around the range of 600 cm there is a second wall. This scene is shown in Figure 5-41 and mesh plot of the scene after processing is given in Figure 5-42. In Figure 5-42 the target is again observable, and this time also the wall behind the target is in the range of the image. Since the target is metallically

coated the pulse can not penetrate through it and totally reflected back. Consequently, the parts of the wall shadowed by the target are not illuminated by the pulses and could not be imaged. The wall is observed on the both sides of the target, but not behind of it.

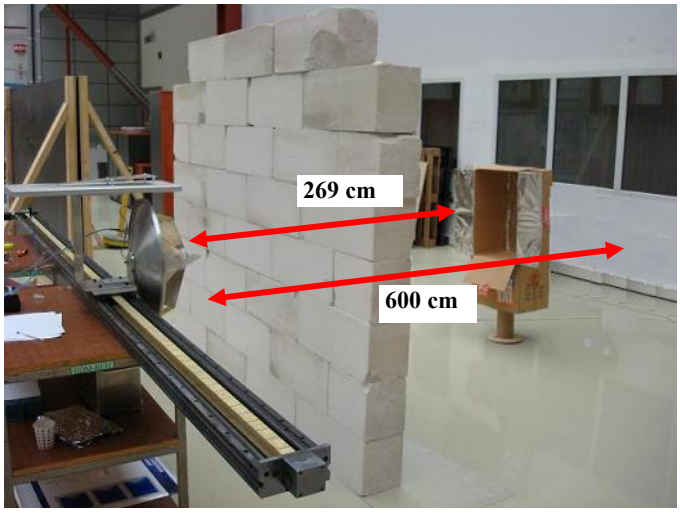

Figure 5-41: Long range experiment

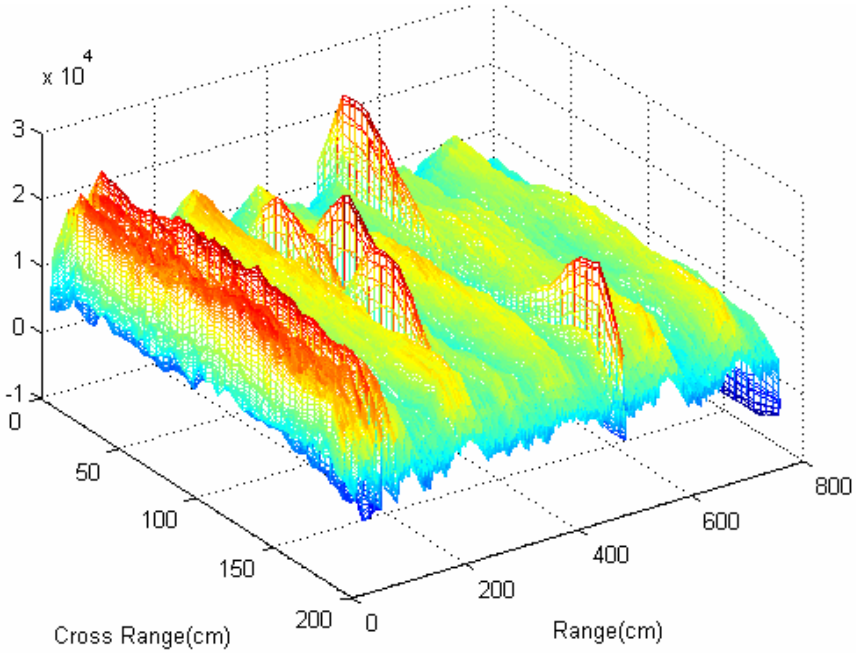

Figure 5-42: Mesh plot of the long range experiment scene

In the image a total range of ~8 m is shown and different from the early images there are not repeating walls or targets formed by the second pulse radiated after the main pulse. The second pulse has been successfully killed. Also reflections from 7.5m can be detected behind a ytong wall, this is managed by the increased total gain of the antennas and the increased processing gain of the system by the help of the new pulse shape and its better matched filter characteristic.

CHAPTER 6

CONCLUSION

In this thesis, the feasibility of UWB through the wall surveillance system is inspected. The hardware blocks of a UWB radar system, pulse generation & transmitter, receiver and antennas are studied in individual parts. An experimental system is set up using laboratory equipments and antennas. Working on the data collected by this system, algorithms are developed for through the wall imaging and respiration rate estimation.

The conventional communication and radar systems are narrowband systems. Consequently, the narrowband hardware is well-known and well-analyzed. On the contrary, UWB is a new topic and not fully matured. In the transmitter of a UWB through the wall surveillance system, short pulses that are hundreds of picoseconds can be generated using SRD diodes with PRF values in the order of MHz. As the receiver topology, correlation based operation is used in typical systems since they can perform well with low SNR signals and their spatial resolution is shorter than the actual signal duration. There are both digital and analog correlators, but for a portable system analog correlators are more reasonable considering the simplicity of hardware and the power consumption.

For a wideband digital correlator, ADC's with sampling rates of a few giga samples per second are necessary and for the processing of this large amount of digital data a very complicated and power consuming digital hardware is required. The UWB antennas can be the most challenging parts of UWB systems, since the required fractional bandwidth is very large covering multiple octaves. Also the antennas differentiate the pulse, so the antenna response must be taken into account for the realization of desired transmit pulse shape. The antenna candidates for an UWB system are axial mode helices, biconical dipoles, parabolic reflectors and frequency independent antennas such as spirals, conical spirals, log-periodic dipole arrays. Instead of using single antenna, an antenna array can be used for increasing the cross-range resolution. Loaded dipole (receive only), TEM horn, LPDA (log-periodic dipole array) and spiral (receive only) antennas are the common options for the array elements.

An experimental hardware system is set up in the laboratory in order to obtain the necessary data for algorithm development. Pulse generator, shapers and amplifiers used in the system are products of Picosecond Pulse Labs. Model 4016 pulse generator is used as for pulse generating. The undesired part with fluctuations in its step pulse output is switched off by using HMC547LP3 series SPDT switch of Hittite Microwave and output of the switch is shaped by model 5208 pulse shaper. Two 5867 amplifiers are used, one in front of the transmit antenna and one after the receive antenna as an LNA. The transmit antenna is IRA-3M and the receive antenna is TEM-1-50 from the Farr Research. The receiver of the system is a Tektronix TDS8200 sampling scope. This equivalent-time sampler limits the performance of the system in dynamic scenes because of its slow data acquisition technique. The collected data in the scope is pulled to a PC over GPIB and processed by Matlab. The resultant proof of concept UWB radar system has 80 mW peak, 6 μW average transmit power, 500 kHz PRF and range resolution far better than 1 cm.

In the literature breathing detection is commonly handled by Doppler radars, but there are also some examples of using UWB systems for this purpose. Also by the thesis work, it is experimentally proven that the respiration of a man

can be detected behind a wall, and if the man does not move much, the respiration rate can also be easily estimated by UWB systems. While breathing, the front face of the chest cavity moves 1-2 cm and this movement can be detected if the resolution of the system is better than this value. Using the suggested successive-channel estimation algorithm the respiration activity of a breathing man can be detected. Besides, if the sampling rate of the system is faster than the double of the frequency of repetitive chest movement activity, then it is possible to detect any respiration rate by processing the collected data using the suggested breathing frequency estimation algorithm. The algorithms are worked on the data collected by the experimental system. The system's range resolution is well enough for this application, but the sampling rate of the equivalent-time sampling scope limits the maximum detectable range of respiration frequency to 0.5 Hz.

UWB through the wall surveillance is commonly studied by the antenna arrays and the back projection algorithm, but this data collection method and the algorithm is not the best choice for this application against strong walls. A synthetic aperture array for data collection and an anti-migration algorithm for processing this data are suggested. Using synthetic aperture array is the most reasonable data collection method considering better total antenna gain and stronger back reflections due to the normal incidence to the wall during transmission and reception of the pulses. This method causes migration curves, but these are successfully handled using the suggested anti-migration algorithm. The data collection method and the algorithm work well enough that by only 6 μW average transmit power of the experimental systems, it is possible to image a static scene with a range of 8 meters behind a 20 cm thick ytong wall which has a single way loss of 13.4 dB. The locations and the cross-range dimensions of the targets are accurately imaged.

As a future work, a dedicated UWB radar hardware which is portable can be designed for the through the wall surveillance application. A real-time hardware will have the capability of collecting and processing the data faster and allow working on dynamic scenes. The synthetic aperture can also be formed by a hand-held UWB radar system, if it is propped to the wall and slided on it. A

suitable UWB antenna array can be preferred for better increasing the cross-range resolution of synthetic aperture. For this hand-held system a simple circuitry designed by using SRD diodes can be used as the pulse generator. The receiver topology must be selected as the analog correlator. Analog correlator may not have the same range resolution as a digital correlator, but it is simple and consumes considerably small power for sampling & processing compared with the digital correlator does. In this topology, the time of arrival is detected by the help of the analog hardware and this time information is then processed by the digital hardware for obtaining the locations of the targets and forming the image. The device can work in two modes, one is for imaging using anti-migration algorithm and the second is for breathing detection and estimation of its frequency.

REFERENCES

[1] Federal Communications Commission, "Revision of Part 15 of the Commissions Rules Regarding UWB Transmission Systems," First Report, FCC 02-48, April 2002.

[2] Igor Immoreev, "Ten Questions on UWB," IEEE AES Systems Magazine, November 2003.

[3] Mobile and Portable Radio Research Group, Virginia Tech, "Implementation and Analysis of Respiration-Rate Estimation Using Impulse-Based UWB," Military Communications Conference, 2005.

[4] E. F. Greneker, "Radar Sensing of Heartbeat and Respiration at a Distance with Applications of the Technology," Radar 97, 14 - 16 October 1997.

[5] A.G. Yarovoy, L.P. Ligthart, J.Matuzas, B. Levis, "UWB Radar for Human Being Detection," IEEE A&E Systems Magazine, March 2006.

[6] Yifan Chen, Erry Gunawan, Kay Soon Low, Yongmin Kim, Cheong Boon Soh, A. Rahim Leyman, and Lin, "Non-Invasive Respiration Rate Estimation Using Ultra-Wideband Distributed Cognitive Radar System ," Proceedings of the 28th IEEE EMBS Annual International Conference, New York City, USA, Aug 30-Sept 3, 2006.

[7] Swaroop Venkatesh, Christopher R. Anderson, Natalia V. Rivera and R. Michael Buehrer, "Implementation and Analysis of Respiration-Rate Estimation Using Impulse- Based UWB," Military Communications Conference, 2005.

[8] Gerald Ossberger, Thomas Buchegger, "Non-Invasive Respiratory Movement Detection and Monitoring of Hidden Humans using Ultra Wideband Pulse Radar," Ultra Wideband Systems, 2004.

[9] Walid A. Chamma and Satish Kashyap, "Detection of Targets Behind Walls Using Ultra Wideband Short Pulse: Numerical Simulation," Technical Memorandum, DRDC Ottawa, TM 2003-226, November 2003.

[10] Sylvain Gauthier, Eric Hung and Walid Chamma, "Surveillance Through Concrete Walls," Technical Memorandum, DRDC Ottawa, TM 2003-233, December 2003.

[11] Genyuan Wang, Moeness g. Amin, Yimin Zhang, "New Approach for Target Locations in the Presence of Wall Ambiguities," IEE Transactions on Aerospace and Electronic Systems, vol. 42, no. 1, January 2006.

[12] Senglee Foo, Alan Walsh and Satish Kashyap, "Ultra-wideband (UWB) Remote Sensing and Radar Imaging," Technical Report, DRDC Ottawa, TR 2004-081, May 2004.

[13] Joelle Boutros and Greg Barrie, "Ultra-wideband Synthetic Aperture Radar Imaging," Technical Memorandum, DRDC Ottawa, TM 2003-177,November 2003.

[14] James D. Taylor, "Introduction to Ultra-Wideband Radar Systems," CRC Press, 1995.

[15] Greg Barrie, Jake Tunaley, "An Analysis of Through- and In-the-Wall UWB Impulse Radar," Technical Memorandum, DRDC Ottawa, TM 2003-134, September 2003.

[16] Hewlett-Packard, "Pulse and Waveform Generation with Step Recovery Diodes (AN 918)," October 1984.

[17] Wikipedia, July 15, 2007 retrieved from http://en.wikipedia.org/wiki/ Step_recovery_diode.

[18] K. Yekeh Yazdandoost, R. Kohno, UWB Technology Institute, "Design and Analysis of an Antenna for Ultra-Wideband System".

[19] Ramesh Harjani, Jackson Harvey, Robert Sainati, "Analog/RF Physical Layer Issues for UWB Systems," Proceedings of the 17th International Conference on VLSI Design, 2004.

[20] Dr. Motohisa Kanda, "Time-Domain Sensors & Radiators," ch 5 in EK Miller, editor, Time-Domain Measurements in Electromagnetics, Van Nostrand Reinhold, New York, 1986.

[21] James R. Andrews, Picosecond Pulse Labs, "UWB Signal Sources, Antennas & Propagation, AN-14a," August 2003.

[22] Tektronix, July 10, 2007 retrieved from http://www.tek.com/Measurement/ App_Notes/ RTvET/ap-RTvET.html - 25k.

[23] Merrill I. Skolnik, "Introduction to Radar Systems, 3rd edition," McGraw-Hill, 2001.

[24] Stephen P. Lohmeier, Raviprakash Rajarman, Vijaya C. Ramasami, "An Ultra-Wideband Radar for Vehicle Detection in Railroad Crossings," Sensors Conference, 2002.

[25] Ahmad Safaai-Jazi, Sedki M. Riad, Ali Muqaibel, Ahmet Bayram, "Ultra-wideband Propagation Measurements and Channel Modeling," DARPA NETEX Program, 2002.

[26] Alan V.Oppenheim, Alan S.Willsky, S.Hamid Nawab, "Signals & Systems," 2nd edition, Prentice-Hall.

[27] David K.Cheng, "Fundamentals of Engineering Electromagnetics," International Student Edition, 2nd. Ed., Addison Wesley, 1993.

[28] N. Sudarshan Rao, "Demonstrating the Reflection of an Electromagnetic Pulse from a Dielectric Slab Using FDTD Method," Electromagnetic Interference and Compatibility'97, 1997.

[29] Picosecond Pulse Labs, "Model 5867, 15 GHz Linear Amplifier, spec-4040087, revision1," October, 2002.

[30] Picosecond Pulse Labs, "Product Specification Models 5208, 5210, 5212a, 5214, 5216 Impulse Forming Networks, spec-4040026, revision 4," December 2004.

[31] Farr Research Inc., "Catalog of UWB Antennas and HV Components," January 2007.

[32] Hittite Microwave Corp., "Hmc547lp3 / 547lp3e Gaas Mmic Spdt Non-Reflective Switch, Dc - 20.0 GHz," v00.0305.

[33] Senglee Foo, Alan Walsh, Satish Kashyap, " Ultra-wideband (UWB) Remote Sensing and Radar Imaging," Technical Report, DRDC Ottawa, TR 2004-081, May 2004.